GROWTH AND CHARACTERIZATION OF THIN SiO_2 AND Ta_2O_5
DIELECTRIC LAYERS BY Nd:YAG LASER OXIDATION

A THESIS SUBMITTED TO

THE GRADUATE SCHOOL OF NATURAL AND APPLIED SCIENCES

OF

MIDDLE EAST TECHNICAL UNIVERSITY

BY

GÜLNUR AYGÜN ÖZYÜZER

IN PARTIAL FULFILLMENT OF THE REQUIREMENTS FOR THE DEGREE OF

DOCTOR OF PHILOSOPHY

IN

PHYSICS

APRIL 2005

Approval of the Graduate School of Natural and Applied Sciences

_____

Prof. Dr. Canan Özgen

Director

I certify that this thesis satisfies all the requirements as a thesis for the degree of Doctor of Philosophy.

_____

Prof. Dr. Sinan Bilikmen

Head of Department

This is to certify that we have read this thesis and that in our opinion it is fully adequate, in scope and quality, as a thesis for the degree of Doctor of Philosophy.

_____   _____
Prof. Dr. Sinan Bilikmen   Prof. Dr. Raşit Turan
      Co-Supervisor   Supervisor

Examining Committee Members

Prof. Dr. Hüsnü Özkan   (METU, PHYS)   _____

Prof. Dr. Raşit TURAN   (METU, PHYS)   _____

Prof. Dr. Sinan BİLİKMEN   (METU, PHYS)   _____

Prof. Dr. Bahtiyar SALAMOV (GAZİ UNV, PHYS) _____

Assoc. Prof. Dr. Gülay ÖKE   (METU, PHYS)   _____

I hereby declare that all information in this document has been obtained and presented in accordance with academic rules and ethical conduct. I also declare that, as required by these rules and conduct, I have fully cited and referenced all material and results that are not original to this work.

Name, Last name   : Gülnur, Aygün Özyüzer

Signature   :

ABSTRACT

GROWTH AND CHARACTERIZATION OF THIN SiO_2 AND Ta_2O_5
DIELECTRIC LAYERS BY Nd:YAG LASER OXIDATION

Aygün Özyüzer, Gülnur

Ph. D., Department of Physics

Supervisor: Prof. Dr. Raşit Turan

Co-Supervisor: Prof. Dr. Sinan Bilikmen

April 2005, 136 pages

Our aim was to establish a methodology for laser assisted oxidation of
semiconductor and metal surfaces. One advantage of laser oxidation is the fact that
radiation is heavily absorbed in a thin surface layer of the sample and the other is its
ability for local oxidation. In addition to this, laser beam can be directed into some
areas that other processes cannot reach. For these reasons, Nd:YAG pulsed laser
working at 1064 nm wavelength is used for the oxidation purposes of Si and Ta
films.

First, SiO_2 layer was obtained for various O_2 pressures and laser powers. The
thickness, refractive index, structural, dielectric, electrical and optical characteristics
of the SiO_2 layers have been determined. We have established that there exists an
interval of laser power in which the oxidation occurs without surface melting. The
oxidation process is controlled by the laser power rather than by the substrate

temperature (673 – 748 K). It was found that better film quality is obtained at higher substrate temperatures and laser power greater than 3.36 J/cm^2.

Second, rf-sputtered Ta films were oxidized by laser, because Ta_2O_5 appears to be a good promising candidate to replace SiO_2 because of its high dielectric constant, high breakdown voltage and relevant small leakage current values. It was found that the substrate temperature is an important parameter to obtain denser layers with reduced amount of suboxides and the most suitable substrate temperature range is around 350^0C to 400^0C. β-orthorhombic crystal structure was obtained when the substrate temperature is $350 – 400^0$C for thinner films (up to 20 – 25 nm) and $300 – 350^0$C for thicker films (40 nm). The refractive index values of laser grown thin tantalum oxide films were between ~1.9 and 2.2 being close to those of bulk Ta_2O_5 (2.0 – 2.2). Oxide thicknesses in uniform Gaussian–like shapes were measured as around the twice of those initial Ta films. Effective dielectric constant values reached ~26 when the substrate temperature was increased from 250^0C to around 400^0C. It was shown that the leakage current density level decreases with increasing substrate temperature. However, the refractive index values of the films were smaller than those of thermally grown films. Porous structure formed during laser oxidation might be the reason for lower refractive indices and can be improved by post–oxidation annealing.

Keywords: SiO_2, Ta_2O_5, Nd:YAG laser oxidation, XPS, MOS structures, reflectance and refractive index.

ÖZ

Nd:YAG LASER OKSİTLEME YÖNTEMİ KULLANILARAK
İNCE SiO$_2$ VE Ta$_2$O$_5$ DİELEKTRİK TABAKALARIN
BÜYÜTÜLMESİ VE KARAKTERİZE EDİLMESİ

Aygün Özyüzer, Gülnur

Doktora, Fizik Bölümü

Tez Yöneticisi: Prof. Dr. Raşit Turan

Ortak Tez Yöneticisi : Prof.Dr. Sinan Bilikmen

Nisan 2005, 136 sayfa

Amacımız, yarıiletken ve metal yüzeylerin lazer yardımıyla oksitlenmesi için bir yöntem geliştirmekti. Lazer ile oksitlemenin avantajlarından birisi, lazer ışınının çok ince bir yüzey tabakası içerisinde soğurulması gerçeği ve diğer avantajı ise oksitlemenin bölgesel olarak yapılabilmesidir. Buna ilave olarak, diğer işlemler aracılığıyla ulaşılamayan bazı bölgelere lazer ile ulaşmak mümkündür. Bu sebeplerden dolayı, 1064 nm dalgaboyunda çalışan Nd:YAG darbeli lazeri, Si ve Ta ince filmini oksitlemek amacıyla kullanılmıştır.

İlk olarak, farklı oksijen basıncı ve lazer güçleri için SiO$_2$ tabakaları elde edildi. SiO$_2$ tabakalarının kalınlığı, kırıcılık indisi, yapısı, dielektrik, elektrik ve opriksel özellikleri belirlenmiştir. Lazer gücü için, yüzey erimesi olmadan oksitlenmenin oluştuğu, bir aralığın bulunduğunu tespit ettik. Oksitleme işlemi, alttaş sıcaklığından (673 − 748 K) daha ziyade lazer gücü tarafından kontrol edilir.

Mümkün olabilen yüksek alttaş sıcaklıklarında ve 3.36 J/cm^2 değerinden daha yüksek olan lazer gücünde büyütülen oksitin, daha iyi film kalitesine sahip olduğu durumu bulunmuştur.

İkinci olarak, Ta$_2$O$_5$'nin yüksek dielektrik sabiti, yüksek kırılma voltajı ve nispeten küçük olan kaçak akım değerleriyle SiO$_2$'nin yerini alabilecek en iyi adaylardan birisi olması sebebinden dolayı, rf-sputter yöntemiyle elde edilen Ta tabakaları lazer kullanılarak oksitlendi. Alttaş sıcaklığının, ara-durum oksit değerleri az olan daha yoğun tabakalar elde etme bakımından önemli bir parameter olduğu ve yaklaşık olarak 350^{0}C ile 400^{0}C arasındaki alttaş sıcaklığının en uygun alttaş sıcaklığı olduğu bulunmuştur. İnce filmler (20 – 25 nm kalınlığa kadar) 350 ile 400^{0}C arasındaki alttaş sıcaklığında büyütüldüğünde ve kalın filmler (40 nm) ise 300 ile 350^{0}C alttaş sıcaklığında büyütüldüğünde, β – ortorombik kristal yapısına sahip olduğu sonucu elde edildi. Lazer ile büyütülen ince tantalum oksit filmlerinin kırıcılık indisi değeri 1.9 ile 2.2 arasında değişmekte olup bulk Ta$_2$O$_5$'ın kırıcılık indisi değerine (2.0 – 2.2) oldukça yakındır. Oksit kalınlıkları, düzgün Gaussian şeklinde olup başlangıçtaki Ta filminin yaklaşık olarak iki katı kalınlıktadır. Etkin dielektrik sabiti değerleri, alttaş sıcaklık değeri 250^{0}C'den 400^{0}C'ye artırıldığında, yaklaşık olarak 26'ya ulaşmıştır. Kaçak akım yoğunluğu seviyesinin artan alttaş sıcaklığı ile azaldığı gösterilmiştir. Buna rağmen, filmlerin kırıcılık indisi değerleri ısıtılarak büyütülenlerinkinden daha küçüktür. Düşük kırıcılık indisinin sebebi, lazerle oksitleme esnasında elde edilen yapının gözenekli olmasından kaynaklanıyor olabilir ve oksitleme sonrası ısıtma işlemleri aracılığıyla iyileştirilebilinir.

Anahtar kelimeler : SiO$_2$, Ta$_2$O$_5$, Nd:YAG lazer ile oksitleme, XPS, MOS yapılar, yansıma ve kırıcılık indisi.

To My Lovely Parents and Especially for my son, Alkım…

ACKNOWLEDGMENTS

TABLE OF CONTENTS

LIST OF FIGURES

LIST OF TABLES

CHAPTER 1

INTRODUCTION

1.1 Introduction

One of the most important issues in modern microelectronics is to fabricate dielectric layers with enhanced capacitance properties to meet the requirements of the high density dynamic random access memories (DRAMs). The decreasing size of electronic devices requires high quality thin films, for example, in the case of Metal-Oxide-Semiconductor (MOS) capacitors the oxide barrier must have high dielectric constant and should be defect free [1]. Two directions can be defined in the research activities concerning the production of these films: i) fabrication of ultra-thin and electrically reliable SiO_2 layers on Si substrate and ii) fabrication of alternative dielectrics with high dielectric constant, (high-κ materials). In both cases, however, there is always great interest in novel processing techniques that may, in some way, improve the existing methods of production. There are various methods such as thermal oxidization, a number of various chemical vapor deposition techniques, reactive sputtering, pulsed-laser deposition, and laser assisted oxidation to oxidize the semiconductor surfaces [2].

The conventional methods for oxidation involve the use of furnaces to heat the samples to high temperatures ($\approx 1000^0C$) for sufficiently long enough times. Unfortunately this high temperature furnace heating of the entire sample and oxidation of the whole surface may be undesirable for certain device fabrications. Therefore, one great advantage of laser annealing is that the laser radiation is

heavily absorbed in a thin surface layer, a few hundred to several thousand angstroms in the surface.

There are other novel oxidation methods for local oxidation like AFM oxidation [3]. However, the writing speed of AFM might be slow for the application in the industrial scale. The multiple piezo scanners might be used to decrease the writing time. The diameter of piezo tubes restricts the number of piezo scanners on the wafer. On the other hand, the multiple lasers with beam alignment optics can be used to write on the Si.

Among all these methods, laser oxidation has attracted special attention due to its ability to induce localized oxidation with good spatial resolution and ability to achieve a good control over the thickness of very thin layer of 1-2 nm at low processing temperatures [4-8], i.e. one of the most important techniques for thin film growth. The other important reasons can be given as that it is the most suitable one reaching into some areas that other processes cannot be done. Therefore, laser oxidation has potential for novel applications where a local processing is needed. An example would be applications emerging in the field of nanotechnology where nanostructured Si surface is needed to fabricate device like waveguides. Even though today's conventional microelectronics industry does not use the local oxidation, this does not mean that it will not be needed in the future. With the growing industrial techniques, the advance of laser technology will supply well-controlled laser beam which facilitates oxidation in a more accurate and better controlled way.

The effectiveness of pulsed laser annealing in removing lattice damage and restoring crystalline order in semiconductors has already been reported [9]. The ultrarapid melting and resolidification sequence by pulsed laser has been extensively studied with a variety of time resolved optical [10], electrical [11] and X-ray [12] techniques.

After the pulsed laser annealing, some researchers established that cw lasers could also be used for annealing [13]. However, cw laser annealing differ from pulsed

laser annealing in some respects, i.e., the characteristic time is much longer and melting is not generally allowed to occur. Typical time of the laser beam incident on a spot of the sample during cw laser annealing process is of the order of ms and the surface temperature is held below the melting point in order that solid phase epitaxial regrowth occurs. Investigations of cw laser induced recrystallisation show that the physical mechanisms of regrowth are in many respects similar to those of furnace annealing.

1.2 Advantages of laser oxidation

There are a various applications of lasers such as deposition, evaporation, alloying, plasma formation, welding, cutting, crystallization, annealing, oxidation, laser writing. The most important properties of lasers are its directionality and collimated nature with a very low angle of divergence. As a result of these properties, the large amounts of energy can be easily collected, propagated very large distances from its source without any lost, directed onto any desired location and focus to extremely small dimensions. Depending on the quality of the optics used, the spot size of the focused laser beam can be as small as the wavelength for a single mode laser beam [4]. On the other hand, traditional light sources cannot compete with this regime.

Advantages of laser processing can be given in short remarks as followings;
- not limited processing area to the traditional planar structural configurations of many technologies; quite possible for three dimensional structures,
- giving the user some degree of control over the process and the actual processing depth with the choice of tunability of laser wavelength,
- reductions in the amount of high temperature processing,
- used in direct formation of microstructures and therefore an alternative to forming patterns by conventional lithographic methods.

The main advantages of laser oxidation, here, can be realized as;
- ❖ oxidation at relatively low substrate temperatures,
- ❖ small area oxidation in a way of controlled dimensions,

❖ laser beam scanning the required area with a suitable velocity by using a two dimensional scanner system.

1.3 Why do we need to heat the Si substrates before oxidation by laser?

Various laser sources (Ar[5], CO_2 [6], ruby [7], excimer [8]) with continuous or pulsed beams have been used to process Si or metal surfaces for the oxidation, and successful growth of thin oxide layers has been demonstrated.

Pulsed Nd-YAG laser operating at 1064 nm has recently been applied to an oxidation of metal surfaces for obtaining high-κ dielectrics [14]. The emitted laser energy is 1.165 eV at 1064 nm, which is slightly over the bandgap energy of Si crystal, the absorption by the Si surface is then expected to be weak due to limiting value of the photon energy. On the other hand, high peak energy pulses of Nd:YAG laser beam usually result in melting of the surface [15]. In an interesting study [15], the effect of 266 and 1064 nm Nd-YAG laser pulses on the Si morphology and the mechanisms of melting have been carried out. So far, observation of high quality SiO_2 on Si grown by Nd-YAG laser has not been reported, although there are investigations devoted on its annealing effects [15,16]. The question here is, whether or not an efficient oxidation can be achieved without causing an undesirable deformation of the surface. We observed the formation of thin SiO_2 layer on Si surface by pulsed Nd-YAG laser scanned over a predefined region and demonstrated the successful oxidation of Si surface with a laser power, which is slightly smaller than needed for surface melting.

In fact strong absorption occurs around 1.1 eV which corresponds to the energy difference between the bottom of the conduction band and the top of the valance band. This transition is defined as indirect transition since these points are displaced in momentum space. Therefore phonons are required to balance the difference in momentum. Because the presence of phonons is necessary for the transition, it is expected a strong temperature dependence for this process being occurred. In order to eliminate the formation of slip dislocations on the surface by reducing the large lateral temperature gradients and increase the absorption

coefficient by enhancing the free carrier generation for the infrared wavelength region, silicon wafer needs to be preheated to the substrate temperatures of at least 400^0C [4,6].

As a result, Si sample needs to be heated to a certain temperature for the two reasons before the laser light has been sent on it for the oxidation purposes. These reasons can be given as;

1. Since the Si is an indirect gap semiconductor, the phonons should be included for the 1064 nm laser light.
2. In order to decrease of the slip dislocations, Si wafer need to be heated around 400^oC previous to the laser oxidation [4].

The other important parameters were studied very carefully to obtain a qualitative oxide during this work. These parameters can be given as in the following form;

i. substrate temperature,
ii. thickness of the oxide film already present on the surface of the material,
iii. level of the oxygen gas,
iv. energy density of the Nd-YAG laser.

1.4 The importance of SiO$_2$

Laser oxidation of Si surface has been of interest because of its local and low temperature processing conditions. Local oxidation might be a desirable ability in the development of new microstructures and it can only be achieved by laser oxidation. We investigated the use of Nd YAG laser in the oxidation process.

At the first stage, Si was chosen for laser oxidation process because it is the most studied material and all characteristics relating to the Si and SiO$_2$ interface, and oxide layer are explored. Even though various forms of silicon oxide exist, the silicon dioxide, SiO$_2$, is the most important one. Since its resistivity is very high (higher than 10^{16} Ohm-cm), it has very important electrical parameters making it an excellent insulator. These properties can be given as;

i.   dielectric breakdown strength > 10 MV/cm,

ii.   surface states < $10^{11}/cm^2$,

iii.   chemically very stable.

Oxidation of Si by Nd YAG laser is interesting both from technological and scientific point of view. The wavelength of the laser is 1064 nm (~1.166 eV) which is very close to the bandgap energy of the Si crystal. The absorption of the light is expected to be weak for this wavelength value. It is interesting to know how Si surface reacts to the laser irradiation and see if the oxidation takes place with a light whose wavelength is close to the Si bandgap.

1.5 The importance of Ta_2O_5

Dielectrics like SiO_2 and SiN are widely used in a variety of areas in integrated circuit fabrication. At the same time, the device dimensions in semiconductor industry are shrinking from 0.5 μm in 1992 to 0.35 μm in 1995; 0.25 μm in 1998 and the tendency is the minimum feature size to be $\leq$ 0.1 μm about 2007-2010. On the other hand, the power supply voltage has dropped from 5 to 3.3 V, with another drop to 2.2 V and now it is about 1.5 V. The focus of activity in dielectrics is the development of high dielectric constant materials like single metal oxides in order to increase the packing density for the needs of sub-microelectronics, without reducing the insulator thickness. The main attraction of metal oxides is their relatively high dielectric constant which ranges from 10 to 100 depending on the material microstructure and crystalline phase. The conventional SiO_2 and SiN films have reached their physical limits, since the direct tunneling current increases drastically below 4 nm thickness.

Recently, some metal oxide materials have been widely researched as alternative dielectric layers to SiO_2 – based insulators in VLSI (Very Large Scale Integrated) and ULSI (Ultra Large Scale Integrated) circuits. Among them Ta_2O_5 appears to be the most promising candidate to replace SiO_2 because of its high dielectric constant, high breakdown voltage and small leakage currents [17,18].

This study was motivated by the extended applications of laser annealing in the last decade as advanced technologies for the surface modification of materials. Some dielectric materials, i.e., SiO_2, SiN, Ta_2O_5 have some special interest because of their dielectric properties. However, the electrical characteristics of these materials greatly depend on the oxidation conditions and on the subsequent annealing. On the other hand, laser oxidation seems to be of special interest as a technique to overcome some problems of traditional furnace oxidation. Therefore, the laser beam was used on silicon substrates in oxygen atmosphere to obtain SiO_2 material. Later, the thickness and the refractive index of SiO_2 on Si substrate was investigated. For electrical characterization, a metal on SiO_2 through a shadow mask was evaporated. The electrical and dielectric characteristics of the SiO_2-Si structure were defined by capacitance-voltage, current-voltage and oxide breakdown voltage, V_{bd}. After optimization of the laser oxidation system, it was continued to the oxidation process by thin Ta film.

For some of the films, the elemental composition and the chemical bonding were analyzed by means of X-Ray Photoelectron Spectroscopy (XPS). The structure of the oxidized films was investigated by X-Ray diffraction. The electrical properties of the layers have been obtained by the admittance, i.e. high-frequency Capacitance-Voltage (C-V) and Conductance-Voltage (G-V) techniques and Current-Voltage (I-V) measurements of Metal-Oxide-Silicon (MOS) structures.

Stoichiometry of the layers has been determined by XPS which is a very sensitive, direct and reliable technique in studying the chemical structures on the surfaces with sufficiently good accuracy. XPS has been performed as a function of depth from the surface. In addition to the XPS measurements, we have also ellipsometry results giving some idea about the structures of the grown oxide. We used the FTIR measurement techniques in order to obtain information about the chemical and structural properties of the grown oxides.

This work is a part of the international collaboration project between METU Physics Department and Bulgarian Academy of Science, supported financially by TÜBİTAK. Some of the works have been carried out during mutual visits to

METU and BAS. XPS and reflectance measurements were carried out at BAS. FTIR, ellipsometry, MOS and XRD measurements were done at METU.

We believe therefore that this work does bring a new contribution to the knowledge accumulation to the science and technology of Si oxidation. Besides, laser oxidation might be applied to other materials and the knowledge on Si oxidation will form the basis for these new research activities with other materials.

The main structures of the other chapters can be given in the following order;
The theory of the MOS capacitor structures is given in chapter 2. The experimental details are given in Chapter 3. The thickness distribution, electrical and optical properties of Nd:YAG laser grown Si oxides' results are examined in details in chapter 4. The XPS depth profile results of laser grown Si oxides are given in Chapter 5. Structural and optical characteristics of tantalum oxide grown by Nd:YAG laser oxidation ıs examined in Chapter 6. Thickness profile and electrical properties of tantalum oxide films grown by Nd:YAG laser oxidation ıs given in Chapter 7. Chapter 8 gives an overview about the conclusion.

CHAPTER 2

THEORY OF LASER ASSISTED OXIDATION
AND MOS CAPACITOR STRUCTURES

2.1 Laser – Matter Interaction

Laser radiation (from UV to IR) mainly interacts with the electrons, and sometimes but with a lower probability, with the atomic vibrations or phonons of an atom or atom system.   The electromagnetic radiation does neither induce nuclear disturbances nor affect the energy levels of the inner core electrons of an atom. However, it interacts only with the outer (bound or free) valance electrons of the atoms. After the interaction of laser radiation with matter, the optical properties of the system will be affected. The laser excitation with matter can be examined in different groups depending on the interacting material's physical condition, i.e. being in the gas or solid form.

2.1.1 Laser Excitation of Gas Species

Atomic and molecular species when compared to solids exhibit a small number of excited states which are easily accessible by optically induced transitions. The allowed transitions among the rotational, vibrational and electronic levels result in a series of discrete and sometimes narrow lines in the absorption spectrum of most gases. In order to have vibrational spectra, a change in the dipole moment during the motion is required and accordingly, the coarse structure of the energy levels of the corresponding system is affected. On the other hand, the molecules possessing a permanent dipole moment can exhibit a pure rotational spectrum and the fine

structure of the energy levels of the atom system is affected by the rotational changes. However, electronic spectra are exhibited by all molecules. As a result of optical excitation, stable but reactive species or complete dissociation into a volatile radical are the possibilities for an atom or molecule system [4].

2.1.2 Laser Interaction with Solids

2.1.2.1 Metals

The radiation is absorbed by the outermost electrons of the atoms of solid materials. As commonly assumed, metals are characterized by their loosely – bound outermost electrons. Since these electrons are defined as free to travel around from atom to atom, "*free electron gas*" model is quite successful for characterizing the metals. According to the calculations of dielectric response of this model, a plasma frequency, ω_p, is obtained. Electrons of a plasma can resonantly oscillate in an undamped form at this plasma frequency, ω_p;

$$\omega_p = \frac{e}{2\pi}\sqrt{\frac{N_e}{m_e \varepsilon_0}} \tag{2.1}$$

where N_e is the number density, m_e is the mass, e is the charge of the electrons and ε_o is the dielectric constant of free space with the value of 8.85 x 10^{-12} F/m. This free electron gas system interacts with the radiation depending on the frequency of the interacting beam.

i) At low radiation frequencies (Longer wavelengths);

At the radiation frequencies lower than the plasma frequency, free carriers in the material characterize the absorption. Free electron model totally controls and characterizes the absorption characteristics of various metals like Hf, Co, Pt, Fe, Pd, W, Ta, Kr, Mo, V, Cr and Ni when the radiation frequency is higher than 1 μm [19,20]

The slope of the fitted lines of absorption versus wavelength gives 2 and therefore, the absorption results in an inverse proportionality to the square root of the frequency of the radiation. The "skin depth" is defined as the absorption depth (the inverse of the absorption coefficient) and found from the extrapolation of the absorption versus wavelength relationship to the lower frequencies.

ii) At increased radiation frequencies;

Both the absorption and reflectivity decrease as the wavelength of the incident radiation decreases. On the other hand, no any accurate analytical approximations can be made for the optical properties of the metal in this regime. Therefore, the band structure of the individual material together with the plasma frequency defines precisely the minimum position of the reflectivity and absorption.

iii) At the very high radiation frequencies;

At this regime, there exists an extremely small free carrier contribution to the optical properties. Accordingly, the metal exhibits characteristics related to the lattice properties and interband absorption occurs for most of the metals at this regime.

Other than the plasma frequency edge, the condition of the metal's surface is very important for the optical reflectivity. Thin films can be given as an example that they exhibit higher reflectivity values than their highly polished bulk counterparts. Optical properties are also affected from the presence of impurities, a surface oxide, and a particular surface finish.

After the energy is coupled from the laser beam into the electronic system of the metal, it is redistributed among the electrons of the metal system and eventually to the lattice system by various scattering processes during the time durations of the order of picoseconds or less. Since the photon energy is converted into the random atomic motions, the metal is rapidly heated. The rate of supply energy is proportional to the beam flux and the duration of the exposure.

2.1.2.2 Insulators and Semiconductors

The allowed energy levels of electrons in insulators and semiconductors are grouped into bands and these energy bands are separated that electrons cannot be in the forbidden energy gaps [21]. The highest energy band that is completely filled by electrons at 0 K is named as the *valance band* and the next higher energy band separated by a forbidden gap (E_g) from the valance band is called the *conduction band* (Figure 2.1).
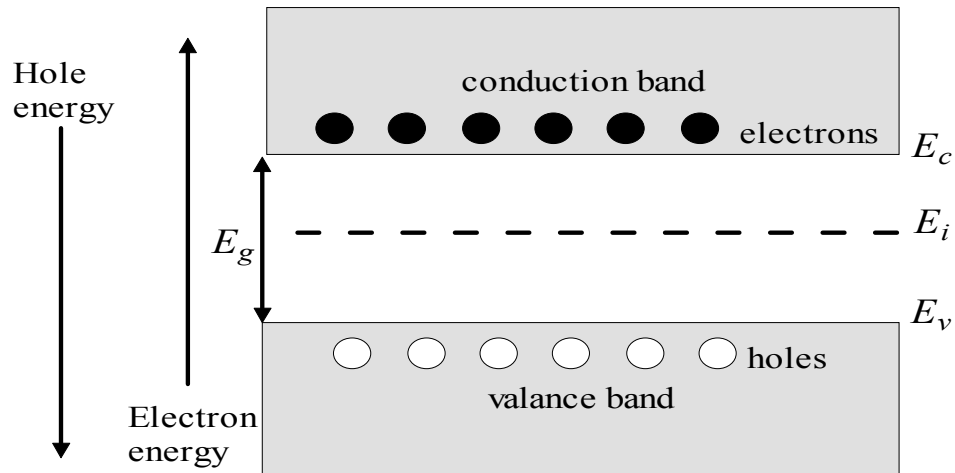
Figure 2.1 Energy band diagrams for semiconductors.

When the value of E_g is around 9 eV, then the material is a very strong insulator. However, if E_g is closer to 0 eV, the material is defined as a narrow-bandgap semiconductor. Even it is not a solid line, a value around 5 eV is generally considered to be the lower limit for insulators.

No electrical conduction is possible when there are no electrons in the conduction band and the valance band is completely filled by electrons at 0 K. However, a small fraction of electrons are excited into the conduction band leaving vacancies, or holes, in the valance band at room temperature when the bandgap is small

enough. Therefore, a limited amount of conduction occurs because of a small amount of electrons in the conduction band and the holes in the valance band. Nevertheless, this room temperature conduction is impossible for insulators that have several eV of bandgap energies.

In order to have electronic transitions between the valance and conduction band by means of a laser radiation, the photon energy should be greater than the bandgap energy, E_g, of the semiconductor, i.e. hν > E_g. Both semiconductors and insulators behave like metals at wavelengths above their individual band edges. When the photon energies are below the E_g value, much weaker intraband electronic transitions and the excitation of specific vibrational modes within the lattice determine the optical properties of these materials.

Si has an indirect bandgap energy semiconductor and strong absorption occurs around at 1.12 eV which corresponds to the energy difference between the bottom of the conduction band and the top of the valance band energy level. Since it is an indirect gap, bottom of the E_c and the top of the E_v are displaced in momentum space. Therefore, this transition requires the existence of phonons to conserve the momentum. Since the presence of phonons is necessary for the transition, then a strong temperature dependence of this process is expected. Accordingly, when the temperature is increased, the transitions can occur from the deeper levels of the energy bands resulting in a much stronger absorption since the density of states is significantly higher. Direct transitions, not requiring phonon assistance for Si, occur for the photon energies higher than 3.4 eV (360 nm wavelength).

The photon energy of Nd:YAG laser at 1064 nm corresponds to ~ 1.17 eV. However this value is higher than the required energy for the bandgap of Si (1.12 eV), it is not enough to make direct transitions because Si is an indirect bandgap material. Since the photon energy is less than the intrinsic absorption edge, the generation of electron-hole pairs by single photon absorption is not energetically possible and, therefore, the sample needs to be heated optically for the absorption. The absorption is dominated by free carrier transitions for this situation. There are two possible ways to increase the carrier density in the semiconductors;

i) heating the lattice

ii) irradiating the material with a laser having a photon energy greater than the bandgap energy.

Since the first procedure will be used in our case, the presence of phonons is inevitable for the transitions with the below bandgap edge for Si.

Since the radiation wavelength is large compared to the interatomic dimensions, macroscopic optical constants, i.e. the refractive index n and the extinction coefficient k, $k = \dfrac{\alpha\lambda}{4\pi}$ where α is the absorption coefficient of the material at the wavelength λ, can describe the optical properties of the solid. The optical properties of a material can be related to the complex dielectric constant $\varepsilon = \varepsilon_1 + i\,\varepsilon_2$ and the conductivity σ of the medium by using the Maxwell's equations;

$$n^2 - k^2 = \frac{\varepsilon_1}{\varepsilon_0} \tag{2.2}$$

$$2nk = \frac{\varepsilon_2}{\varepsilon_0} = \frac{\sigma}{\omega\varepsilon_0} \tag{2.3}$$

where $\varepsilon_1 = \dfrac{D}{E}$ and $\sigma = \dfrac{J}{E}$ with ε_0 the permittivity of free space, D the electric displacement, E the electric field and J the current density. According to these equations, n and k values can be obtained with the knowledge of ε_1, and ε_2 (or σ) and the reflectance coefficient R at normal incidence is given by

$$R = \frac{(n-1)^2 + k^2}{(n+1)^2 + k^2} \tag{2.4}$$

When the transitions are confined to within the conduction band, or within the valance band, free carrier absorption can be defined. Free carrier absorption depends on the density of free carriers, their mobility, and the number of available states within the band.

Free electrons or holes can be successfully described as particles of a gas and the following equations are obtained by solving the classical equation of motion of a free carrier by means of Drude model in terms of the effective mass, m^*;

$$2nk = \frac{\sigma_0}{(1+\omega^2 t^2)\omega \varepsilon_0} \tag{2.5}$$

$$n^2 - k^2 = \frac{\varepsilon_L}{\varepsilon_0} - \frac{\sigma_0 \omega t}{(1+\omega^2 t^2)\omega \varepsilon_0} \tag{2.6}$$

where $\sigma = \frac{N e^2 t}{m^*}$. Here t is the relaxation time, N is the carrier density and ε_L is the dielectric constant of the lattice. The following approximations can be done for the low conductivity materials, i.e. *for semiconductors and insulators*;

$$n^2 - k^2 = \frac{\varepsilon_1}{\varepsilon_0} = \frac{\varepsilon_L}{\varepsilon_0} \tag{2.7}$$

In other words, $\varepsilon_1 \cong \varepsilon_L$, i.e. the contribution of the electrons to the dielectric constant is negligible. For low conductivity, the following approximations can also be done;

$$n^2 - k^2 > 2nk \tag{2.8}$$

Accordingly, it is also correct that $n > k$ and therefore, $n \cong \frac{\varepsilon_1}{\varepsilon_0}$. A value for the absorption coefficient due to free-carrier absorption using these assumptions can be given as;

$$\alpha = \frac{\sigma_0}{1+\omega^2 t^2} \sqrt{\frac{\mu_0}{\varepsilon_L}} \tag{2.9}$$

where μ_0 is the permeability of free space.

i) At low frequencies;

Following approximations are followed at this limit;

$$1 + \omega^2 t^2 \rightarrow 1 \tag{2.10}$$

Therefore,

$$\alpha \cong \sigma_0 \sqrt{\frac{\mu_0}{\varepsilon_L}} \tag{2.11}$$

It is shown that the absorption is frequency independent at low frequencies.

ii) At high frequencies;

The high frequency approximation is given in the following form;

$$1 + \omega^2 t^2 \rightarrow \omega^2 t^2 \tag{2.12}$$

Therefore, the absorption coefficient is proportional to the square of the wavelength. The absorption coefficient as a function of the photon energy can be found in general in the Si technology based semiconductor books [4].

2.1.2.3 Plasma Formation

When extremely high intensity and ultrashort laser pulses are used, formation of dense plasma above the surface of many materials is induced. This process starts with the radiative heating of free electrons within the solid by the intense laser pulses. The electrons are accelerated in a strong manner by coupling to and absorbing the incident radiation. Since these strongly accelerated electrons collide with ions and various gas–phase atoms, then more atoms are ionized and the more increased rate of ionization occurs. As a result of rapid formation of an electron gas, a shielding layer occurs on the surface of the material. This technique is named as laser pulsed plasma chemistry (LPPC) and used to induce the growth of thin oxide layers on the surfaces of the films [22]

2.2 Possible Laser Oxidation Mechanisms

Typical oxidation process of Si surface contains three steps [23 and references therein];

16

i) transport of the oxygen species to the oxide surface,

ii) diffusion through the oxide,

iii) reaction with Si at the Si – SiO$_2$ interface.

Laser beam can take place in the oxidation process with two possible mechanisms : It can either react with the oxygen molecules filling the vacuum chamber in a controlled gas pressure or interact with the Si surface. In the former case, photodissociation of O$_2$ molecules occurs at temperatures higher than 50^{0}C [24,25]. Threshold for photodissociation of O$_2$ molecules is around 5.1 eV (~ 242 nm) and as a result of this process highly reactive O species are created [26].

The wavelength ranges to create the various types of active oxygen atoms from O$_2$ molecules can be given in the following form [27];

1. 200 nm $< \lambda <$ 242.4 nm:

   $O_2 + h\nu \rightarrow O(^3P) + O(^3P)$

   ΔH_o=493.56 kJ/mol

2. 137 nm $< \lambda <$ 175 nm:

   $O_2 + h\nu \rightarrow O(^3P) + O(^1D)$

   ΔH_o=683.38 kJ/mol

3. 110.6 nm $< \lambda <$ 134.2 nm:

   $O_2 + h\nu \rightarrow O(^3P) + O(^1S)$

   ΔH_o=897.80 kJ/mol
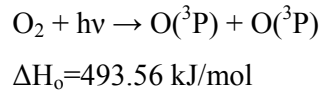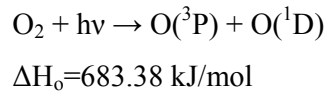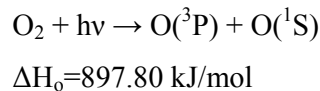
The value of ΔH_o defines the activity levels of created O atoms, and thus the lower wavelength light can produce more active oxygen species leading to a more efficient photo-oxidation reaction.

As an example, the possible oxidants and active species for the wavelength of 193 nm laser light can be given as [28]:

$$SiO^* + SiO \rightarrow Si + SiO_2 \qquad\qquad (2.13)$$

$$SiO^* + O_2 \rightarrow SiO_2 + O_2$$
$$O + SiO \rightarrow SiO_2 \qquad\qquad\qquad (2.14)$$

$$O_2 + h\nu \rightarrow 2O^*$$
$$O^* + SiO \rightarrow SiO_2 \qquad\qquad\qquad (2.15)$$
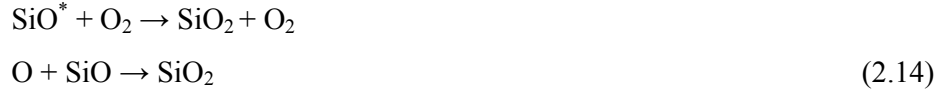
However, the energy of 1064 nm wavelength laser light from Nd:YAG laser is around 1.17 eV. Since the necessary photodissociation energy of O_2 molecules is around 5.1 eV (~242 nm), the 1064 nm wavelength from Nd:YAG laser is well below the photodissociation limit of oxygen molecules. Therefore, there is not even small possibility to crack oxygen molecules to obtain two active oxygen atoms with the used laser wavelength. The laser light, in this situation, can only interact with the Si substrate. Si is an indirect bandgap material having the E_g value around 1.12 eV, and direct transitions occur when the photon energies are higher than 3.4 eV (~340 nm) [See section 2.1.2.2 for details]. Below this energy level, which is the case for 1064 nm wavelength of Nd:YAG laser, Si behaves as an indirect bandgap material and transitions from the valance band to the conduction band are realized only with the participation of phonons. In addition, free carrier absorption occurs with the indirect bandgap transitions in this situation. Therefore, the doping level of Si and the existence of phonons are vitally important parameters for the oxidation of Si surfaces by means of 1064 nm wavelength of Nd:YAG laser.

It is generally hard to distinguish the above mentioned mechanisms experimentally. However, based on the introduction given above, major interaction process that takes place during the oxidation of Si surface by Nd:YAG laser is expected to be the free carrier absorption.

2.3 Introduction to MOS Capacitor Structures

Metal – Oxide – Semiconductor devices are named as MOS devices. Only one type of carrier predominately participates in the conduction process of MOS devices. The MOS capacitors are used as storage capacitors, i.e. switched capacitor filters, semiconductor memory, image sensors in integrated circuits [29,30]. Silicon is

used as the semiconductor material here, but all these concepts apply to any Metal – Insulator – Semiconductor system. A schematic representation of an MOS capacitor is given in Figure 2.2. In this figure, t_{ox} is the thickness of the oxide layer, and V_G is the applied bias voltage. A metal layer is used as the gate electrode.

In conventional scheme, bias voltage V_G is positive when the positive terminal of the bias voltage is applied to the gate and negative when the negative terminal of the bias voltage is applied to the gate. The dielectric constants are $3.9\epsilon_o$ for SiO_2 and $11.7\epsilon_o$ for Si.   Some definitions need to be given at this point before the discussion of MOS capacitors` properties.

Flat Band Voltage: In an ideal MOS capacitor, difference in the metal and semiconductor work function is termed the **flat band voltage** and shown as

$$V_{FB}^0 = \Phi_{Al} - \Phi_{Si}.$$

When the applied voltage to the MOS capacitor is equal to the flat band voltage, the difference in the work functions is exactly compensated and the energy bands do not vary with distance.

Accumulation or Enhancement: Bias conditions which give a majority carrier concentration at the SiO_2 – Si interface greater than the majority carrier concentration in the neutral bulk are called **enhancement** or **accumulation**.

Inversion: Bias conditions which give a minority carrier concentration at the SiO_2 – Si interface greater than the majority carrier concentration in the neutral bulk are called **inversion**.

Threshold Voltage: The bias at which the minority carrier concentration at the SiO_2 – Si interface is equal to the majority carrier concentration   in the neutral bulk of semiconductor is termed the **threshold voltage**. The so called strong inversion occurs at voltages whose magnitude is greater than the threshold voltage.
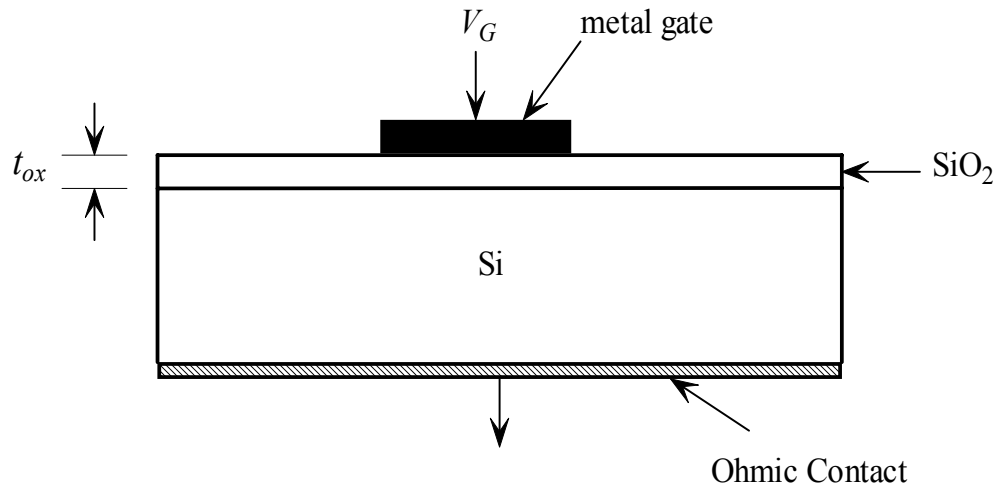
Figure 2.2 Cross section of an MOS capacitor.

2.3.1 Ideal MOS Capacitor

Energy–band diagram of an isolated metal (Al) adjacent to isolated insulator (SiO_2) and isolated semiconductor (p-type Si) with the allowed energies E in the bulk of the material versus position, x, is given in Figure 2.3.

At thermal equilibrium,

- Fermi levels in the Al and semiconductor must be equal,
- Vacuum level must be continues.

These two requirements give the energy band diagram for the ideal MOS capacitor as in Figure 2.4.

Ψ_s is the voltage drop in the semiconductor, which is also semiconductor band bending. Ψ_s, in definition, is the difference between the intrinsic Fermi level in the neutral bulk and the intrinsic fermi level at the SiO_2 / Si interface. Ψ_s values for different physical conditions for n-type and p-type semiconductors are given in Figure 2.5.
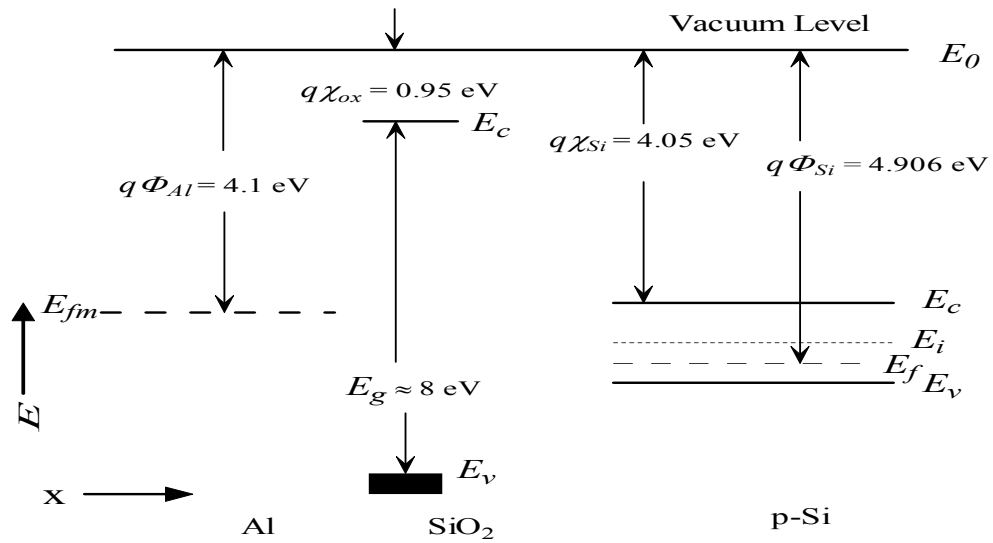
Figure 2.3 Energy levels are shown for the MOS capacitor before initial contact.
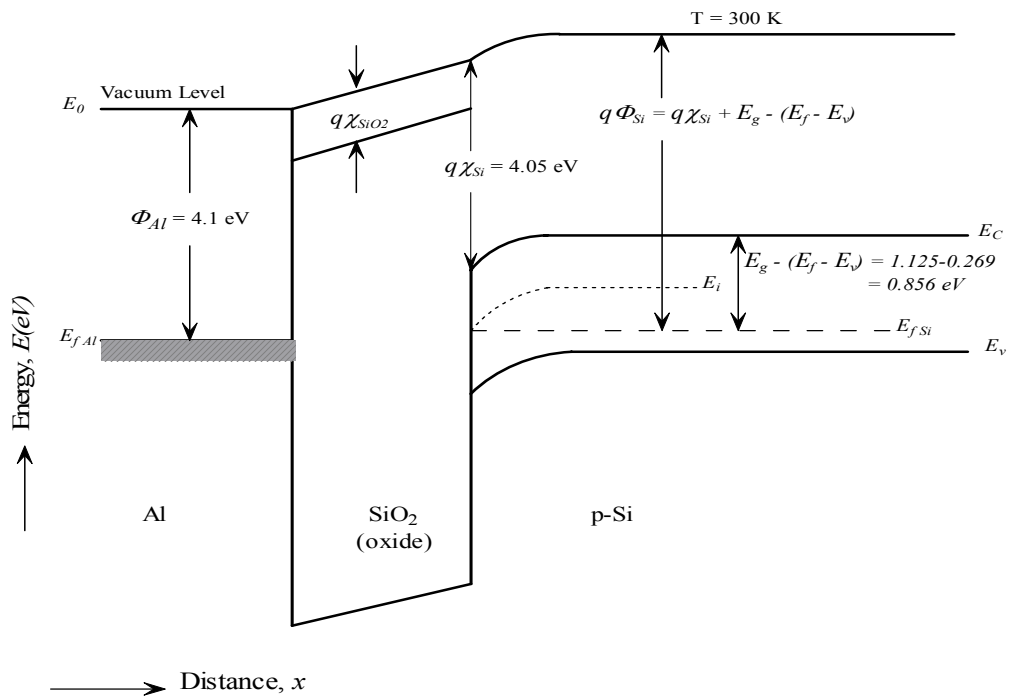
Figure 2.4 Energy band levels are seen for an MOS capacitor at thermal equilibrium.
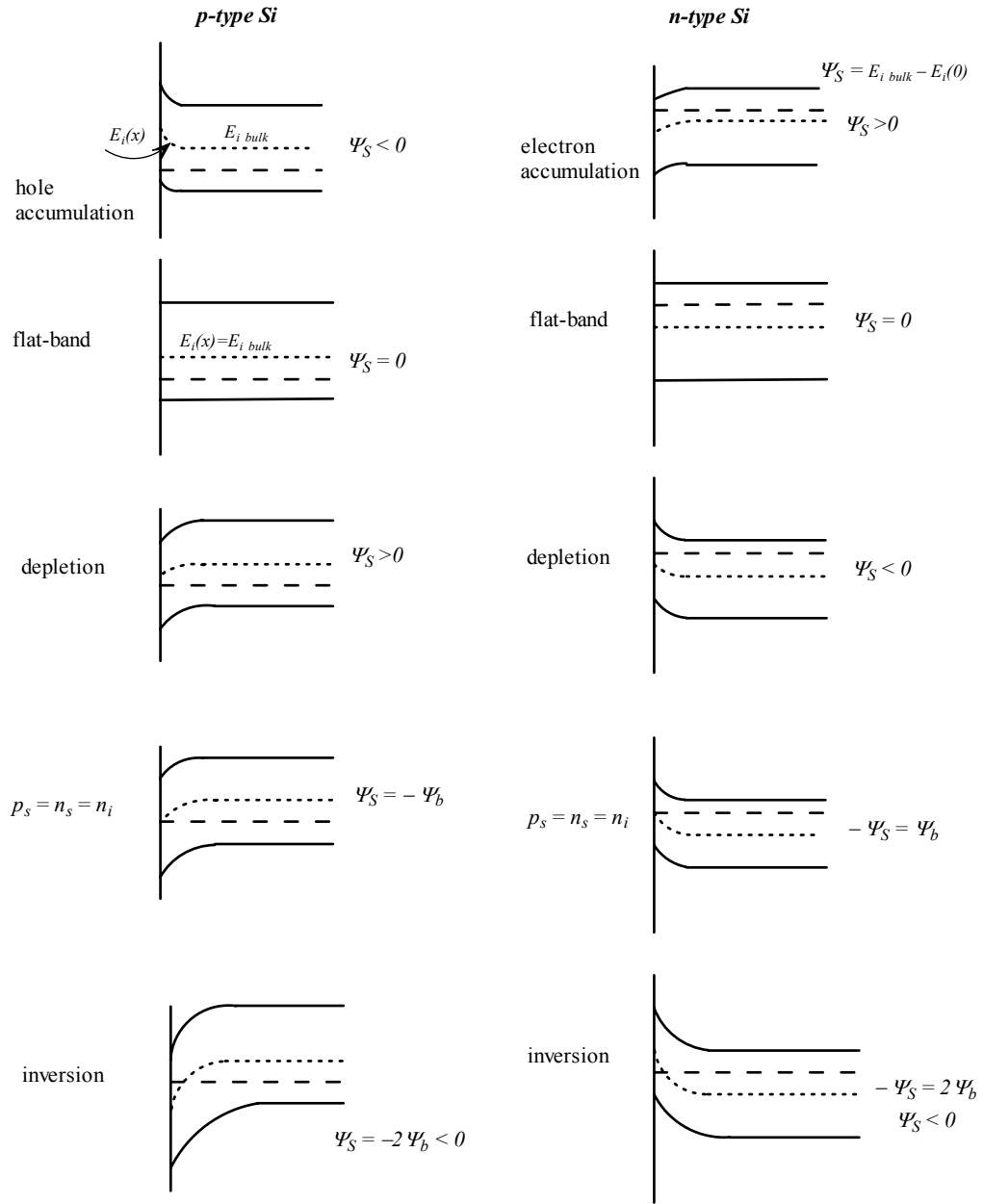
Figure 2.5 Different physical conditions for p-type and n-type semiconductors.

2.3.2 Differential MOS Capacitance

2.3.2.1 Ideal Oxide MOS Capacitance – Voltage Behavior

Definition of the static capacitance is given as $C = Q/V$ where Q is the total charge on the capacitor while V is the applied voltage. For the MOS system, the differential capacitance is defined because the charge on the capacitor varies nonlinearly with the applied gate voltage. Differential capacitance is given as;

$$C_{dif} = \left| \frac{dQ_{Si}}{dV_G} \right| \tag{2.1}$$

After inserting the known equations for V_G, the result for C_{dif} per unit area is obtained as;

$$\frac{1}{C_{dif}} = \frac{1}{C_{ox}} + \frac{1}{C_{Si}} \tag{2.2}$$

with $\quad C_{Si} = \left| \frac{dQ_{Si}}{d\Psi_s} \right| \tag{2.3}$

The schematic view of the capacitance is shown in Figure 2.6. The equivalent capacitance is equal to the series combination of two parallel plate type capacitances corresponding to oxide layer and the silicon depletion layer. For the ideal oxide MOS system, the normalized high frequency C-V behavior for p-type semiconductor is given in Figure 2.7. When the substrate carrier concentration and oxide thickness change, the C-V curve changes, too. This dependence is shown in Figure 2.8 and Figure 2.9, respectively.
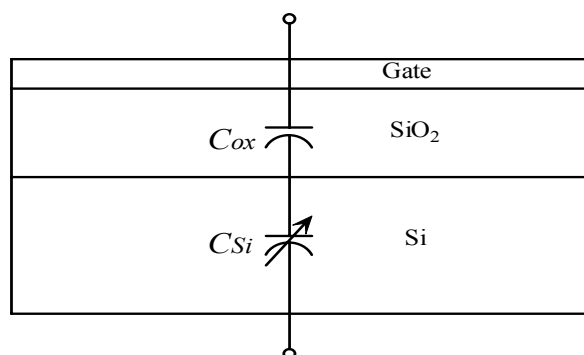
Figure 2.6 Schematic representation of an MOS capacitor as a series combination of the fixed oxide capacitor C_{ox} and the variable Si capacitor C_{Si}.
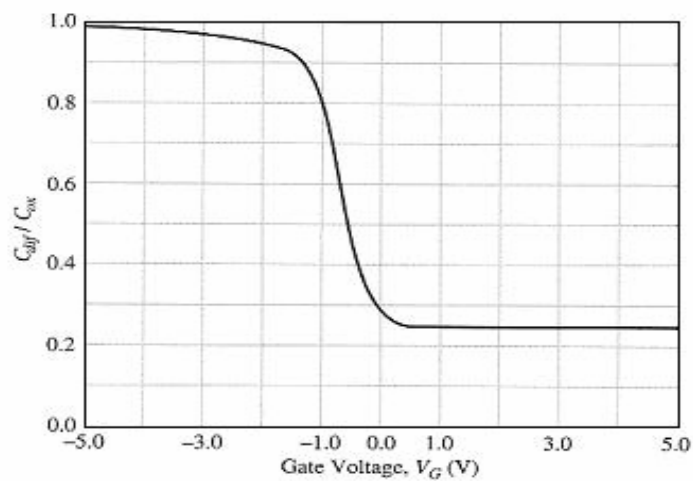
Figure 2.7 Normalized capacitance C_{dif}/C_{ox} is seen for the ideal oxide MOS capacitor on p-type Si with $N_a^- = 4 \times 10^{15}$ cm^{-3} and $t_{ox} = 50$ nm (taken from 30).
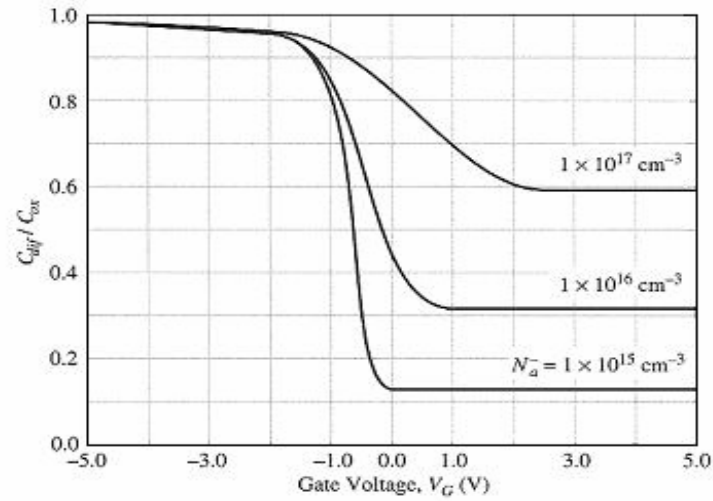
Figure 2.8 Normalized capacitance C_{dif}/C_{ox} is shown for the ideal oxide MOS capacitor on p-type Si with an Al gate and oxide thickness of 50 nm. The substrate hole concentration is indicated on each curve (taken from 30).
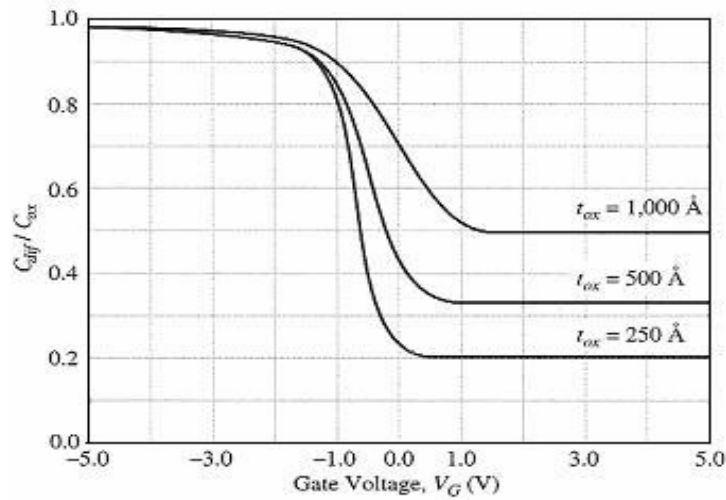
Figure 2.9 Normalized capacitance C_{dif}/C_{ox} is shown for the ideal oxide MOS capacitor on p-type Si with an Al gate and a hole concentration is 1 x 10^{16} cm^{-3}. The oxide thickness is indicated on each curve (taken from 30).

2.3.2.2 Non-ideal Oxide MOS Capacitance – Voltage Behavior

In an actual MOS capacitor, there may be charge within the oxide, or at the SiO_2–Si interface. The charges alter the C – V behavior of the MOS capacitor. There are four types of charges associated with the SiO_2 / Si system. As illustrated in Figure 2.10, these charges are categorized as fixed oxide charge (Q_f), interface trapped charge or fast states (Q_{it}), oxide trapped charge (Q_{ot}) and the mobile ionic charge (Q_m).
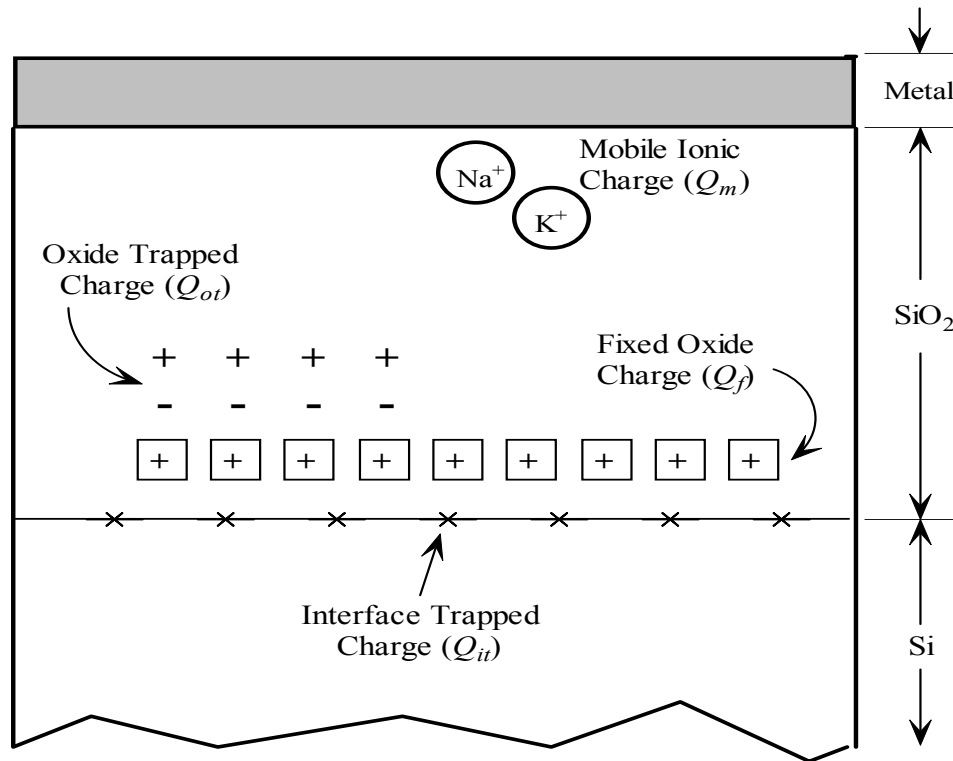
Figure 2.10 Names and the locations of the oxide charges.

The interface trapped charges, Q_{it} and N_{it}, may be positive or negative charges. These charges are due to structural, oxidation-induced defects, metal impurities or defects caused by radiation or similar bond-breaking processes. Since the charge is

in electrical communication with the underlying Si, Q_{it} can be either charged or discharged. Most of the interface charge can be neutralized by annealing at 450 ^{0}C in hydrogen. This interface trapped charge has also been called *surface states*, *fast states*, or *interface states*.

Oxide trapped charge, Q_{ot} and N_{ot}, may be positive or negative due to holes or electrons trapped in the bulk of the SiO$_2$. This trapped charge may result from ionizing radiation or avalanche injection.

Mobile ionic charge, Q_m and N_m, is due primarily to ionic impurities such as Li$^+$, Na$^+$, and K$^+$.

Fixed oxide charge, $Q_f = q\,N_f$, is very near the SiO$_2$ / Si interface and shifts the gate voltage. In this case, flat band voltage and gate voltage is given in the following equations;

$$V_{FB} = V_{FB}^0 - \frac{q\,N_f}{\left(\varepsilon_{ox} / t_{ox} \right)} \tag{2.4}$$

$$V_G = V_{FB}^0 - \frac{q\,N_f}{\left(\varepsilon_{ox} / t_{ox} \right)} + \frac{\left| Q_{Si} \right|}{C_{ox}} + \Psi_s \tag{2.5}$$

As a result of this, the calculated C–V curve is shifted by the change in flat band voltage due to the fixed oxide charge. Figure 2.11 illustrates this behavior for p-type semiconductor.

Since the interface trapped charge, $Q_{it} = q\,N_{it}$, is in electrical contact with the underlying semiconductor it can be charged or discharged. The charge of the fast states will vary with the band bending, represented by Ψ_s. This charge will change the C-V behavior of the MOS system. The C–V curve is distorted from the ideal C–V curve and shown in Figure 2.12.
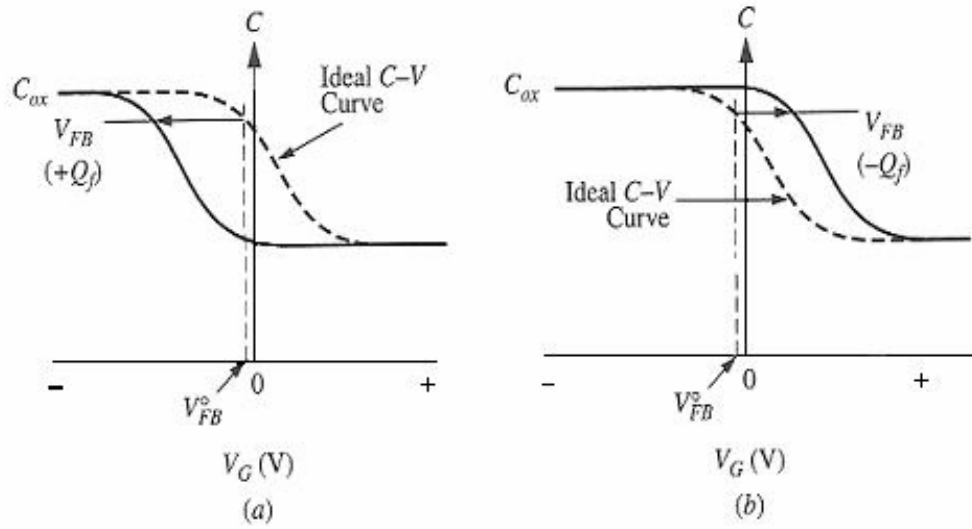
Figure 2.11 Shift of the high frequency C-V curve in a p-type semiconductor for **(a)** positive fixed charge, **(b)** negative fixed charge (taken from 30).
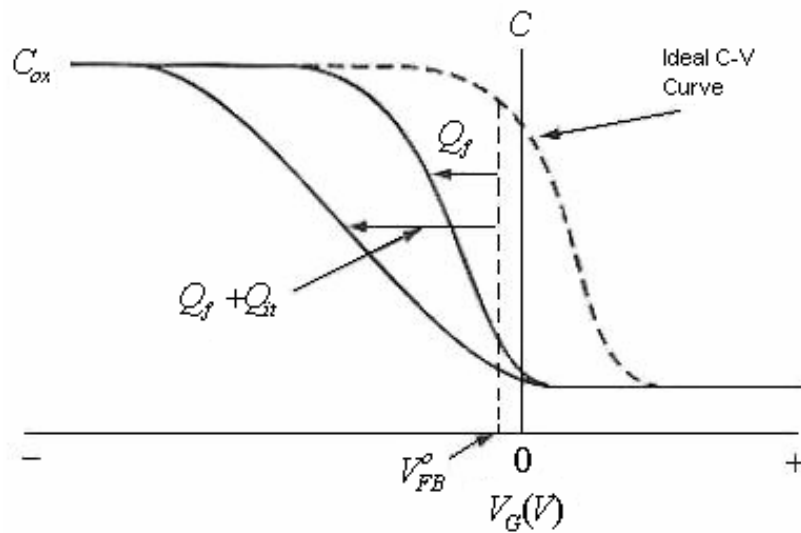
Figure 2.12 Distortion of the ideal oxide C-V curve due to fixed oxide charge and interface trapped charge (taken from 30).

CHAPTER 3

EXPERIMENTAL PROCEDURE

3.1 Introduction

In this chapter, experimental procedures for laser oxidation of Si-surface and Ta thin films are explained. The experimental set-up for laser oxidation has been designed and constructed in this work. It consists of a chamber equipped with substrate heater, water cooling system for the substrate heater, gas control valves, a computer controlled X – Y scanner system and an Nd:YAG laser. Details of these systems and sample preparation are described in the following section.

3.2 Experimental procedure for the laser oxidation of Si surface

The procedure for the laser oxidation of Si surface is described below:

1. p-type Si substrates oriented in (100) direction with the resistivity of 15-17 Ω-cm were used.
2. Samples were cleaned chemically in boiling trichloroethylene and acetone together with the ultrasonic bath of ultra pure water. They were dipped into diluted HF for a few second just before loading them into the chamber. The surface of films was hydrophobic after HF dip showing that the native oxide layer, namely SiO_2, was removed from the surface.
3. The cleaned Si wafer was placed onto the substrate holder of the vacuum chamber evacuated by a mechanical pump to a pressure below 0.133 Pa.

4. Substrate holder was preheated to some degree of high temperatures, T_s, whose value changes between 673 and 748 K.

5. O_2 gas was introduced into the chamber (working gas pressure of 123 Pa) after reaching the desired substrate temperature, T_s.

6. Having attached to a X-Y scanner system, a 3 cm converging lens with a focal length of approximately 25 cm generated a 1.8 mm diameter of spot size on the substrate. The X-Y scanner system was controlled by a computer via its parallel port to direct the laser beam on a certain pre-defined region of Si wafer with controllable dimensions. By means of the scanner system, the laser light shines on a region on the substrate approximately 4 mm x 4 mm and this area can be reduced or increased by software (See section 3.4).

7. The Si wafer was irradiated for certain time durations to oxidize the Si surface. Preliminary experiments showed that at least 20 min oxidation time was needed to be able to obtain measurable oxide layer on Si.

8. The main laser fluence varies in the range 2.65 and 3.51 J/cm^2 per pulse in this study.

9. After the oxidation process of Si wafer was completed, the wafer was taken out of the vacuum chamber to measure the thickness and the refractive index of the oxide layers by using an ellipsometer (λ=632.8 nm).

10. The electrical characterization of the layers was carried out using MOS capacitors with evaporated Al gate electrodes with an area of 1.96 x 10^{-3} cm^2 (see section 3.5 for the details of the construction of MOS capacitors).

3.3 Experimental procedure for the oxidation of Ta layer on Si

The procedures for the oxidation of rf-sputtered Ta layer on Si are given below:

1. p-type Si substrates oriented in (100) direction with the resistivity of 15-17 Ω-cm were used.

2. After conventional chemical cleaning of the wafers, tantalum films with a thickness from 10 to about 20 nm were deposited on Si by rf sputtering of tantalum target (99.99 % purity) in an Ar atmosphere, (the working gas pressure was 3 Pa; rf power density was 2.2 W/cm^2 and the deposition rate

was 9.3 nm/min; the substrate was not intentionally heated during the tantalum deposition and presumably remained at temperatures close to room one).

3. Subsequently, the samples were laser oxidized in vacuum chamber which was evacuated to a base pressure below 0.13 Pa.

4. Before the oxidation, the substrate was heated to temperatures between 250 and 400^0C.

5. O_2 gas was introduced into the chamber (working gas pressure, p, was in the range of 1.2×10^2 – 1.2×10^3 Pa) after reaching the desired substrate temperature, T_s.

6. The main laser fluence varies in the range between 3.16 J/cm^2 and 3.36 J/cm^2 per pulse.

7. The oxide thickness, d, and the refractive index, n, of the oxide layers obtained were initially determined by fixed wavelength ellipsometry, (λ = 632.8 nm); the films with $d \sim 20 - 50$ nm were studied.

8. After optical and structural measurements, the metal oxide samples were used in the construction of MOS capacitors (see section 3.5) to measure the electrical properties.

The laser treatment was carried out using a Nd-YAG radiation at 1064 nm, (EKSPLA Pulsed Laser NL301). Total pulse energy of 320 mJ, pulse duration of 4.7 ns, repetition rate of 10 Hz, and the beam radius of approximately 3 mm circle area were the Nd-YAG laser parameters of our system. The laser beam has a hat-top intensity profile and thermal effects are expected at the irradiated surface [4, 31]. The schematic view of the oxidation system is seen in Figure 3.1, while the photographs are in Figure 3.2.

A scanning electron microscope (SEM) model PhilipsTM equipped with an energy dispersive X-ray spectroscopy (EDX) model EDAXTM was used to characterize the morphology of the specimens and to obtain qualitative information on the elemental composition of the samples, respectively.

The models and the properties the equipment used for the measurements of the laser grown oxides and MOS capacitors are given in details in Section 3.6.
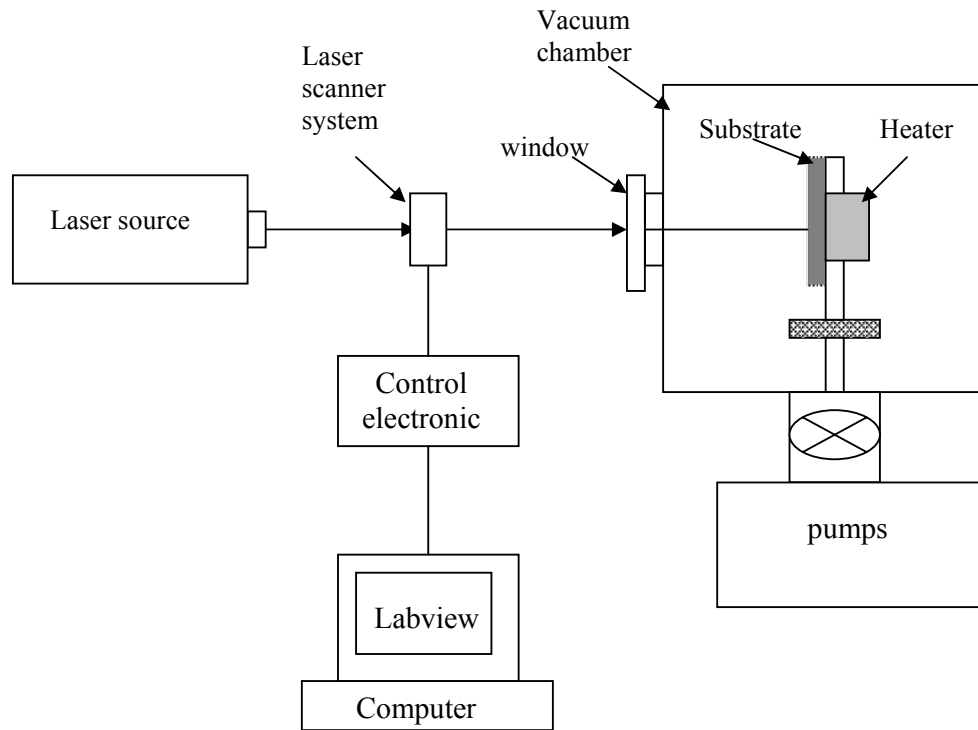
Figure 3.1 The schematic view of the laser oxidation system.

Figure 3.2 Pictures of the laser oxidation system.

3.4 Laser Scanner System

The laser scanner system is designed so as to obtain a controlled and required surface modification by means of scanning the laser beam on the surface. This is also the main difference between this method and other known methods. So with controlled local oxidation process, the specific patterns can be fabricated easily at one time process.

A laser scanner system for two directional (X–Z) scanning by laser beam has been developed in this work. This system is based on focusing with a converging optical lens of the laser beam and scanning with this converged beam onto the surface of the material. In this design, the laser beam falls different points at each time on the lens because of the lens movement, and this effect causes images at different points on the material's surface (Figure 3.3).
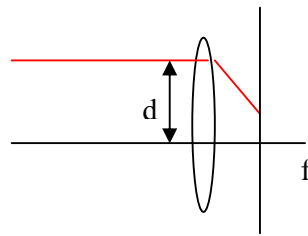
Figure 3.3 Beam line passing through the converging lens.

This scanner mechanism can be analyzed in four main parts. First part is the chassis providing the necessary fixings of all movable parts (Figure 3.4). The second part is the rail providing a motion only in desired direction. The third one is the screw which translates rotational movement to the motors for one-dimensional straight movement. The last part is the movable platform located on the screw and rail to carry lens on (Figure 3.5). This mechanical design of the laser scanner system was constructed together with experimental condensed matter physics research group at İzmir Institute of Technology.

Bipolar stepper motors having 3.6^0 angular step sizes were used. The distance and speed were controlled finely with counting the steps of the stepper motors. LN298 integrated H-bridge bipolar control circuits were used between the computer and mechanical unit of the scanner system. The working scheme of this LN298 integrated H-bridge is given in Figure 3.6. This integrated circuit works with signals coming from parallel port of the computer with a special order and then H-bridge integrated circuit converts 5 V parallel port output signal to 12 V bipolar stepper motor signals with the same order of the computer signals for bipolar stepper motors. The signals should be in the order of 1a, 2a, 1b, 2b where the gates started with 1 and 2 are connected with each other in themselves. The order of these signals can be changed to 2b, 1b, 2a, 1a for the reverse direction of motor movement. Two DC voltage sources, for logical supply and direct power supply of H-bridge, were used. So the scanner system is able to scan the maximum 1.5 cm x 1.5 cm area with minimum 0.01 mm step size with a fine described path.

The other specification of this scanner system is being fully computer controlled. Labview scientific programming language is used. With Labview software, the system can scan a pre-defined area automatically or with manual control. The position of the laser on the material is given in real-time position graph during experiments. The speed of the scan can be controlled. Architecture of this program is based on sending sequential signals to stepper motors. The communication between program and stepper motors is provided by parallel port.
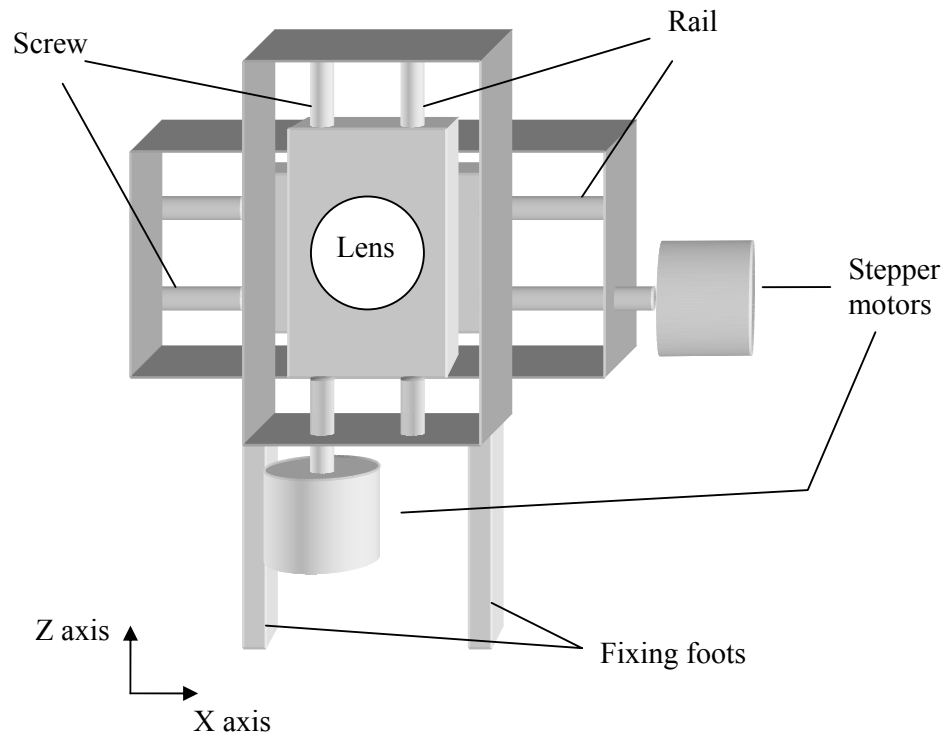
Figure 3.4 The schematic view of the X-Z scanner system.
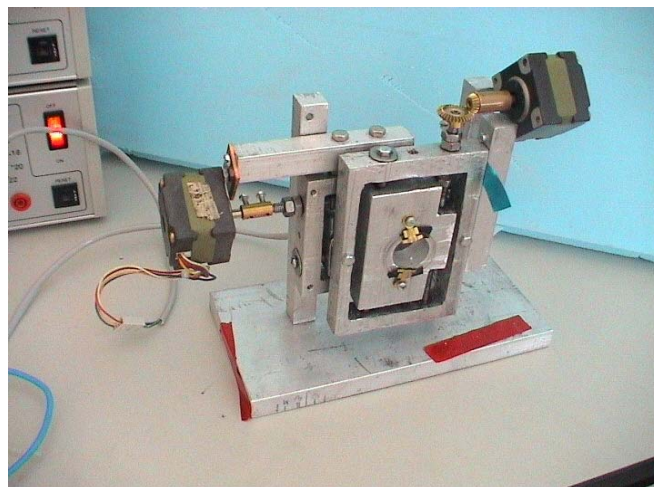
Figure 3.5 Picture of the X-Z two dimensional scanning system.
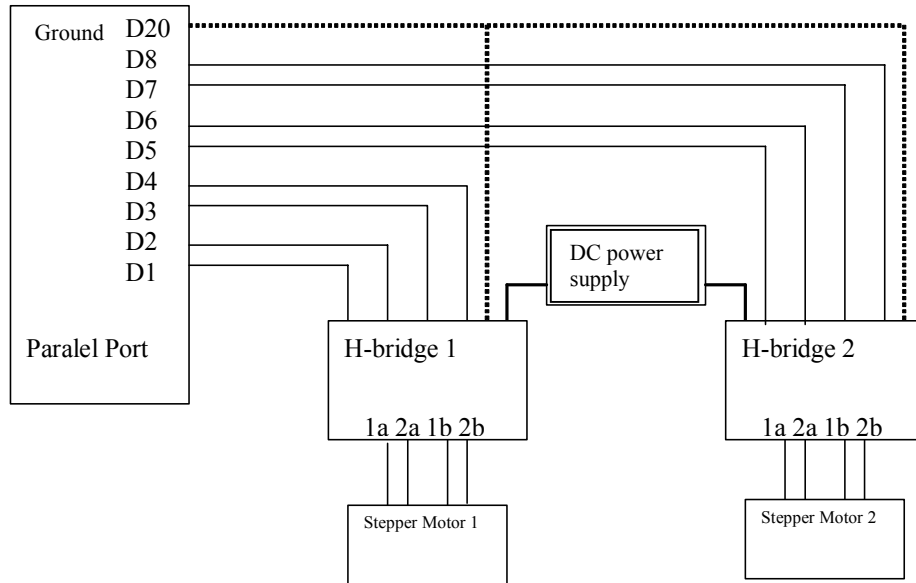
Figure 3.6 Working scheme of LN298 H-bridge integrated circuit.

3.5 Construction of MOS Structures

Before the fabrication of the MOS structures, the general cleaning of the sample (oxide layer on Si) was carried out. The procedure used for the general cleaning can be summarized as follows:

1. The sample is boiled in trichlorethylen for 5 minutes.

2. Then, it is inserted into the container tube which has de-ionized water of 18 Ω *cm* resistivity in. This container is placed into the vibrator system (BRANSONIC 221 vibrator) to vibrate the sample for 5 minutes.

3. The sample is put into another container which has acetone (MERCK brand) and then the system is vibrated for 15 minutes.

4. If the oxide is SiO_2 on Si substrate, this process is continued. However, if the oxide is metal based oxide, this step is skipped and continued with step 5.

   i.   550 ml H_2O, 120 ml H_2O_2 and 80 ml HCl are mixed into another plastic based container.

   ii. This mixture is boiled using hot plate.

   iii. As soon as the boiling of the mixture starts, the sample is put in this boiling mixture and boiled for 15 minutes.

5. The sample is put into another container which has de-ionized water, and then it is rinsed.

6. The sample is dried by N_2 gas.

7. 10% HF and 90% de-ionized water are mixed in another plastic based container and used for the back-contact (Si) cleaning from SiO_2.

8. Metal contact onto the back (Si) surface is evaporated using the evaporation system at the pressure below 10^{-6} Torr.

9. In order to decrease the series resistance, the sample is annealed around 400^0C in the oven, (This is done if the sample is SiO_2 on Si).

10. The sample is placed on the reverse side into the evaporation system for the purpose of evaporating metal gate onto the oxide layer.

3.6 Measurement Systems

3.6.1 MOS Capacitance Measurements

The combination of two types of voltages is used in measurement instruments. They are a linear voltage ramp and a small sinusoidal AC voltage. The linear

voltage ramp is used to sweep the voltage over the bias ramp range from accumulation to inversion or from inversion to accumulation. The ramp rate is given in mV/s. The small sinusoidal AC voltage whose peak-to-peak voltage is generally less than 50 mV is superimposed on the ramp voltage. As a result of this voltage combination, the measurement of differential capacitance, $C_{dif} = dQ/dV$, or conductance, $dG = dI/dV$, is possible. The measurement frequency can be varied generally from a few hertz to a few MHz. The schematic for the measurement of C-V and G-V data from the MOS structure is seen in Figure 3.7.
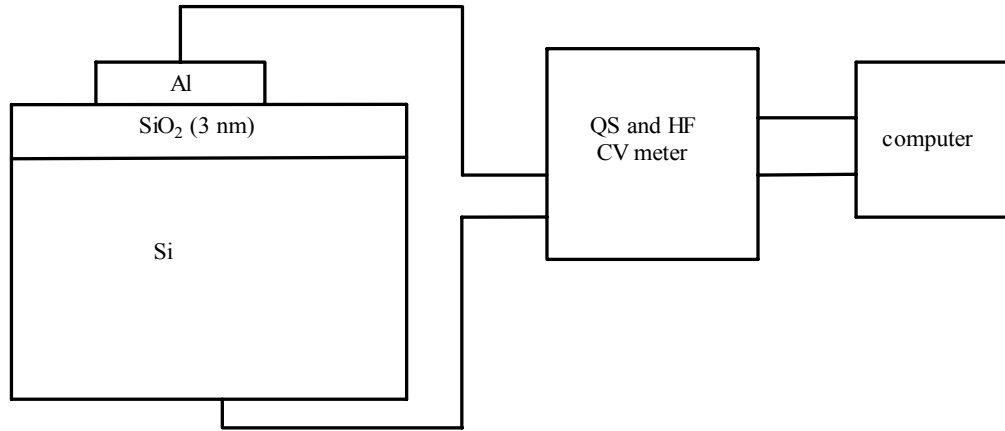
Figure 3.7 MOS capacitor and the C-V measurement system.

In Figure 3.8, the most common three principal C-V characteristics are given. All these three curves occur in inversion region where $V_G > V_T$. The reason for the separation to three curves in the inversion is minority carrier effects. These are named as (i) Low frequency, (ii) high frequency, (iii) ultrahigh frequency limits.

3.6.1.1 Low frequency limit:

At low frequency limit, the frequency is sufficiently low that the minority carriers are in thermal equilibrium with the small signal AC voltage. When the

measurement frequency period $1/f$ is less than the minority carrier generation time, the minority carriers are in equilibrium with the small AC voltage signal.

3.6.1.2 High frequency limit:

At this limit, the minority carriers are in equilibrium with the slowly varying ramp voltage. But minority carriers cannot follow the rapidly varying small-signal AC voltage. In this situation, x_d becomes fixed at $x_{d\,\max}$ and independent of gate bias. As a result of this, C_{dif} remains constant as V_G goes to values beyond V_T.

3.6.1.3 Ultrahigh frequency limit:

This situation is termed deep depletion. In deep depletion, the gate bias ramp rate is too rapid to allow the inversion layer to form by thermal generation. As V_G exceeds V_T, the inversion charge is absent. Therefore, the space charge in the semiconductor $(Q_{sc}=-q\,N_a^-x_d)$ must increase with $x_d > x_{dmax}$. This increase in x_d provides more negative charge due to the ionized acceptors in order to balance the larger positive gate charge. Further increases in gate voltage, V_G, can result in avalanche breakdown.
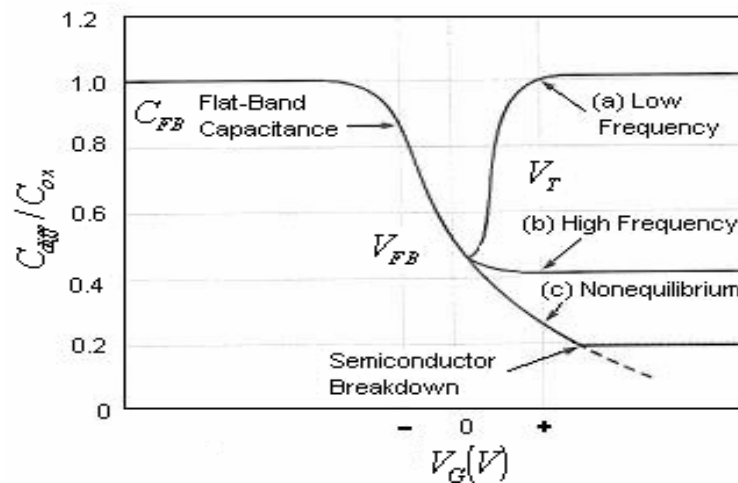
Figure 3.8 The C-V behavior for three different conditions **(a)** low frequency, **(b)** high frequency, **(c)** deep depletion (taken from 30).

The construction of the MOS capacitors was done both in the Physics Department of the Middle East Technical University, Turkey and Institute of Solid State Physics, Bulgarian Academy of Sciences, Bulgaria.

High frequency capacitance voltage and conductance voltage curves were obtained from MOS capacitors by using HP 4192A LF Impedance Analyzer in the Physics Department of the Middle East Technical University, Turkey controlled by a Labview program. Current voltage curves were obtained by HP 4140B pA meter/DC voltage source in the Physics Department of the Middle East Technical University, Turkey. The information related to dielectric and electrical characteristics of the oxides were extracted from these curves.

3.6.2 Spectrophotometric Measurements

Varian Cary 5E (Figure 3.9) optical absorption spectrometer at the Central Laboratory of Photoprocesses, Bulgarian Academy of Sciences, Bulgaria was used for the spectroscopic measurements. It is a standard research tool with a wavelength range from 175 nm to 3300 nm and can be applied to various samples including crystals, liquid solutions, and polymer films. The reflectance and transmittance measurements were done using suitable apparatus for the spectrometer. Since the Si substrate is opaque at the frequencies studied in our experiments, just the reflectance measurements with the aid of *VW absolute specular reflectance apparatus* were conducted, not the transmittance for our samples.

Both the refractive index and film thickness were determined [32] with high accuracy in the spectral range $\lambda = 350\text{–}800$ nm, using reflectance measurements (with an accuracy of 0.5%) at normal light incidence for our samples by Varian Cary 5E spectrophotometer for reflectance, refractive index and optical thickness measurements. Refractive index, n, and film thickness, d, of the layer were obtained by minimization of the objective function using the substrate trust region method based on the interior-reflective Newton method [33]. More details on the calculating procedure used can be found elsewhere [32]. The thickness, dispersion energy and the single-oscillator energy were varied until a good fit between the measured and calculated values of reflectance, R, was found (accuracy better than 0.5%). The fit

was accepted as successful when good enough accordance between ellipsometrically measured and fitted thickness were achieved.

Figure 3.9 Picture of the spectrophotometer measurement system.

Figure 3.10 The VW Specular Reflectance accessory.

3.6.2.1 VW Absolute Specular Reflectance Accessory

The VW Specular Reflectance accessory (Figure 3.10) is designed to measure the 'mirror-like' reflectance off a sample surface. It has applications in measuring the specular reflectance of different types of surfaces. In addition, it can be used to determine the degree of polishing of an optical surface, or to measure the film thickness of thin coatings. It can also be used in a wide variety of other applications. Samples can be placed in both beams, allowing comparative measurements.

3.6.2.2 Small ample measurement

The measurement of samples as small as 12 mm in diameter, and samples with very low reflectance (such as anti-reflection coatings) can be enhanced with the use of the 'single bounce' technique.

A mirror of known reflectivity is placed next to the sample, reflecting the first bounce of the light. The sample then reflects the second bounce. This technique ensures the maximum light throughput. The data is then corrected for the contribution of the mirror.

3.6.3 Ellipsometer

Ellipsometry is a well-established non-destructive optical method for precise determination of properties of surfaces and thin films. Thickness and optical properties of the film can be analyzed by means of the change in polarization state of incidence light after reflection from the film's surface. If linearly polarized light of a known orientation is reflected at oblique incidence from a surface then the reflected light is elliptically polarized. The shape and orientation of the ellipse depend on the angle of incidence, the direction of the polarization of the incident light, and the reflection properties of the surface. The polarization of the reflected light can be measured by a quarter-wave plate followed by an analyzer; the orientations of the quarter-wave plate and the analyzer are varied until no light passes though the analyzer (nullifying condition). From these orientations and the

direction of polarization of the incident light, the relative phase change, Δ, and the relative amplitude change, Ψ, of the electromagnetic wave can be calculated. These values are related to the ratio of Fresnel reflection coefficients, *Rp* and *Rs* for p- and s- polarized light, respectively. The main ellipsometer equation, i.e. amplitude ratio, *ρ*, is given in the following form;

$$\rho = \tan(\Psi)\, e^{i\Delta} = \frac{R_p}{R_s} \tag{3.1}$$

Since *ρ* is a complex number, it contains "phase" information, which makes the measurement very sensitive.

Figure 3.11 The picture of the Rudolph Auto EL II ellipsometer.

The most important application of ellipsometer is to study thin films. In the context of ellipsometry a thin film is one that ranges from essentially zero thickness to several thousand Angstroms, although this range can be extended in some cases. If

a film is thin enough that it shows an interference color then it will probably be a good ellipsometric sample. The sensitivity of an ellipsometer is such that a change if film thickness of a few Angstroms is usually easy to detect.

Rudolph Auto EL II working at 632.8 nm wavelength ellipsometer at the optoelectronics laboratory of the Physics Department in the Middle East Technical University was used for the measurements of the refractive index and the thickness of the thin films during the course of this work. The picture of the ellipsometer is given in Figure 3.11.

3.6.4 X-ray Photoelectron Spectroscopy (XPS)

In XPS, the sample is illuminated with soft (1.5keV) X-ray radiation in an ultrahigh vacuum. The photoelectric effect leads to the production of photoelectrons, the energy spectrum of which can be determined in a beta-ray spectrometer. In this process, the photon is absorbed by an atom in a molecule or solid, leading to ionization and the emission of a core (inner shell) electron, whose binding energy is defined by the following equation;

$$hv\text{-}KE = BE \tag{3.2}$$

where *KE* is the electron kinetic energy and *hv* is the photon energy.

For XPS, *Al K_α* (1486.6eV) or *Mg K_α* (1253.6eV) is often the photon energies in common use. Other X-ray lines can also be chosen such as *Ti K_α* (2040eV). The XPS technique is highly surface specific due to the short range of the photoelectrons that are excited from the solid and strongly attenuated by passage through the sample material itself. Therefore, the information obtained comes from the sample surface, with a sampling depth on the order of 5 nm.

For each and every element, there will be a characteristic binding energy associated with each core atomic orbital i.e. each element will give rise to a characteristic set of peaks in the photoelectron spectrum at kinetic energies determined by the photon energy and the respective binding energies.

The presence of peaks at particular energies therefore indicates the presence of a specific element in the sample under study - furthermore, the intensity of the peaks is related to the concentration of the element within the sampled region. Thus, the technique provides a *quantitative analysis of the surface composition* and is sometimes known by the alternative acronym, ESCA (**E**lectron **S**pectroscopy for **C**hemical **A**nalysis).

3.6.4.1 Instrumentation

The detection of photoelectrons requires that the sample be placed in a high vacuum chamber. Since the photoelectron energy depends on X-ray energy, the excitation source must be monochromatic. The energy of the photoelectrons is analyzed by an electrostatic analyzer and the photoelectrons are detected by an electron multiplier tube or a multichannel detector such as a microchannel plate. The schematic view for the XPS measurement system is given in Figure 3.12.
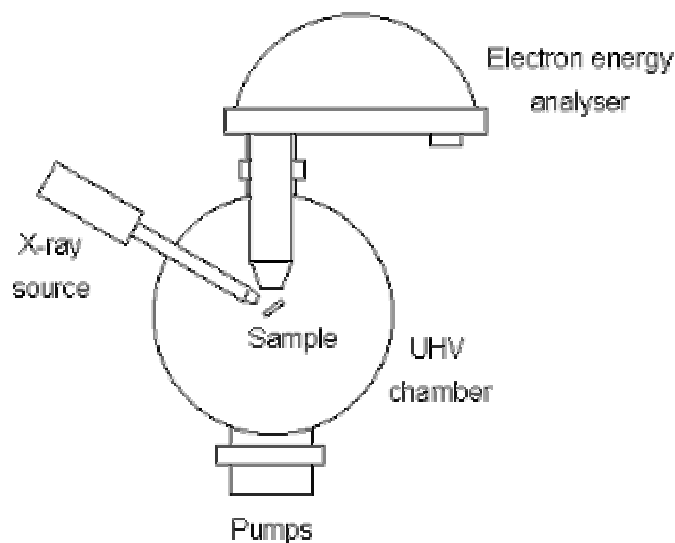
Figure 3.12 Schematic view of the XPS measurement system.

During the course of this study, the X-Ray Photoelectron Spectroscopy (XPS) data were obtained in an ESCALABII high vacuum apparatus (VG Scientific Ltd.) at the

Institute of General and Inorganic Chemistry, Bulgarian Academy of Sciences, Bulgaria with a residual gas pressure better than 1×10^{-8} Pa. AlK_α (1486.6 eV) radiation was used to excite the photoelectrons from the sample. All spectra were taken at 300 K. The photoelectrons were separated by a semi-spherical analyzer with a pass energy of 10 eV. The instrumental resolution measured as the full width at half maximum (FWHM) of the Ag $3d_{5/2}$ photoelectron peak was 1.0 eV. The photoelectron lines of Si 2p and O 1s were recorded. The energy position of the peaks was determined with an accuracy of 0.1 eV. The spectra were obtained under an angle of observation of the photoemitted electrons $\theta = 90^o$, (with respect to the surface plane).

3.6.5 Fourier Transform Infrared Spectroscopy (FTIR)

In a molecule, the atoms are not held rigidly apart. Molecular bonds vibrate at various frequencies depending on the elements and the type of bonds at certain conditions. If infrared radiation of a specific frequency (between 300 and $4000cm^{-1}$) is subjected to a bond, it will absorb infrared energy at certain frequencies (or wavelengths). As a result, the bond will move from the lowest vibrational state to the higher ones. For any given bond, there are several specific frequencies at which it can vibrate. According to quantum mechanics, these frequencies correspond to the ground state (lowest frequency) and several excited states (higher frequencies). The basic structure of compounds can be determined by the spectral locations of their IR absorptions.

There is, however, one important restriction that the molecule will only absorb radiation if the vibration is accompanied by a change in the dipole moment of the molecule. A dipole occurs when there is a difference of charge across a bond. If the two appositely charged molecules get closer or further apart as the bond bends or stretches, the moment will change.

BRUKER Equinox 55 type Fourier Transform Infrared (FTIR) spectroscopy at the Optoelectronics Laboratory of the Physics Department in the Middle East Technical

University, Turkey was used to determine the chemical composition and structure of the films as a function of various oxidation parameters during this study.

3.6.6 X-ray Difraction (XRD)

X-rays are electromagnetic radiation with typical photon energies in the range of 100 eV – 100 keV. Standard optical microscope measurements do not provide enough information on the crystal structure, since the interatomic distances are usually of the order of a few angstroms. For diffraction applications, x-rays in the range of a few angstroms to 0.1 angstrom (1 keV – 120 keV) are used. Because the wavelength of x-rays is comparable to the size of atoms, they are ideally suited for probing the structural arrangement of atoms and molecules in a wide range of materials. The energetic x-rays can penetrate deep into the materials and provide information about the bulk structure.

X-rays primarily interact with electrons in atoms. When x-ray photons collide with electrons, some photons from the incident beam will be deflected away from their original direction. Diffracted waves from different atoms can interfere with each other and the resultant intensity distribution is strongly modulated by this interaction. If the atoms are arranged in a periodic fashion, as in crystals, the diffracted waves will consist of sharp interference maxima (peaks) with the same symmetry as in the distribution of atoms. Measuring the diffraction pattern, therefore, allows us to deduce the distribution of atoms in a material. The maxima conditions for a beam diffracted by atomic planes are given by the following expression which is known as the Bragg equation;

$$n\lambda = 2d \sin\theta \tag{3.3}$$

where n represents the order of reflection and is an integer. The other physical parameters are defined as follows: λ is the wavelength of the incoming X-rays, d is the interplanar spacing between successive atomic planes and θ is the angle of incidence which is also equal to the angle of reflection.

Common targets used in x-ray tubes include Cu and Mo, which emit 8 keV and 14 keV X-rays with corresponding wavelengths of 1.54 Å and 0.8 Å, respectively.

The crystallinity of the films was examined by taking XRD patterns. The XRD analysis were carried out by using a Rigaku Miniflex system equipped with CuK_α radiation of average wavelength 1.54059 Å with 2°/min. scan speed at the Optoelectronics Laboratory of the Physics Department in the Middle East Technical University, Turkey. The XRD patterns were analyzed with a computer software and ICDD database which includes the diffraction patterns of well known structures. The peak matching process was carried out based on the observed peak positions at specific 2θ values and relative intensities of the peaks.

3.7 Series resistance correction for MOS devices

3.7.1 What is series resistance?

Series resistance is an important parameter of small signal energy loss in the MOS capacitor measurements. There are five different sources for the series resistance;

1. Contact to the gate,
2. Back contact to the silicon,
3. Dirt film or particulate matter between the back contact and the silicon,
4. Resistance of the quasi-neutral bulk silicon between the back contact to the silicon and the depletion layer edge at the silicon surface underneath the gate,
5. Extremely non-uniform doping distribution in the silicon.

It can be minimized by
  ✓ Sample fabrication,
  ✓ Measurements at low frequencies where this effect is negligible,
  ✓ Measurement of series resistance and applying a correction to the measured admittance.

3.7.2 Minimization and Correction to the measured admittance for series resistance

It is not easy to make negligibly small series resistance in every case, the general approach is to measure and apply the series resistance as a correction to the measured admittance. Series resistance depends on the applied voltage and frequency. The effect of series resistance is high at high frequency measurements and greatest in strong accumulation. Since the series resistance depends on the applied voltage and frequency, its value can be found and extracted from the measured data as shown in details in the following form. Figure 3.13 shows the equivalent circuit of the MOS capacitor for strong accumulation.

$<Y_{it}>$ is the average interface trap admittance. In strong accumulation condition, the equivalent circuit is simplified to Figure 3.13 (b) since $wC_A >> <Y_{it}>$, so $<Y_{it}>$ is shunted. In this situation, since $C_A >> C_{ox}$, the equivalent circuit is transformed to Figure 3.13 (c) circuit of the MOS capacitor for strong accumulation.

To determine R_s, MOS capacitor is biased into strong accumulation. Admittance Y_{ma} across A-A in Figure 3.13 (c) in strong accumulation in terms of the capacitance C_{ma} and parallel conductance G_{ma} is given in the following formula,

$$Y_{ma} = G_{ma} + jwC_{ma} \qquad (3.4)$$

Impedance is

$$Z_{ma} = \frac{1}{Y_{ma}} \qquad (3.5)$$

Series resistance is the real part of the impedance;

$$R_s = \mathrm{Re}\,al(Z_{ma})$$
$$R_s = \frac{G_{ma}}{G_{ma}^2 + w^2 C_{ma}^2} \qquad (3.6)$$

Examining Figure 3.13 (c), C_{ma} is obtained as

$$C_{ma} = \frac{C_{ox}}{1 + w^2 R_s^2 C_{ox}^2} \qquad (3.7)$$

Substituting R_s into C_{ma} equation results in,

$$C_{ox} = C_{ma}\left[1 + \left(\frac{Gma}{wC_{ma}}\right)^2\right] \qquad (3.8)$$

Corrected capacitance and corrected equivalent parallel conductance G_c at the frequency of interest are

$$C_c = \frac{\left(G_m^2 + w^2 C_m^2\right)C_m}{a^2 + w^2 C_m^2} \qquad (3.9)$$

and

$$G_c = \frac{\left(G_m^2 + w^2 C_m^2\right)a}{a^2 + w^2 C_m^2} \qquad (3.10)$$

where $a = G_m - \left(G_m^2 + w^2 C_m^2\right)R_s$ and C_m and G_m are the capacitance and the equivalent parallel conductance measured across the terminals of the MOS capacitor.
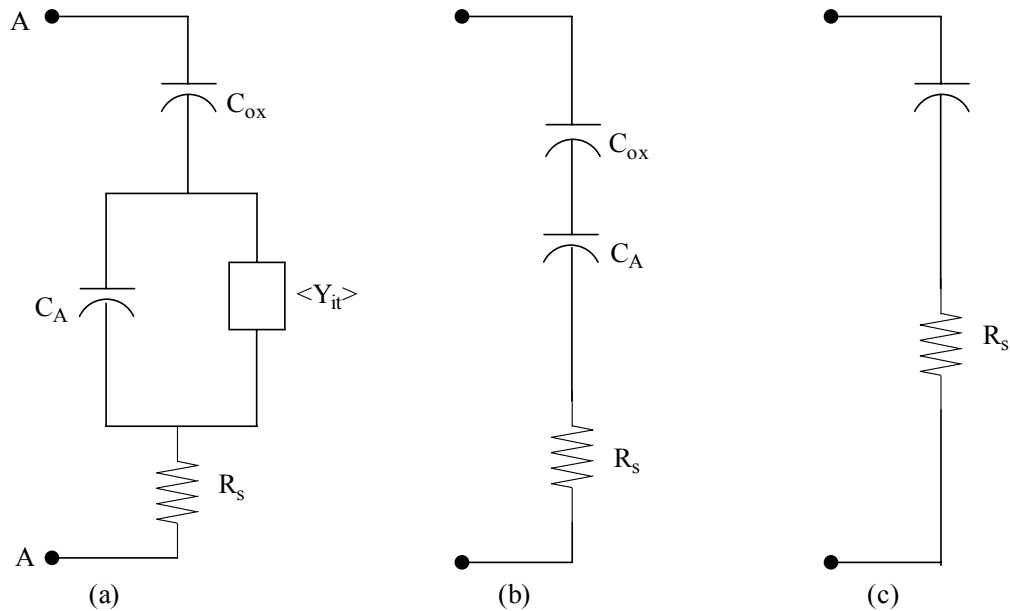
Figure 3.13 Equivalent circuit of the MOS capacitor in strong accumulation.

3.7.3 Computerized calculation program for Series Resistance

A program that calculates the series resistance of a specific MOS device was written in the labview programming language. HP 4192A Impedance Analyzer was used for the capacitance voltage measurements of the MOS capacitors. While measuring the capacitance-voltage (C-V) values, a serial port was used to transport the measured values to a file in the computer. These files contain three columns data as capacitance, conductance and sweeping voltage values. The capacitance and conductance values at strong accumulation and the measurement frequency of the specific measurement need to be given as the input parameters of this program. When this program is run, the file which needs to be corrected is asked by a dialog and then the name of the corrected file is asked. At the same time, in front panel of this labview program, two graphs are drawn. First one is the Capacitance – Voltage, the second one is the Conductance – Voltage for again both corrected and uncorrected data drawn together in each of the graph. The labview program developed for this purpose is given in Appendix A.

CHAPTER 4

OXIDATION OF Si SURFACE BY A PULSED Nd:YAG LASER

4.1 Introduction

One of the most important issues in modern microelectronics is to fabricate dielectric layers with enhanced capacitance properties to meet the requirements of the high density dynamic random access memories. There are mainly two directions in the research activities concerning the production of these films: i) fabrication of ultra-thin and electrically reliable SiO_2 layers on Si substrate [2], and ii) fabrication of alternative dielectrics with high dielectric constant, (high-κ materials) [34-36]. In both cases, however, there is always great interest in novel processing techniques that may, in some way, improve the existing methods of production. Formation of an oxide layer on Si substrate can be realized by a number of well-known techniques, such as thermal oxidation, a variety of chemical vapor deposition methods, sputtering, plasma assisted oxidation, oxidation by pulsed or continuous light sources [2]. Among all of these techniques, laser assisted oxidation has attracted special attention due to its ability to induce localized oxidation with good spatial resolution and ability to achieve a good control over the thickness of very thin layer of 1-2 nm at low processing temperatures [7]. Various laser sources (Ar^+ [5], CO_2 [6], ruby [7], excimer [8]) with continuous or pulsed beams have been used to process Si or metal surfaces for the oxidation, and successful growth of thin oxide layers has been demonstrated. Pulsed Nd-YAG laser operating at 1064 nm has recently been applied to an oxidation of metal surfaces for obtaining high-κ dielectrics [14]. The emitted laser energy is 1.165 eV at 1064 nm, which is slightly over the bandgap energy of Si

crystal, the absorption by the Si surface is then expected to be weak due to limiting value of the photon energy. On the other hand, high peak energy pulses of Nd-YAG laser beam usually result in melting of the surface. The effect of laser pulses on the Si surface morphology and the mechanisms of the melting were reported [15,16]. So far, observation of high quality SiO_2 on Si grown by Nd-YAG laser has not been reported. The question here is, whether or not an efficient oxidation can be achieved without causing an undesirable deformation of the surface. If the answer is yes, then the feasibility of SiO_2 formation and device characteristics with this kind of oxide layer needs to be investigated.

In this chapter, we give the results on the formation of thin SiO_2 layer on Si surface by pulsed Nd-YAG laser scanned over a predefined region, and demonstrate the successful oxidation of Si surface with a laser power, which is slightly smaller than needed for surface melting. A special attention is given on the influence of both laser power and the substrate temperature on the oxidation process and thickness uniformity of the layers obtained. The electrical properties of the films in Metal – Oxide – Si (MOS) capacitor configuration were also examined.

It is well known that the optical properties of every dielectric film are important when discussing its applied aspects as an active dielectric. Here, in this chapter, we also report on some optical properties of Nd:YAG laser-oxidized SiO_2 thin films with thickness values changing between 15 to 75 nm. Refractive index, n, and the thickness, d, of the layers are determined with high accuracy in the spectral range of λ = 300 – 800 nm using reflectance measurements at normal light incidence [32]. The dependences of the optical parameters on the oxide thickness, substrate temperature during oxidation and laser – beam – energy density are also discussed.

4.2 Experimental procedure

The samples were cleaned and loaded into the vacuum chamber (step 2 of section 3.2). After the conditions were satisfied for oxidation, the laser action was started. The laser treatment was carried out using a Nd:YAG radiation at 1064 nm, (EKSPLA Pulsed Laser NL301). The laser parameters are summarized in Table 4.1. The oxide

thickness, d, and the refractive index, n, of the oxide layers obtained were determined by an ellipsometer, (λ=632.8 nm). The electrical characterization of the layers was carried out using MOS capacitors with evaporated Al gate electrodes with an area of 1.96 x 10^{-3} cm^2. The dielectric and electrical characteristics of the layers were studied using Capacitance – Voltage (C-V), Conductance – Voltage (G-V), and Current – Voltage (I-V) measurements. The oxide charge, Q_f, was evaluated from the flat band voltage, V_{fb}, of the high-frequency (1 MHz) C-V curves.

Table 4.1 Laser Parameters

Wavelength	Pulse duration	Pulse frequency	Total pulse energy	Near field intensity profile	Beam radius
1064 nm	4.7 ns	10 Hz	320 mJ	hat top	3 mm

The specular reflectance, R, of the samples was measured at normal light incidence in the spectral range λ = 300 – 800 nm by a Varian Cary 5E spectrophotometer (see section 3.6.2 for details) with an accuracy of 0.5 %. Refractive index, n, and the physical thickness, d, of the layers were determined by minimization of the objective function, F, using subspace trust region method based on the interior-reflective Newton method [33]. F has the form of the sum of the squared discrepancies between the measured and calculated values of reflectance:

$$F(n,d) = \sum_{i=1}^{N} \left[R_i^{meas} - R_i^{calc} \right]^2 \tag{4.1}$$

The summation is performed over the available N experimental points where λ_i is in the 300 – 800 nm range. The dispersion of the refractive index was described by the Wemple-Di Domenico single–oscillator model [37], as a function of the

dispersion energy and the single-oscillator energy. Their initial estimates were taken from the literature [37]. The thickness, dispersion energy and the single-oscillator energy were varied until a good fit between the measured and calculated values of R was found, (accuracy better than 0.5 %). The fit is accepted as successful when good enough accordance between ellipsometrically measured and fitted thickness values are achieved.

4.3 Results and Discussions

4.3.1 Thickness uniformity

4.3.1.1 Effect of laser beam energy density

Ellipsometric measurements of the variation of the oxide thickness over the exposed area for various laser beam energy densities (for simplicity we will also use the laser power term) are shown in Figure 4.1 a, (substrate temperature, T_s, was kept constant at 748 K). The highest value of oxide thickness, d, is obtained at the center of the laser beam. It is seen that an oxide layer within a predefined region of the surface can be formed with an acceptable uniformity having a Gaussian shape for thickness measurements and a relatively large region around the active spot is also oxidized (two tails of Gauss curves) but with significantly reduced oxide thicknesses. The variation in the oxide thickness is caused by the nonuniformity in the laser beam intensity, which is related to the internal design of the laser system. For certain laser power values, the measured thicknesses over the periphery regions are fairly similar and the effect is more pronounced for lower powers. Here and further, we will focus only on the region close to the center of laser beam, (noted as "0" in Figure 4.1 a), and its profile evaluation with the laser power, P. For the laser beam energy fluence below than about 3.00 J/cm^2, oxidation process was not detected at all. At these lower power values, the oxide detected was virtually native oxide on the wafer and it was slightly affected also from the substrate temperature. Active oxidation started to be seen for $P \geq 3.00$ J/cm^2. The laser beam energy density level significantly affects the oxide thickness, having lower d for lower laser powers and higher d for higher ones. The oxide thickness at the center of the beam, ranging from 7 to 34 nm, is

proportional to P from 3.06 to the highest value, 3.51 J/cm^2. This means that the higher laser power results in sufficiently thicker films and the growth takes place with a faster rate. However, a nonuniformity of the oxidation around the beam center is obvious. The thickness profile shows that a relatively flat narrow range can be found over the distance of 1 mm from the center across which the thickness variation is within 10 %. This dispersion has the lowest value, however, for the highest T_s and P, i.e. it changes between 3 – 4 % at $T_s = 748$ K while it is around 10 % for the lowest T_s. The area of this active oxidized spot on the wafer is in fact independent of the laser power. It should be noted that a second peak close to the main one appears in the oxidant profile for higher energy densities. As a result, a slightly higher oxide thickness corresponding to the power values is obtained. The right-hand side of Figure 4.1 a illustrates this second peak. Even though there may be few reasons for this second peak, it is most likely caused by the nonuniformity in the laser beam energy intensity profile due to the intra-cavity components of the laser that leads to hat-top shape. To check this effect, the two dimensional intensity profile of the beam was recorded by a high resolution CCD camera. The processing of the image demonstrates that the laser beam is nonuniform and includes two main peaks, one of which is the more intensive than the other (Figure 4.1 b). While this can be an explanation for the nonuniformity of the processed area, the small step scanning of the beam on the wafer homogenizes the exposed area in case of perfect X-Y scanner. Since the converging lens moves relative to the laser beam, the focal point also moves resulting in the intensity variation. We generally obtain an oxidized region having more affected at one corner of the oxidized area, despite that the exact intensity distribution is unknown. This second peak's region on the wafer is not crashed or melted and not recognized by naked eyes, whereas, it is detected from the
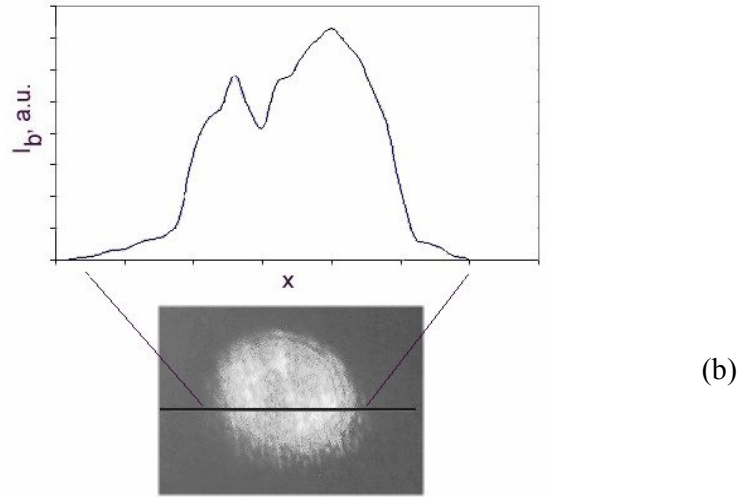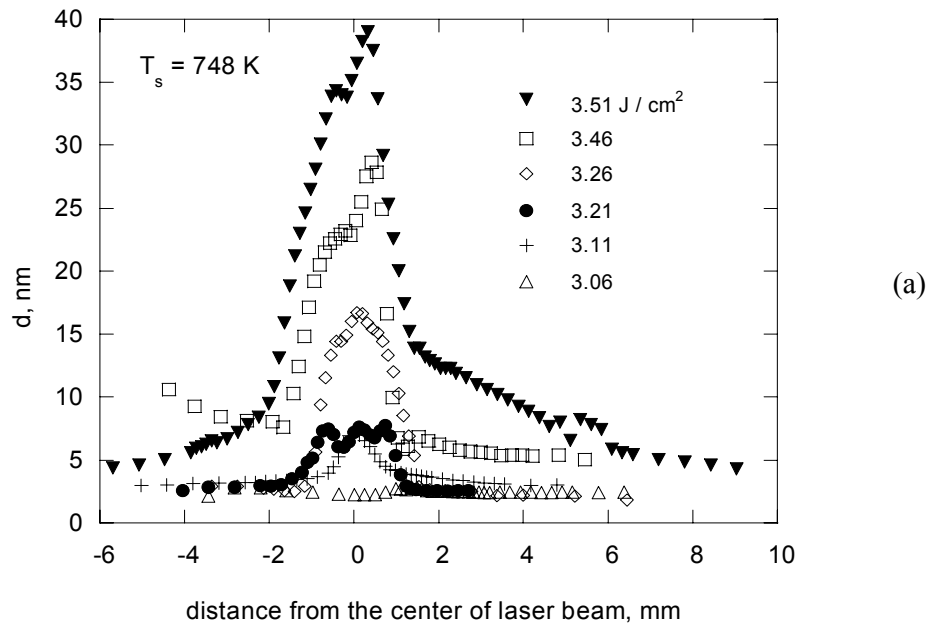
Figure 4.1 (a) Film thickness distribution profile with respect to the center of the laser beam for different beam energy fluences ($T_s = 748K$).
(b) Intensity profile of the laser spot along the scanning direction. Degree of darkness corresponds to the intensity of energy fluence, i.e. the lighter the grey colour is, the more intensive the energy fluence is.

ellipsometer measurements. Therefore, the results imply that this thickness profile feature can be attributed to the nonuniformity of the laser beam intensity on the wafer's surface rather than to the mechanism of laser oxidation itself. Additional evidence for this conclusion comes from the relatively good accordance between the shape of the oxide thickness and laser beam intensity profile, i.e. the oxide thickness distribution repeats the laser beam intensity profile.
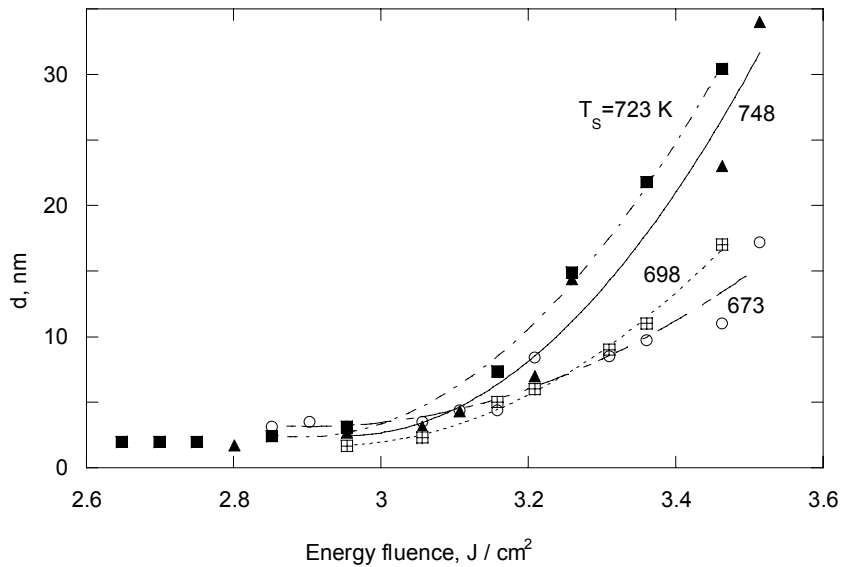
Figure 4.2 Oxide thickness as a function of laser fluence for different T_s.

Figure 4.2 shows the oxide thickness, d, as a function of laser beam energy density for various T_s in the vicinity of the main peak of thickness distribution profile. As seen, the laser beam energy density significantly affects the oxidation process resulting in thicker films for higher power values. The analysis of the data describes the oxide thickness by a linear-parabolic function for all T_s values; $d \propto C_1 P + C_2 P^2$. It is also apparent from the figure that the oxidation process effectively starts when the laser energy fluence exceeds ~3.00 J/cm^2. The energy density "threshold" virtually is independent of substrate temperature, suggesting that the overall oxidation is controlled by the laser fluence rather than T_s as expected. It should be emphasized

that the laser oxidation in our case begins in fact from an initial oxide with a thickness of ~2-3 nm formed on the surface of heated wafer under the action of active oxidizing ambient during the time elapsed between O_2 gas introduction and laser treatment. The oxide thickness measured for $P \leq 3.00$ J/cm^2 (Figure 4.2) corresponds to the thickness of this native oxide, which is slightly influenced by T_s. For P above 3.00 J/cm^2, the oxide grows relatively fast. At the other extreme point, where the laser energy density exceeds 3.60 J/cm^2, the catastrophic deformation of the surface due to the melting is observed. In consequence, the active and safely oxidation interval for laser power is detected namely between 3.00 and 3.60 J/cm^2, where the oxidation takes place without causing any structural deformation of the surface. The results indicate that it is possible to modulate the oxide thickness in an appropriate controlled manner by varying the energy beam density during the growth process. We observed stable film formation for all substrate temperatures by increasing laser beam energy density. As a result of the both effects, i.e. higher P and higher T_s, thicker films are produced. It is clear that when the substrate temperature is increased the thicker oxides are grown at a constant laser beam energy density, i.e. at certain P the oxides are thicker at higher T_s. Even though this qualitative conclusion can be drawn on the effect of temperature dependence, a quantitative analysis is hardly possible due to the unknown chemical-physical processes taking place during the oxidation and also the scattered nature of the data points.

4.3.1.2 Effect of substrate temperature

The oxidation of Si surface by laser beam occurs via heating of the surface locally by the laser beam. The effect of heating is two-fold: increasing the reaction rate of Si atoms with O atoms, and increasing the number of free carriers in the surface region, which in turn enhances the free carrier absorption. The oxidation rate is then expected to depend strongly on the substrate temperature. The energy of the laser beam is about 1.17 eV, which is slightly above the bandgap energy (1.12 eV) of Si at room temperature. Absorption via band-to-band excitation is not expected to provide excess energy for substrate heating. We, then, assume that the heating effect of the laser beam should results from the free carrier absorption which is strongly dependent on the substrate temperature.
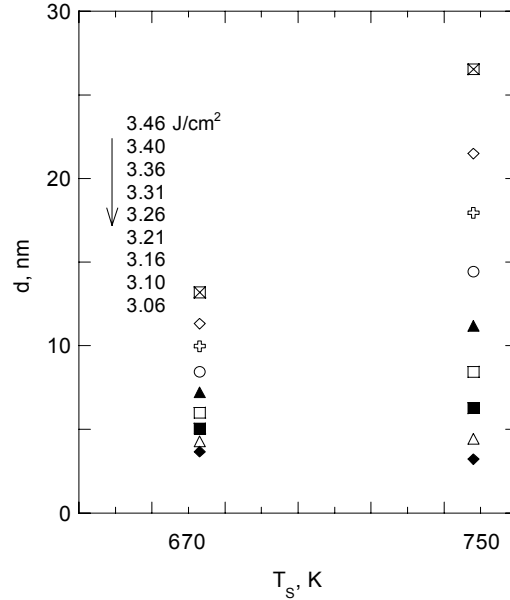
Figure 4.3 Oxide thickness as a function of T_s for various laser beam energy fluences.

The impact of T_s on d for two representative lower and higher substrate temperatures, namely 673 and 748 K is shown in Figure 4.3. As seen, d increases with the enhancement of T_s but the degree of increase depends significantly on the laser energy density. On the other hand, no thickness variation with T_s is detected up to energy density "threshold" for real oxidation, (P~3.00 J/cm^2). Furthermore, d gradually increases with T_s for P above the threshold value, i.e. the higher the energy density the higher the factor of T_s-induced increase is. The changes of substrate temperature from 673 to 748 K results in an increase of d with ~ 80 % when $P = 3.06$ J/cm^2, and the increase of d is by a factor of more than 2 for the highest value of laser energy density used, (3.46 J/cm^2). It emerges that the higher the laser power, the stronger the effect of T_s is. Obviously, heating of the substrate stimulates reactions on the surface, however, the process of the oxidation is mainly controlled by laser action. The effect of substrate temperature has a second order effect in the range of T_s used here. It can be concluded considering the needs of modern microelectronics that the lower laser beam energy density around the threshold value independent of substrate

temperature gives the best laser oxidized films in terms of low enough thickness and high enough thickness uniformity. This is illustrated, for example, in Figure 4.1 a for $T_s = 748$ K.

At the end of this section, it should be emphasized that the physics of laser-assisted oxidation is still speculative. Especially, the results presented here cannot answer the question: "What is the mechanism of laser oxidation itself?". Much more information is needed concerning both the active oxidizing particles created in the oxygen atmosphere under the action of laser beam and wafer surface reactions in order to understand the exact process of oxide growth. Note that the photons' energy used here can not crack the oxygen molecule into two extremely reactive oxygen atoms because the bond energy of O_2 is known to be close to 5.1 eV. Therefore, the laser beam may further either react instantly with the surface of the wafer or alternatively with other O_2 to form a number of powerful oxidants. We are inclined to assume that the active oxidizing particles in our case are oxygen molecules. Most likely, the laser beam induced charged species also contribute to the process of oxidation. For example, it is important to establish the eventual presence of negatively charged species of oxygen, which is known to play a key role in the oxidation of Si. Considering the presence of native oxide on the Si wafer before laser action, i.e. Si – O bonds are already formed even so non-perfect, we assume that the oxide grows by diffusion of oxygen molecules to the interface with Si (Si/oxide) where chemical reactions takes place.

4.3.2 Dielectric and electrical properties

In this section, MOS capacitors fabricated on some of the oxidized regions were studied to evaluate the electrical quality of the grown oxide. Especially, we give representative results on some oxide and interface parameters of a film obtained at one of the laser treatment regimes used. The layer grown at 673 K and 3.31 J/cm^2 is selected for a detailed study. To avoid the errors caused by the thickness nonuniformity, an area near the center of the oxidized region is chosen. For simplicity, we will refer to film obtained as SiO_2 in the following discussions.
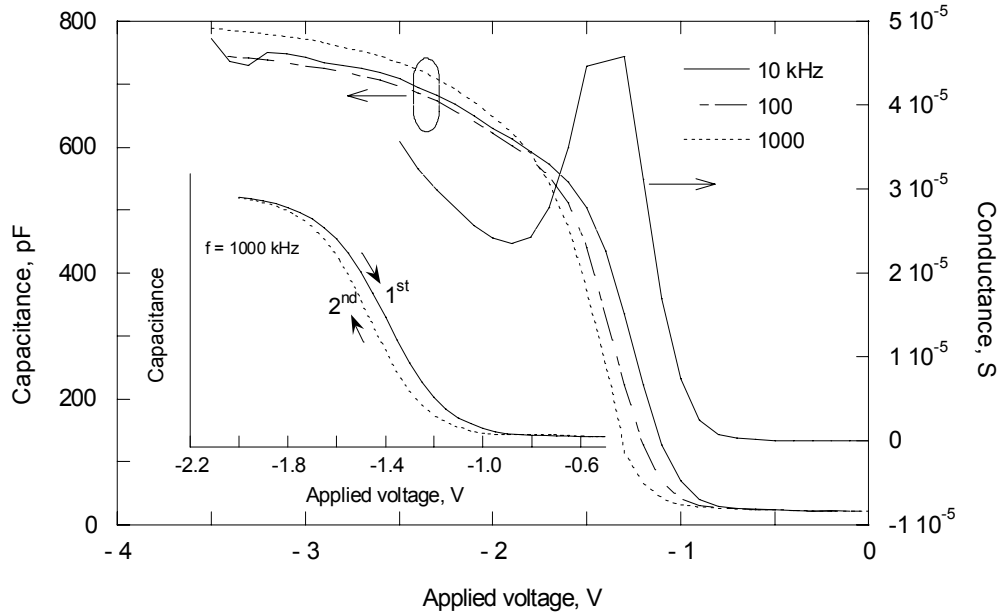
Figure 4.4 C-V curves measured at different frequencies (10, 100, 1000 kHz) and G-V curve at 100 kHz. The inset shows the hysteresis effect for the capacitance with respect to applied voltages.

Figure 4.4 shows typical high-frequency Capacitance – Voltage (C-V) and Conductance – Voltage (G-V) curves (10 kHz; 100 kHz; 1 MHz) for the MOS capacitor fabricated with 1.96 x 10^{-3} cm^2 device area on an 8 nm thick SiO_2 laser-assisted oxidized film. It can be clearly seen that typical MOS characteristics with accumulation, depletion and inversion are clearly obtained in the C-V curve. However, deviations from the saturation value of the C-V curve were observed for high voltage values in both inversion and accumulation sides of the C-V curve, indicating a leaky character for the grown oxide. The important feature of the G-V curve is the observation of the typical conductance peak at around flat band voltage, after which the depletion region capacitance begins to be significant. The observation of conductance peak is an indication of the device performance, which usually does not appear in devices with gross deviations from the ideal structure. The flatband voltage is the voltage corresponding to the flatband capacitance of the device, and roughly equal to the voltage value where the conductance peak is observed.

The flat band voltage, V_{fb}, derived from 1 MHz C-V curve is negative having the value of –1.3 V, (work function difference between Al gate and Si is –0.7 eV). This indicates that the oxide charges present are positive and obtained as 1.5 x 10^{12} cm^{-2}. This value of Q_f is two orders of magnitude higher than that usually obtained in high quality thermal SiO$_2$. Generally, structural non-perfections, bond defects and poor oxidation process conditions result in the higher values of Q_f. As it was detected by XPS analysis, suboxides present indeed in the films (see chapter 5). These intermediate oxidation states of Si, as well as various microstructural defects manifest as electrical active centers in the form of oxide charges. Further studies are needed, however, to clarify the nature of oxide charges in laser-assisted grown SiO$_2$ layer.

The dielectric constant, ε, of the film was estimated to be 3.64 by using the capacitance value in the accumulation mode at 1 MHz, C_0 (–3.5 V) and the known oxide thickness. The index of refraction, n, according to ellipsometrical measurements is 1.35. The lower ε and n values than those values of thermal SiO$_2$ can be attributed to the detected suboxides in the film, i.e. to poor oxygen stoichiometry.

The film exhibits C-V hysteresis (inset of Figure 4.4) on the lower voltage side of the curves, when the gate voltage is swept from accumulation to inversion and back movement. This hysteresis effect indicates the presence of slow (border) states located very close to the Si / oxide interface and recharge during back bias cycle. The hysteresis of the C-V curves is negative. The flat band voltage is shifted as low as –65 mV obtained from the hysteresis curve and the density of slow states from the value of flatband shift is estimated to be 1.6 x 10^{11} cm^{-2}. This means that some charge traps exist in the interfacial region at Si substrate. It should be noted that slow states usually exist in very thin and ultra thin layers even in high quality thermally grown SiO$_2$. In this sense, the slow states detected here are not peculiarity of the laser-induced oxidation. The origin of slow states is generally related with microstructural defects, most likely non-perfect Si – O bonds. It can also be seen from Figure 4.4 that the slight decrease of accumulation capacitance C_0 from 789 at 1 MHz to about 745 pF at both 10 and 100 kHz. The detected leakage current in the film causes the missing of well pronounced saturation of the curves and the non-ideality feature

observed in the range of accumulation mode. On the other hand, the frequency dispersion of C_0 is weak, indicating low leakage currents. The frequency dispersion in the depletion region of C-V curves is also observed (Figure 4.4). Its value between 10 kHz and 1 MHz near the flat band conditions is ~180 mV. This value implies that the interfacial defect charges corresponding to the given frequency ranges are as small as ~ 4.5 x 10^{11} cm^{-2}, ($C_0 = 4$ x 10^{-7} F/cm^2). For illustration, the G-V dependence at 100 kHz is shown in Figure 4.4 and the conductivity peak related to the interface states is seen from this curve. The presence of this peak indicates again low leakage condition, therefore, a relatively good layer quality for device applications.
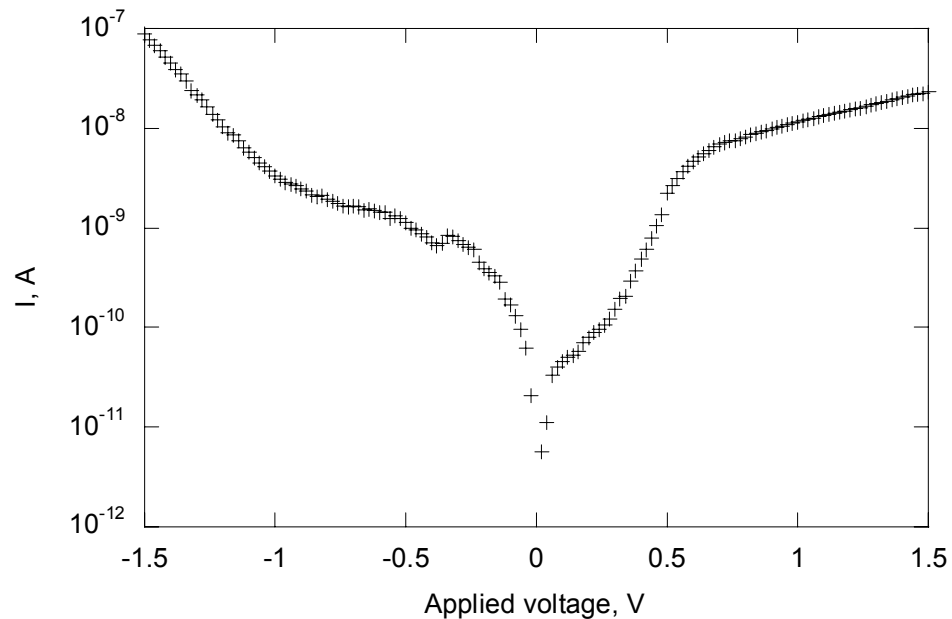
Figure 4.5 I – V curves of MOS capacitor with oxide obtained at $T_s = 673$ K and 3.31 J/cm^{-2}; $d = 8$ nm.

Leakage current as a function of applied voltage is shown in Figure 4.5. The current monotonically increases from 10^{-9} A/cm^2 at very small applied voltages and reaches to 10^{-6} A/cm^2 at ~1.2 MV/cm applied field for forward bias (negative applied voltage where the electrons are injected from Al gate). The shape of the I-V curve for

forward bias gives some indication for appearance of soft breakdowns originated from the defects in the form of oxide charges detected in high density. Well-defined catastrophic (hard) breakdown is not detected up to –1.5 V, (our experimental limit). The gradual increase of the current up to ~10^{-5} A/cm^2 at 1.5 V is also observed at reversed bias (positive applied voltage when the electrons are injected from Si), with changing the slope of the curve (getting smaller) at ~0.6 MV/cm.

4.3.3 Optical Properties: Reflectance spectra and refractive index

Figure 4.6 presents reflectance spectra of laser oxidized films for various laser beam energy densities with a thickness of 50 nm, obtained at the substrate temperature of 748 K. The reflectance spectrum from a Si reference is also shown. As the laser power increases, the reflectance decreases (with 1.5 – 2.5 %) in the ultraviolet region, 300 - 350 nm, indicating a small increase of the optical thickness defined as a product of the refractive index and the layer thickness. As can be seen from this figure, the curves corresponding to 3.16 and 3.36 J/cm^2 are indistinguishable in the spectral range of 350 – 800 nm. Since the thicknesses are the same, 50 nm, the values of optical thicknesses are essentially identical in these cases. This means that these two laser powers are the same in terms of reflectances. However, when the laser power is increased, the reflectance from the samples measurably decreases in the whole spectral range, especially at the higher wavelengths, $\lambda > 400$ nm. Since R is a periodical function of the optical thickness with a periodicity of $\lambda/2$ and when the refractive index of the layer is smaller than that of the substrate, R reduces within an optical thickness range of 0 to $\lambda/4$. In our case, if we suppose that the values of n are close to those of SiO$_2$, the optical thicknesses of the layers are expected to be about $\lambda/20$ for the thinnest film and $\lambda/5$ for the thickest one, and consequently it is smaller than $\lambda/4$. The reflectance decreases over the optical thickness range 6.71 - 3.66 in the spectral range used, because n is lower compared to the refractive index of the Si substrate. The higher values of n are directly related to the decay of R for the layers with $P = 3.41$ J/cm^2 as compared to films obtained at lower laser power, since ellipsometrically measured d is the same for the samples at different laser powers.
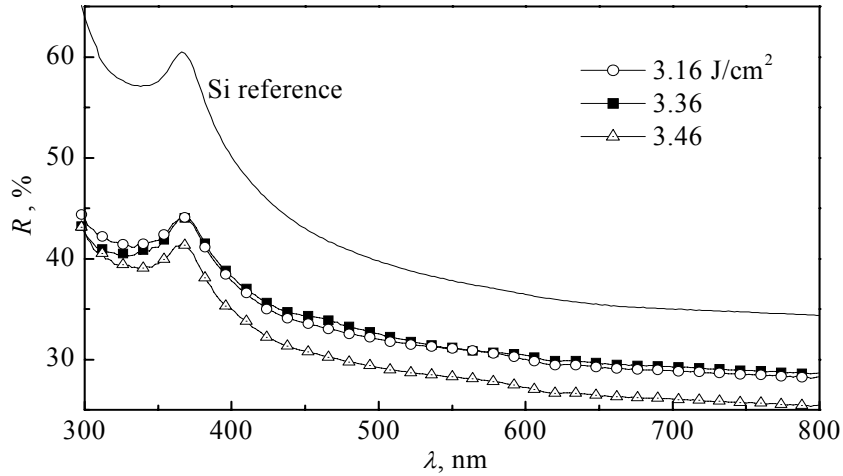
Figure 4.6 Reflectance spectra of laser – oxidized films for various laser beam energy densities; $d = 50$ nm and $T_s = 748$ K.

Reflectance spectra for films oxidized at the lowest and the highest substrate temperatures for two different laser beam energy densities are shown in Figure 4.7. The film thickness is in the range 17 to 50 nm for the corresponding spectra. It is obvious that the reflectance of the thinnest films is not affected at all by T_s. For thin oxides, the spectra are almost the same independent of the value of the laser power. This is seen, here, in the figure for $P = 3.26$ J/cm^2. The results indicate that the substrate temperature in the range of 673 – 748 K has negligible effect on the optical thickness of relatively thin laser-oxidized films, (15 – 20 nm). Even though there are small optical thickness variations, the reflectance is not sensitive to them. This is most likely because the refractive index for thinner films is not sensitive enough to track the changes of T_s from 673 to 748 K. This tendency is also maintained for all laser beam energy densities studied. The absence of T_s effect for thinner films in terms of refractive index means that the densities of the layer formed in this temperature interval are indistinguishable. The effect of T_s on the reflectance is well pronounced for thicker layers (30 – 50 nm), regardless of its changeable behavior over the spectral range, Figure 4.7. A decrease of reflectance

between 300 and 500 nm and the reverse trend at larger wavelengths, ($\lambda > 550$ nm) is observed as a result of T_s increase. This is related to the optical thickness actually, i.e. an increase of the optical thickness in the former case and decrease in the second one. However, it is hard to draw conclusion having in mind only R–spectral behavior because of sophisticated relationship between R and n. The key role of the refractive index in this characteristic of the optical thickness is fairly plausible.
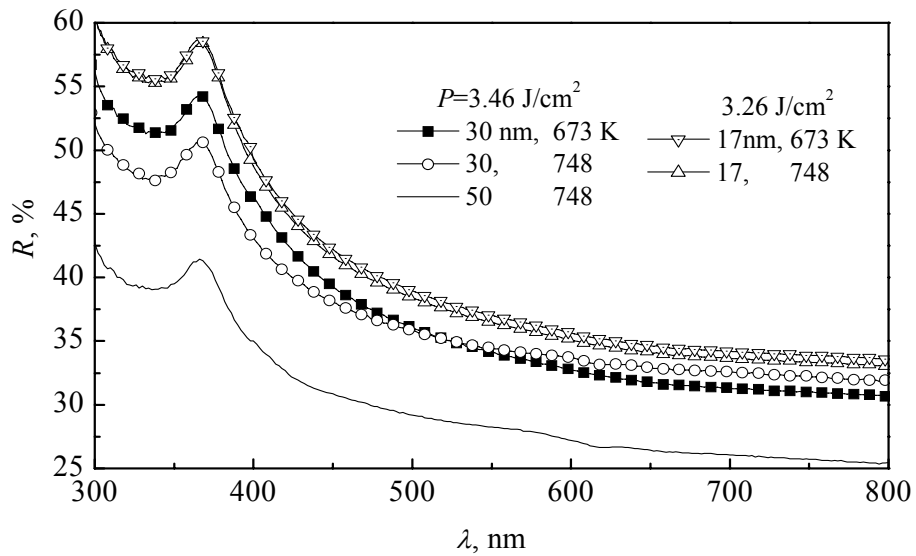
Figure 4.7 Reflectance curves of the films with different thicknesses obtained at two different substrate temperatures and laser beam energy densities.

Notice the wide variation and non-proportional change in reflectance for each thickness. It can also be seen in Figure 4.7 that the decay of R at certain wavelength as compared the spectra of 30 and 50 nm thick films is larger than that of 17 and 30 nm ones. In fact, it is attributed to the well-known $R(nd)$ dependence.

We will, here, concern the dependence of refractive indices of the films on d, T_s and P. The refractive indices of all films were initially determined with an ellipsometer at the wavelength of 632.8 nm. The calculated values of n with respect to λ between

300 and 800 nm for two values of T_s and P and three values of oxide thicknesses are presented in Figure 4.8. It also includes the curve of thermally grown 13 nm thick SiO_2 for comparison. The dispersion curves exhibit a typical wavelength dependence of n for non- or slightly absorbing film. It is in the form of slowly decreasing of n with increasing λ with a tendency of saturation at larger wavelengths. It is also obvious that n is lower for all laser treated samples than that of thermal SiO_2 regardless of its small thickness. This means that, independent of the laser oxidation conditions including the layer thickness, the laser-oxidation provides lower refractive index when compared to thermal oxidation. Since the possible reasons for the lower values of refractive index are the poor density and high porosity of the layers, post-oxidation annealing is being a necessary process for the laser oxidized samples. Furthermore, n for all samples obeys stronger dispersion at shorter wavelengths region, ~300–500 nm, when compared to the thermal SiO_2 dispersion curve. Either the presence of suboxides which lead to the absorption edge to shift to larger wavelengths or the large surface roughness is the reason for this stronger dispersion. The suggestion of suboxides is a simpler explanation and is also consistent with our recent data of X-ray photoelectron spectroscopy analysis [see chapter 5].

It is important to note that T_s and P have strong effect on n. As an example, it is seen from Figure 4.8 that n is increased by 0.1 when T_s is changed from 673 to 748 K for 30 nm thick film obtained at 3.46 J/cm^2. The same behavior is also observed for oxides with thicknesses 50 and 75 nm. The similar behavior of the effect of laser power on n at identical T_s is seen. This effect is clearly realized by comparison of 30 nm thick two samples that n is higher for 3.46 J/cm^2 laser power film by at least 0.1 than that of 3.30 J/cm^2 laser power film, ($T_s = 748$ K). The impact of oxide thickness is the strongest among the three parameters (d, T_s, P) affecting the refractive index. The thickest oxide, 75 nm, has the highest n value regardless of having the lowest substrate temperature. Moreover, n is lower for 50 nm oxide although the film is formed at higher T_s where in both cases P is 3.46 J/cm^2. As the thickness is changed from 50 to 30 nm ($P = 3.46$ J/cm^2 and $T_s = 748$ K), n is reduced by about 0.05. Obviously, the thicker the oxide films are achieved, the

denser as-grown oxides, i.e. higher n, are obtained. By increasing oxide thickness from 30 to 75 nm ($T_s = 673$ K and $P = 3.46$ J/cm^2), the refractive index rises from 1.18 to 1.36 at $\lambda = 633$ nm.
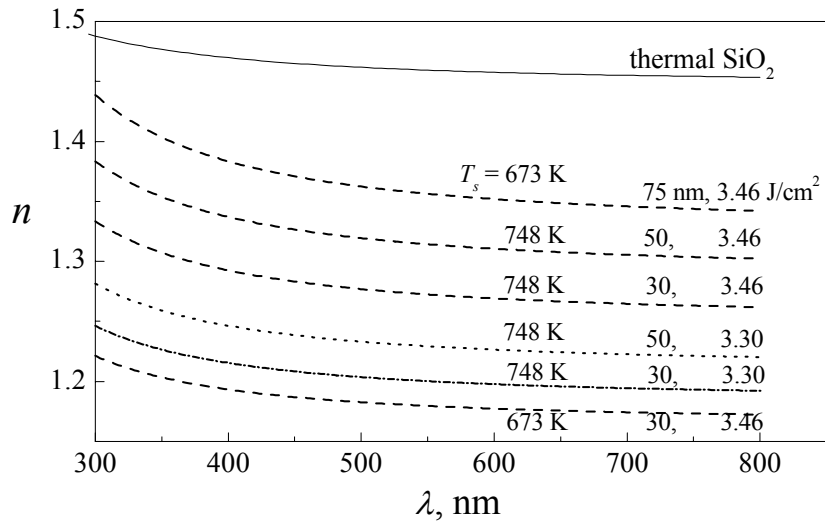
Figure 4.8 Refractive index vs. λ for films obtained at different conditions.

As a result, the thickness dependence of n seems to be attributed to the thicker films are the denser films. Having denser films means a reduction of the interatomic spacing. On the other hand, the refractive index is proportional to the electronic polarizability, which is inversely proportional to the interatomic spacing. In other words, this means that the reduction of interatomic spacing for thicker films results in having greater refractive index. It should be noted that the spectral wavelength has not any influence over the effect of d, T_s and P on the refractive index, i.e. all of the n curves behave in a similar manner over the spectral range $300 - 800$ nm (Figure 4.8). Furthermore, the refractive index values at ~633 nm are in a good agreement with the ellipsometrical measurements for all the cases studied. Moreover, the values extracted from Figure 4.8 imply an approximately linear dependence of n on P. Figure 4.9 shows this behavior for the refractive index at 633 nm wavelength for 50 nm layer grown at $T_s = 748$ K, i.e. refractive index

increases linearly with laser beam energy density. It is possible to evaluate the required laser power for obtaining $n = 1.46$ which is typical refractive index value of stoichiometric SiO_2. If this linear dependence is accepted, the necessary laser power for obtaining $n = 1.46$ falls beyond the critical level of P for surface melting without oxidation. This means that the obtained values of refractive indices are more or less phenomenon of Nd:YAG laser oxidation itself. According to these results, post-oxidation annealing is needed to improve the refractive index values of the layers.
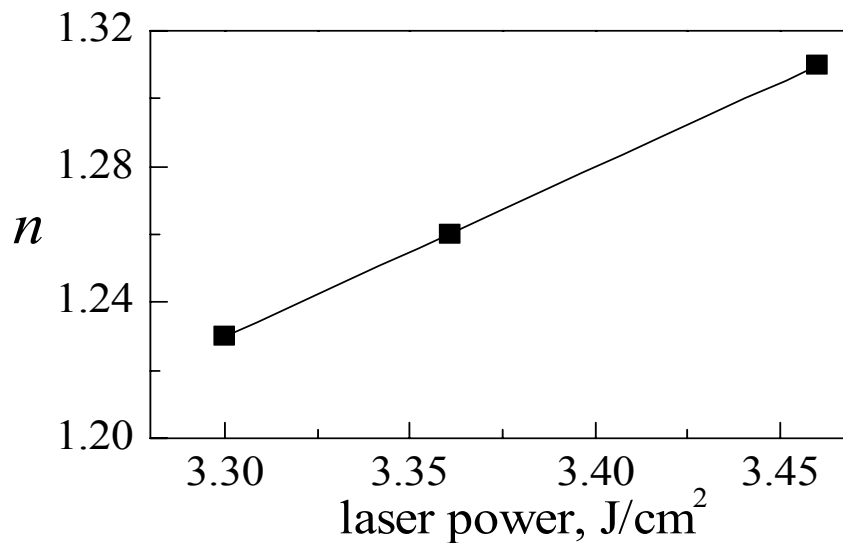
Figure 4.9 Variation of refractive index with the laser power; $T_s = 748$ K, $d = 50$ nm, $\lambda = 633$ nm.

4.4 Conclusion

SiO_2 thin films have been obtained by 1064 nm Nd:YAG laser oxidation of p-Si in the presence of O_2. The thickness uniformity, dielectric and electrical properties, and optical characteristics of the layers have been studied.

MOS capacitors fabricated on the grown oxide exhibited typical C-V and G-V characteristics. Reflectance, refractive index and physical thickness values were

measured by spectrophotometer. Refractive index and thickness from spectroscopy were compared to the ellipsometric measurements while reflectance measurements were compared to the conventional thermally grown oxides' results. The density of interface states and oxide charges were found and compared to the values of thermally grown oxides. Optical properties show that the Nd:YAG laser assisted oxidation of Si provides films whose thickness and refractive index can be controlled by the process conditions.

The results presented in this work allow us to draw the following conclusions. First, amorphous SiO_2 thin films can be successfully obtained by pulsed Nd:YAG laser in O_2 ambient at relatively low temperatures to those of conventional methods. The thickness of the oxide can be monitored easily with respect to the two essential parameters governing the laser oxidation: the laser beam energy density and the substrate temperature. The data suggest that the most desirable growth situation with respect to thicker oxides is to oxidize as close to laser power as possible corresponding to surface melting without crossing it. At the same time, however, the dielectric measurements in MOS configuration indicate that the laser-assisted oxide generally has parameters close to those of thermally grown SiO_2, such as interfacial defect charges, slow states density, leakage current and the capacitors showed true MOS behavior. Relatively high density of oxide charges is most likely due to the non-perfect microstructure of the oxide and the presence of excess Si, as detected by XPS (see chapter 5).

An inverse relationship of the reflectance with the wavelength is exhibited. The reflectance values are decreased in 300 – 800 nm spectral range for laser powers larger than 3.36 J/cm^2, i.e. an increase of optical thickness is detected. Only for relatively thick films with $d \geq 20$ nm, substrate temperature effect on oxidation is well pronounced. At higher substrate temperatures, the decay of reflectance is a proof of having the higher optical thicknesses. Obviously, the higher substrate temperature stimulates better oxidation revealing the denser films.

An inverse relationship of the refractive indices with wavelength is observed. The highest values of refractive indices are achieved at $\lambda = 300$ nm for a given film.

The refractive index gives the information on the degree of oxidation and the film density. Basing on the results presented in this chapter, one can conclude that to grow denser films the oxidation should take place at higher substrate temperatures and above 3.30 J/cm^2 laser power. In addition, refractive index depends on the film thickness, i.e. the higher the thickness, the lower the porosity and the higher the refractive index of the films.

The results show that refractive index of the laser oxidized films is smaller than that of the thermal SiO$_2$, i.e. laser oxidation produces the low denser films as compared to thermal oxidation. The detected suboxides in the films fabricated by laser assisted oxidation are believed to be giving this result. Thickness dependence of refractive index shows that the effect of suboxides is stronger for thinner films. This means that the laser oxidation technique is not able to produce dense enough layers for thin oxides. As an example, the refractive index has been found ~1.3 at λ = 300 nm for film thickness about 20 nm. In summary, optical properties show that the Nd:YAG laser oxidation of Si provides films whose optical thickness and refractive index can be controlled by the process conditions.

Further improvements could be obtained by appropriate post annealing processes. It can be concluded that the Nd:YAG laser oxidation is a promising technique for formation of small-spot oxide with desired dimensions and good oxide quality suitable to the demands of modern microelectronics. Although we do not yet understand the exact oxidation mechanism and the results raise many questions about growth process, the SiO$_2$ films formed by the technique of Nd:YAG laser–enhanced oxidation at low temperatures have been shown to be potentially useful technique for device applications.

CHAPTER 5

XPS STUDY OF PULSED Nd:YAG LASER OXIDIZED Si

5.1 Introduction

Microelectronics has been based on the Si technology during past a few decades since Si has native oxide, namely SiO_2, having perfect interface with Si. The constant shrinking of the device geometries forces the thickness of SiO_2 to its physical limits. Therefore, the development of new active dielectrics with high dielectric constant (high-κ materials) is a research subject [34,36,38]. At the same time, new methods of oxidation of Si for extremely thin SiO_2 growth is still a subject of ongoing investigations [2,3,39,40].

Novel methods of oxidation techniques have found an important investigation area in semiconductor technology for dielectric (mainly SiO_2–based) thin film growth. Recently, local and low temperature oxidation techniques such as Atomic Force Microscopy (AFM) grown oxides attract a huge number of scientists. AFM grown oxide patterns are generally used as masks for the selective etching and not as an active dielectric in the industrial scale since there are certain drawbacks in the production and application stage, such as low writing speed, poor reproducibility, since too thin layers, then, not sufficiently tough for subsequent process steps [3,39]. On the other hand, AFM grown SiO_2 oxides show larger current levels and lower breakdown voltages resulting in a poorer dielectric quality than thermally oxidized SiO_2 layers [3] and then not suitable as an active dielectric.

Due to the difficulties of mass production of AFM oxidized nanostructures, another oxidation technique, namely laser oxidation, has many advantages and great potential for the future semiconductor technology [6,14,41,42]. In addition to the advantages such as local oxidation and low processing temperatures, laser oxidation provides a good control over the thickness of very thin films including SiO_2 as shown in the previous chapter [4,14,41,42]. The advance of laser technology (well-controlled laser power, pulse energy, repetition rate, beam diameter etc.) helps us to grow better oxide layers on various semiconductors.

We have successfully obtained the amorphous thin SiO_2 films on Si substrate by 1064 nm wavelength pulsed Nd:YAG laser in O_2 ambient at relatively low temperatures. The thickness depth profiles by ellipsometer, MOS structures to extract the electrical, dielectrical and conductance properties and then the reflectance spectra and refractive index of the obtained SiO_2 layers on Si substrate were inspected in details (chapter 4).

The obtained electrical data are encouraging that the capacitors showed typical MOS behavior, i.e. interfacial defect charges, slow states' density and leakage current levels are close to those of thermally grown SiO_2. The investigations, on the other hand, force us to think about the chemical and structural analysis of the grown oxide layers since some results are the proof of existing suboxides in the oxide. The nonperfections, i.e. excess Si and suboxides, behave like active charge centers resulting in a high leakage current through the capacitor. In order to detect, identify and obtain the distribution in the oxide and at the interface of the various suboxides, X-ray Photoelectron Spectroscopy (XPS) analyses were conducted.

In this chapter, X-Ray Photoelectron Spectroscopy (XPS) to obtain the chemical and structural information of the oxides at the surface and at the interface with Si is presented in details. Based on these data, the laser parameters (laser beam energy density and substrate temperature) giving the best oxide quality in terms of the outcomes of capacitance-voltage and current-voltage measurements are discussed. Layers with thickness d of 40 nm were studied.

5.2 Experimental procedure

The Si substrate was p-type (100) oriented with a resistivity of 15 – 17 Ωcm. The Si wafer was cleaned to remove the native oxide from the wafer's surface (step 2 of section 3.2). Then, it was mounted onto the substrate holder of the chamber which was evacuated to a pressure below 0.13 Pa. After reaching the required substrate temperature, here T_s = 748 K, oxygen gas was sent into the chamber to obtain 123 Pa. Oxidation source was Nd:YAG laser at 1064 nm, (EKSPLA Pulsed Laser NL301). More details about the process of the laser oxidation can be found in chapter 3 and 4. Briefly, the laser beam energy density, P, was 3.41 J/cm^2 per pulse. The preliminary results show that the small variation of P, namely from 3.35 to 3.45 J/cm^2 has no effect on XPS results. According to the previous data, the better oxidation conditions were obtained for P value which was close to surface melting but without crossing it. The laser exposure time was 30 min. A computer-controlled X−Y scanner system was used to direct the laser beam on approximately 4 mm x 4 mm substrate area on the wafer. The oxide thickness was measured by an ellipsometer (λ = 632.8 nm).

The composition and chemical states in the film and its interface with Si were analyzed by XPS. The data were obtained using an AlK$_\alpha$ (1486.6 eV) excitation source in ESCALAB Mk II apparatus (VG Scientific) with a residual gas pressure better than 1x10^{-8} Pa. All spectra were taken at 300 K. The photoelectrons were separated by a semispherical analyzer with a pass energy of 10 eV and an instrumental resolution of 1.0 eV measured as the Full Width at Half Maximum (FWHM) of the Ag 3d$_{5/2}$ photoelectron peak. The energy position of the peaks was determined with an accuracy of 0.1 eV. The photoelectron lines of Si 2p and O 1s were recorded. The binding energies E_b have been corrected for sample charging effect with referenced to the C 1s line at 285.0 eV for the surface of the oxide and to the Si 2p line of the elemental Si at 98.7 eV for all spectra obtained after ion sputtering. The peak positions and widths were determined from least square fitting using the instrument's software. The peak shapes were fixed to a mixture of Gaussian-Lorentzian functions. The final fitting was made iteratively. The composition was calculated using the standard software. The spectra were obtained

under the angle of 90^0, (with respect to the surface plane) of photoemitted electrons. The chamber was also equipped with an ion source to facilitate in situ sputtering of the sample by Ar^+ to determine the concentration profiles of various species. The argon ion beam was with energy of 1.5 keV and a current density of 12 $\mu A/cm^2$. The angle of incidence of the sputtering beam was 40^0 with respect to the surface of the layer. The experimental curves are as-recorded data after Shirley background subtraction. It is very important to minimize the adverse effects of the ion beam on the sample stoichiometry during the ion sputtering. It is known [43] that 1−1.5 keV argon ions sputter conventional SiO_2 keeping its stoichiometric ratio, i.e. the ions remove Si and O at a rate very close to 1:2. That is why we assume that eventual unfavorable effects of the ion beam sputtering, such as a preferential sputtering should not influence considerably the experimental results and conclusions drawn from them. During sputtering the structural characteristics are probably in some way damaged but most likely this is not reflected on the Si 2p binding energy or its line width. For sputtering times, t_s, of 0.5 to 140 min, the thickness reduction as measured by XPS [44] was linear with t_s and the sputtering rate was obtained to be 3 Å/min. The sputtering rate determined by the oxide thickness and t_s was approximately the same, (2.9 Å/min) indicating that both methods are correct.

5.3 XPS Spectra of the films

X-ray photoelectron spectra (XPS) in the region of the Si 2p, O 1s and C 1s peaks were monitored. The binding energies E_b have been corrected for sample charging effect with referenced to the C 1s line at 285.0 eV for the surface of the oxide and to the Si 2p line of the elemental Si at 98.7 eV for all spectra obtained after ion sputtering.

5.3.1 Carbon signal

The spectrum at the surface shows a peak at C 1s region, (at 284.6 eV indicating the presence of C-C bond) with negligible intensity, demonstrating that the surface remains clean enough after short air exposure. The carbon signal is probably due to the adsorbate, which disappears when the surface is sputtered slightly.
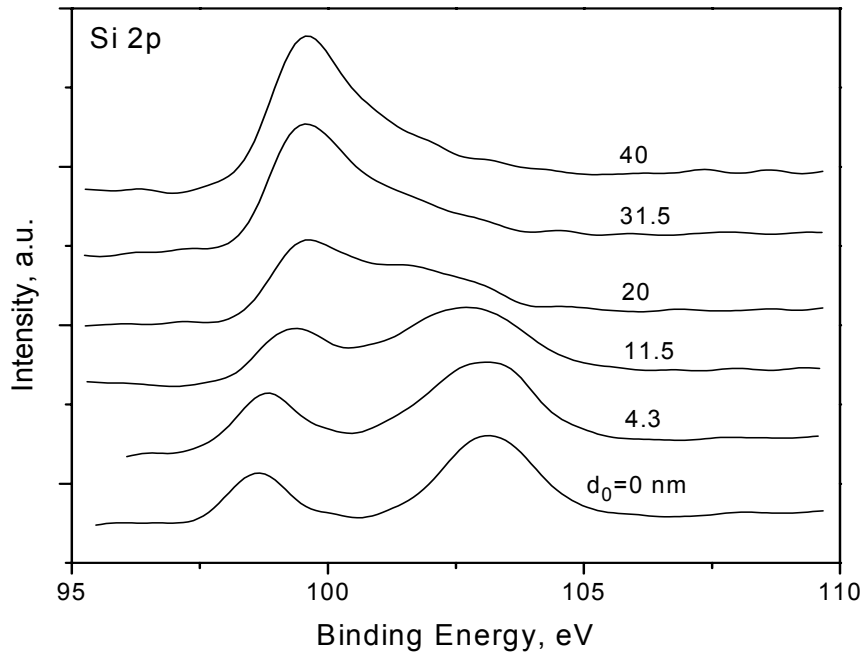
Figure 5.1 Si 2p depth photoelectron spectra.

5.3.2 Si 2p spectra

Figure 5.1 illustrates Si 2p spectra at 90° take-off angle for different depth profiles, i.e. different sputtering times (distance d_0 from the surface, respectively). Two peaks are seen in the Si 2p spectra at the surface, i.e. $d_0 = 0$ nm: one with higher binding energy located at 103.1 eV which is typical for Si_{2p}^{oxide} and the other with lower binding energy located at 98.7 eV for Si_{2p}^{Si} peaks. From these two peaks, Si_{2p}^{oxide} is more intensive than the other. As the sputtering evolves, the peak intensities and the shapes are changing resulting in a sharper and more intensive peak for Si_{2p}^{Si} while decreasing width for the Si_{2p}^{oxide} peak. The gradual shift to lower binding energies and an increase in the width of the Si_{2p}^{oxide} peak occurs showing an implication that Si_{2p}^{oxide} is transformed to suboxides at the depth spectra of the oxide. After the oxide depth of 15 nm, the main peak at the spectra comes from the

Si_{2p}^{Si} peak and not only a very wide but also a very tiny peak from Si_{2p}^{oxide} showing a sign that the oxide is mainly composed of suboxides.

In order to obtain more information about the types of suboxides, the depth spectra have been deconvoluted to Gaussian curves. Peaks' fitting has been made with a full width at half maximum of standard components and Gaussian-Lorentzian functions. The final fitting was made iteratively. Figure 5.2 a-d shows all the experimental and deconvoluted data of the Si 2p spectra for several selected sputtering times. The experimental curves are as-recorded data after Shirley background subtraction. The binding and FWHM energies of different peaks as well as their chemical energy shifts, Δ, with respect to the Si_{2p}^{Si} peak are presented as an inset in the figure. The binding energy shifts of the stoichiometric and intermediate oxidation state to lower energies are seen.

The relatively high intensity of Si_{2p}^{Si} line is probably due to the thickness nonuniformity of the laser oxidation in a wide range around the beam center (chapter 4). The thickness profile of laser oxidized SiO_2 is fitted to a Gaussian curve and a relative flat narrow range (active oxidized spot on the wafer) is about 1 mm from the center across which the thickness variation is within 10%. We believe that this thickness nonuniformity is responsible for the significant intensity of Si_{2p}^{Si} line rather than the presence of eventual non-oxidized elemental Si in the film, including at the surface. Additional support of this assumption is the nearly constant intensity through the depth of the layer up to the interface where strong signal from the substrate is detected, (Figure 5.2). The presence of pinholes in the layer should be also taken under consideration that the films with pinholes usually exhibit a larger signal from the bulk Si. If the layer is not continuous, it will give rise to an extra emission from pure Si through pinholes.
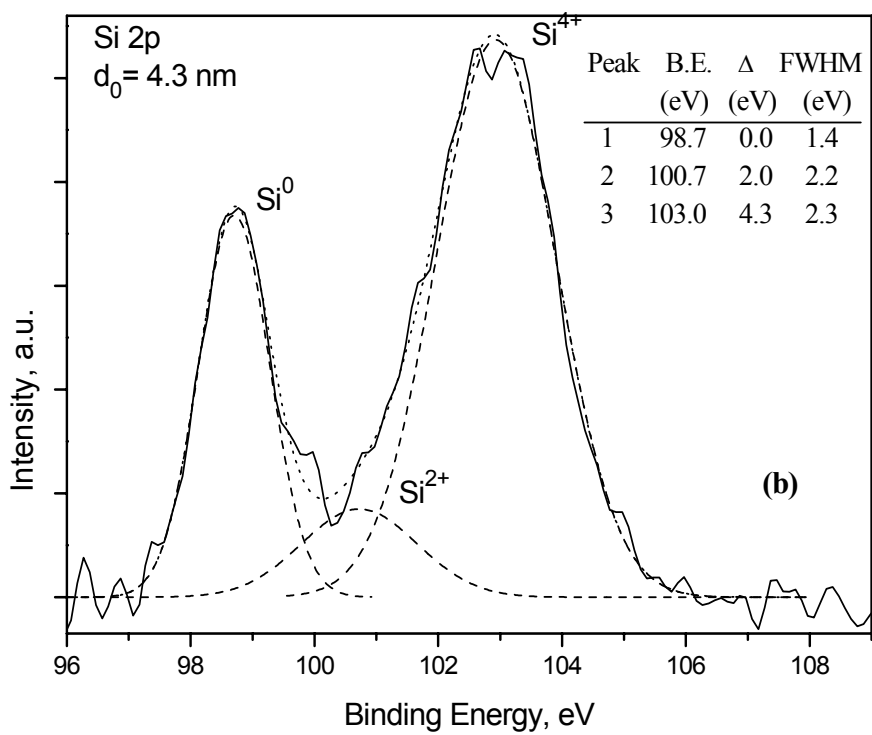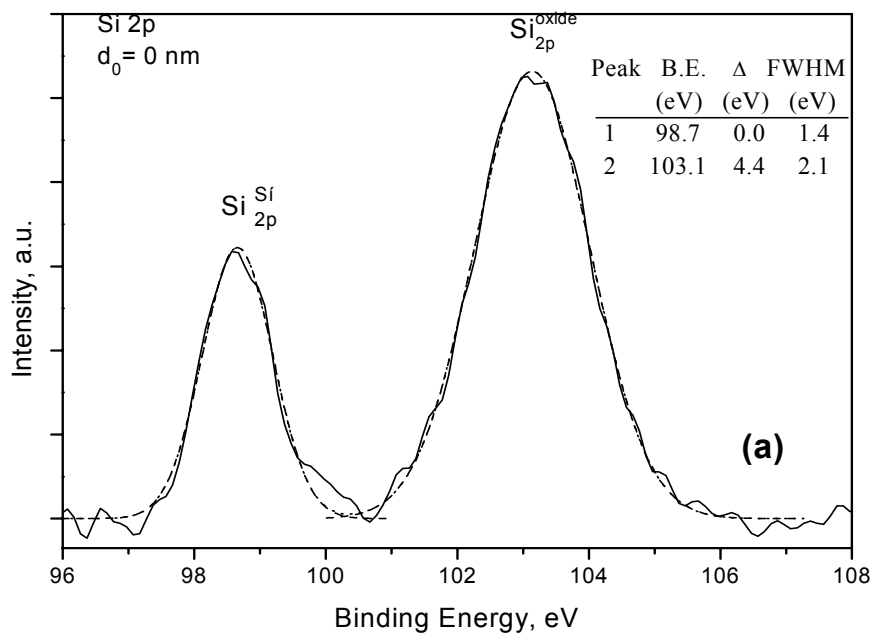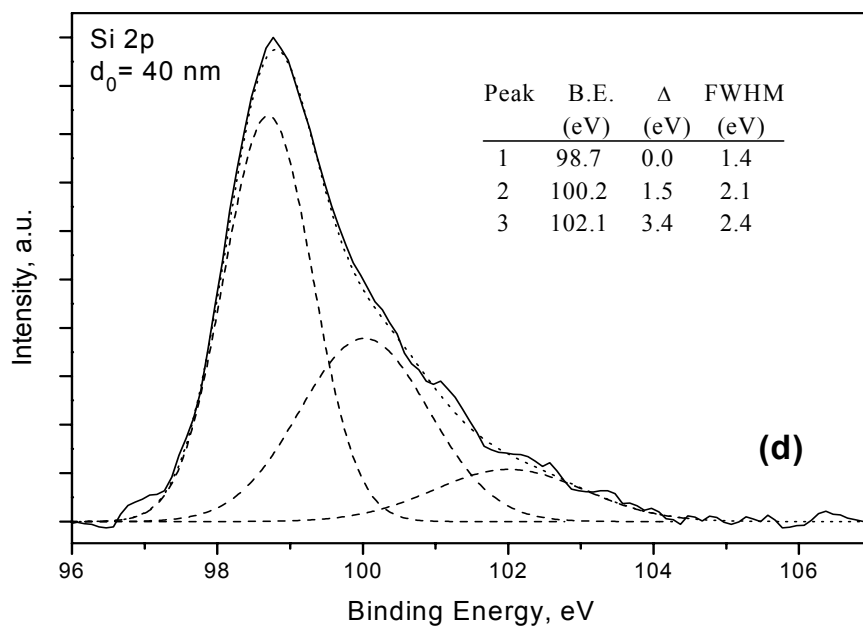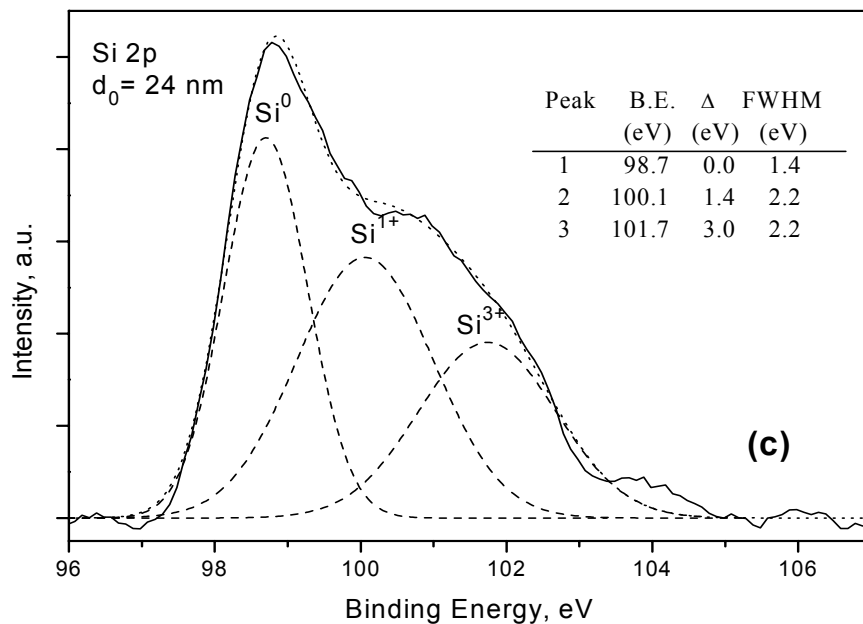
Figure 5.2 Decomposition of Si 2p spectra of laser oxidized SiO_2 for various distance from the surface: **a)** $d_0 = 0$ nm; **b)** 4.3 nm; **c)** 24 nm; **d)** 40 nm; (—— as-recorded data, ---- decomposition of the components). The corresponding oxidation states (see text) are indicated in the figures.

The analysis of the data for the best fit shows the followings. Si 2p has two peaks at the surface of the oxide, $d_0 = 0$ nm (Figure 5.2a). The first peak, associated with a signal from the Si substrate, Si_{2p}^{Si}, is fitted with a symmetrical line centered at 98.7 eV with a FWHM of 1.4 eV. The second peak, Si_{2p}^{oxide}, is centered at 103.1 eV with a FWHM of 2.1 eV which is a typical position of SiO_2 [45,46]. It is seen that there are two main peaks coming from the elemental Si (Si_{2p}^{Si}) and the stoichiometric oxide, SiO_2 (Si_{2p}^{oxide}) and no other intermediate oxidation states occur. The latter has a higher intensity. As is known [47] a peak at ~ 103.3 eV corresponds to Si–O–Si bond angle very close to 144^0 which is typical of amorphous SiO_2. Therefore, we interpret the spectrum at the surface ($d_0 = 0$ nm) as the film is composed of stoichiometric SiO_2.

As the sputtering process proceeds, the depth profile spectra reveal that the detected at the surface Si 2p line deforms and Si_{2p}^{oxide} line develops to a double peak structure. With increasing sputtering time the Si_{2p}^{oxide} peak shifts to lower energies, (Figure 5.1); at a distance of about 12 nm from the surface this shift is 3.3 eV as compared to the Si_{2p}^{Si} peak position. The binding energy and FWHM of the various peaks, (after deconvolution of the spectra) as well as their shift Δ with respect to the Si_{2p}^{Si} line are presented (tabular inset) in the Figure 5.2 a-d.

While the sputtering continues to t_s=15 min, (d_0=4.3 nm from the oxide surface), the deconvolution of the experimental data gives three peaks (Figure 5.2 b); one is located at 98.7 eV binding energy with FWHM value of 1.4 eV, Si_{2p}^{Si} (Si^0), second is 100.7 eV binding energy with FWHM value of 2.2 eV, Si_2O (Si^{2+}), and the third at 103.0 eV with FWHM of 2.3 eV, SiO_2 (or Si^{4+} according to the well known classification). The intensity of Si^{2+} component is about 6 times smaller than that of the main SiO_2 peak. There is small energy shift to lower energy side for the Si^{4+}, but being too small this is in the experimental error limits, (0.1 eV). The sum of the three peaks, i.e. elemental Si, (Si^0), stoichiometric SiO_2, (Si^{4+}) and intermediate Si^{2+} oxidation state, gives a spectrum equal to the experimental one.

The two lines, (Si^{4+} and Si^{2+}) present in the Si_{2p}^{oxide} peak exist until $d_0 \sim 20$ nm, but their intensities change with t_s: when thinning the oxide the intensity of stoichiometric Si^{4+} line decreases and the intensity of the suboxide Si^{2+} increases indicating the enhanced effect of the suboxide in the depth of the layer. The Si^{2+} peak is shifted from the elemental Si peak by 2.1−1.7 eV depending on d_0, which is consistent with the shift usually observed for this suboxide [46-49].

The qualitative change in the spectra is observed for d_0 greater than 20 nm, (Figures 5.1, 5.2): the Si_{2p}^{oxide} line changes its typical form to a broad peak with reduced intensity. The most pronounced effect of the change, however, is the missing of a signal of SiO_2 (Si^{4+}). The deconvolution of the spectra yields a set of three peaks (Figure 5.2 c) corresponding to Si^0 and two new intermediate oxidation states of Si, namely Si_2O (Si^{1+}) and Si_2O_3 (Si^{3+}) [47,48]; the SiO (Si^{2+}) peak disappears.

The variation of the intensity of the different peaks towards the interface with Si is such that after $d_0 \sim 25$ nm, the peak of Si dominates in the spectrum; the intensity of Si^{1+} does not change at all and Si^{3+} peak gradually loses its potency, but even just at the interface its intensity is not negligible (Figure 5.2 d) and is smaller than that of Si^{1+} by a factor of three. The Si^{1+} line is shifted by 1.4−1.5 eV from that of Si^0 and the Si^{3+} is shifted by 3.0–3.4 eV, respectively. This is in accordance with the observations [45-49] that about 1 eV shift of the oxidation state peak starting from the line of elemental Si with respect to each other.

At the interface, d_0=40 nm, the spectra consists of three peaks at 98.7 eV with FWHM value of 1.4 eV for Si^0, 100.2 eV with FWHM of 2.1 eV for Si^{1+} and 102.1 eV with FWHM value of 2.4 eV for Si^{3+}. The most intensive peak corresponding to elemental Si, Si^0, is followed by the intermediate oxidation state, Si^{1+}, and stoichiometric oxide, Si^{3+}.

As seen from Figure 5.2 a, the chemical shift Δ of the SiO_2 is 4.4 eV at the surface of the layer. This value is larger than that usually reported (3.8 eV) for thin SiO_2 films [50]. Similar large values of Δ have been reported previously [52] and have been associated to structural imperfections and nonhomogeneity of the layers. That

is why we assigned this higher detected chemical shift to the presence of structural nonperfections in the laser oxidized films, i.e. strained and/or broken Si–O bonds as well as intermediate oxidation states of Si atoms as evidenced by XPS data. Nearly constant value of Δ for SiO_2 through the depth of the layer (Figure 5.2 a-b) indicates a uniform distribution of the structural imperfections in this part of the layer that contains SiO_2, i.e. up to ~ 20 nm.

In Figure 5.3, the relative area under the peaks of the four oxidation states of Si as well as the area under the Si^0 peak is plotted as a function of d_0. The spectra exhibit clearly the distribution of the oxidation states through the depth of the oxide. It is clear that the film at the surface is completely stoichiometric SiO_2, while it is understoichiometric containing SiO_2 and SiO starting from a few nm deep from the surface until up to $d_0 \geq 20$ nm dominating SiO_2 up to $d_0 \sim 20$ nm. Si_2O and Si_2O_3 suboxides present in the whole interface region where the prevalent oxidation state is Si_2O, (Figure 5.3). The quantity of the suboxides is constant in the near interfacial region (~8 nm from the interface; the concentration of Si_2O_3 is threefold smaller). The existence of these intermediate oxidation states in the interfacial region and the presence of excess Si in a wide interfacial transition region clearly indicate a strong deviation from the ideal and atomically abrupt interface.
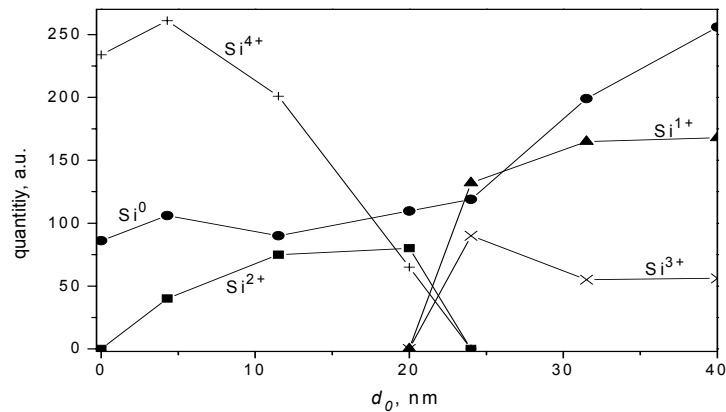
Figure 5.3 In depth distribution (peak areas) of the four silicon oxidation states and elemental silicon.

5.3.3 O 1s spectra

Figure 5.4 a-d shows the O 1s spectra for different sputtering times. The O 1s spectrum at the surface of the sample can actually be fitted to two Gaussian components (Figure 5.4 a). The main peak is located at 532.3 eV which is close to the expected position of SiO_2 [52]. The fact the position of the main peak not being at the exact place of SiO_2 but close to it is the influence of the lower oxidation state. On the other hand, the peak at 530.1 eV with three times smaller amplitude can be associated with poor oxidation state combined with surface contamination, such as carbon oxide or hydroxide. The FWHM values of the peaks are 1.8 eV for the main one and 1.4 eV for the smaller one. The energy positions of the peaks are not practically changed according to the fittings (Figure 5.4 b-d). The sum of these lines gives the experimental data for the O 1s peak and it changes both its position and shape through the depth of the layer.

The line at 531.1 eV is assigned to the elemental oxygen [52] and we will refer as O_{1s}^{O}. The higher binding energy line, referred as O_{1s}^{Si-O}, dominates in the spectra up to 20 – 24 nm, (Figure 5. 4) where its intensity equals to the intensity of the peak of elemental oxygen. The progressive reduction of the intensity of O_{1s}^{Si-O} peak as the film is sputtered is detected, while the intensity of O_{1s}^{O} one is practically constant suggesting the presence of elemental oxygen through the whole layer.

FWHM value of elemental O decreased until d_0 = 11.5 nm and increased again after this sputtering time to the interface. The binding energy of oxidation state of O shifts to lower energies starting from the surface of the oxide to the depth of 24 nm, i.e. d_0 = 24 nm. This behavior infers us that there is a deterioration of the oxidation state of silicon and the suboxides starts existing at some point of sputtering and increases, so there is an excess Si at the depth of oxide. FWHM value of oxidation state of O is 1.8 eV for the oxide surface, it slightly increases to the 2.8 eV value at d_0 = 24 nm depth from the surface, and it is almost constant after this point. That the increment of FWHM value of oxidation state of O while the sputtering increases is a sign of the excess Si at the depths of the oxide.

O 1s
$d_0 = 0$ nm

Peak	B.E. (eV)	FWHM (eV)
1	530.1	1.4
2	532.3	1.8

(a)

Intensity, a.u.

Binding Energy, eV

O 1s
$d_0 = 4.3$ nm

Peak	B.E. (eV)	FWHM (eV)
1	531.1	1.3
2	532.1	2.1

(b)

Intensity, a.u.

Binding Energy, eV
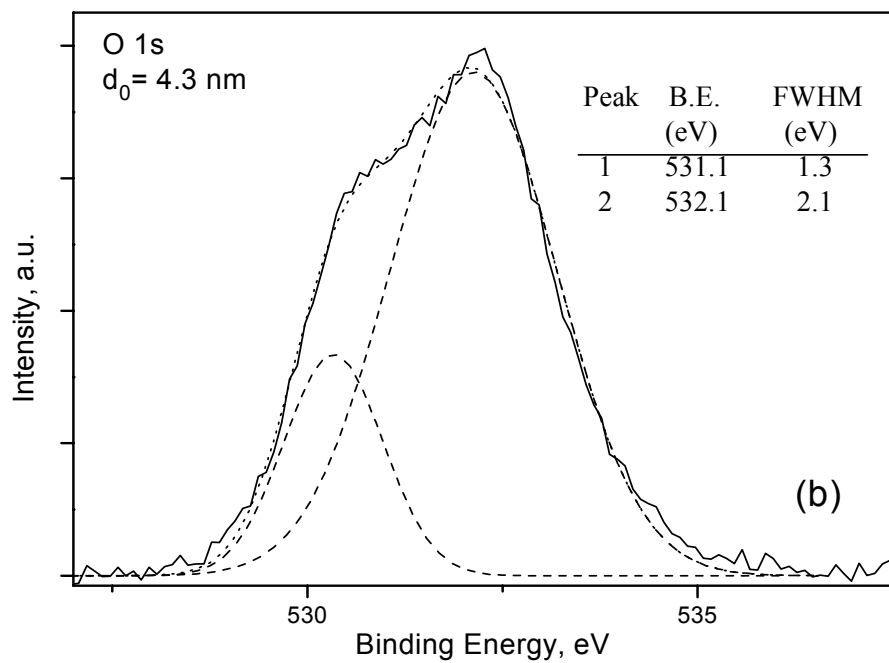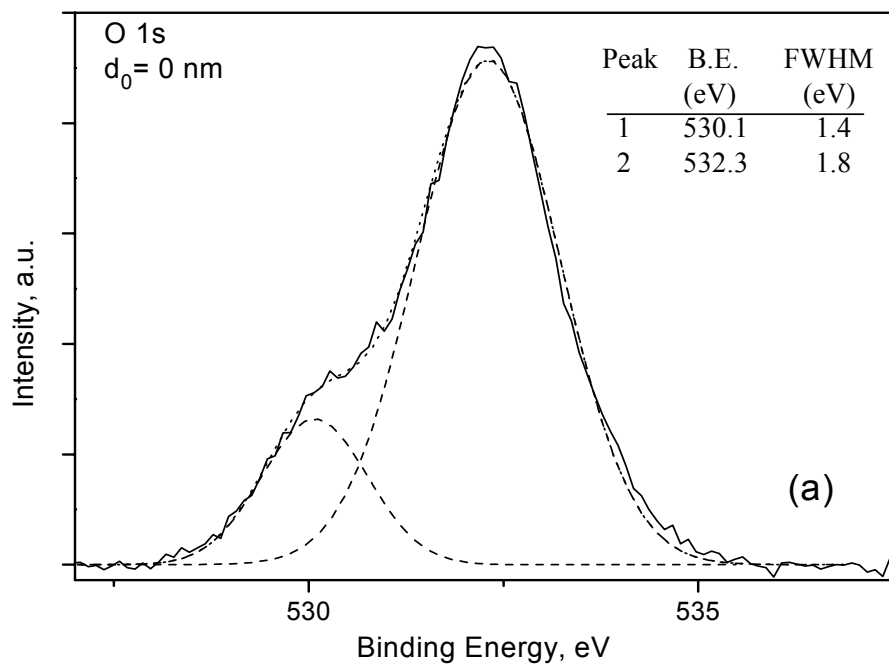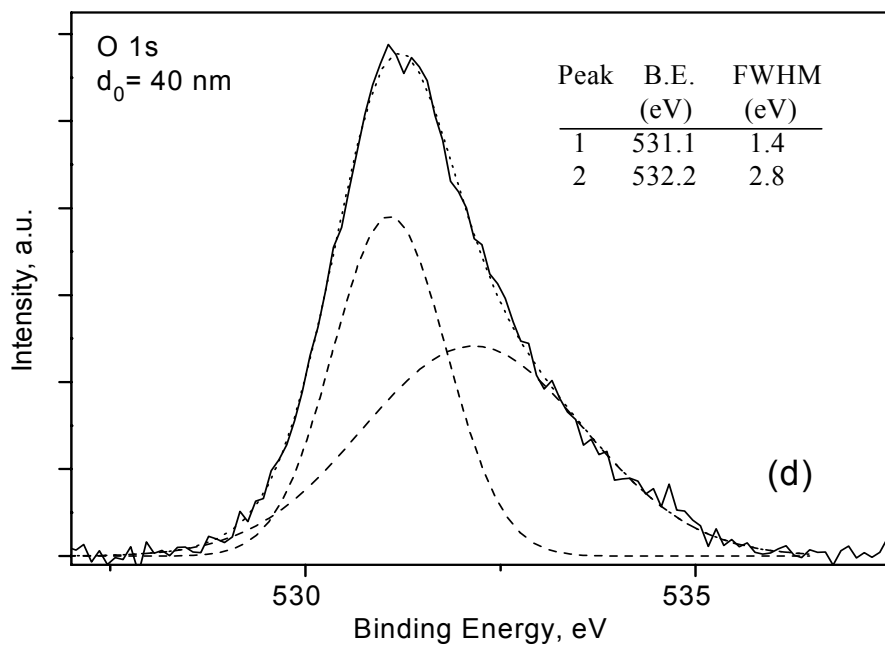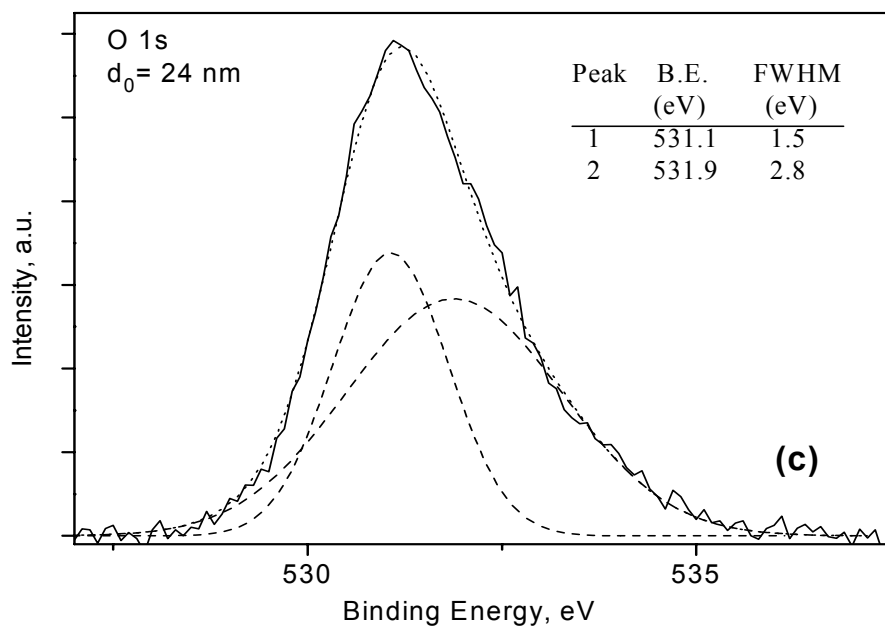
Figure 5.4 O 1s spectra for different d_0: **a)** $d_0 = 0$ nm, (at the surface of the layer); **b)** 4.3 nm; **c)** 24 nm; **d)** 40 nm; (—— as-recorded data, ---- after deconvolution).

Figure 5.5 shows the evolution of the O 1s intensity depth profiles corresponding to elemental O and bonded O with Si by thinning the film with sputtering. At the surface of the oxide, oxidation state of O is dominant to elemental O while the relative peak intensity changes during the sputtering process. O 1s peak shifts to lower energy for d_0 in the range 11–25 nm, indicating certain structural and compositional changes in the film at these depths, namely enhanced effect of suboxides. After around 4nm depth, the binding energy of elemental O 1s line is not changed up to the interface with Si.
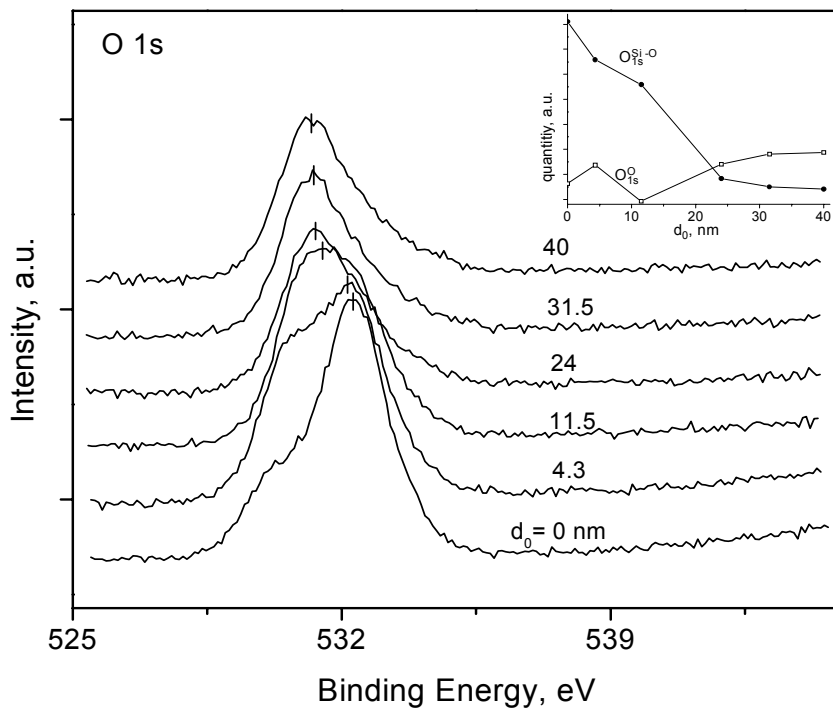
Figure 5.5 Comparison of O 1s spectra for various distances from the surface. Inset shows the depth profiles of O_{1s}^{oxide} and O_{1s}^{O} peak heights.

Intensity variation with d_0 of two peaks forming O 1s line is illustrated as an inset for Figure 5.5. The intensity of oxidation state of O is constantly decreasing as the sputtering proceeds, whereas, an inverse character is observed for the elemental O.

The intensities of elemental and bonded O are equal at the depth of around 23 nm, $d_0 = 23$ nm, the starting of the interface region. After this point, the dominant peak is the elemental O giving rise to constant intensities for both elemental and oxidized O state after the depth of 30 nm until the interface point with Si.

At present we have not clear explanation for the presence of non-bridging oxygen in the laser oxidized film. Generally there are two hypotheses for this phenomenon: i) spontaneous decomposition of some quantity of suboxides during Ar^+ bombardment. The low energy of Ar^+ ions, (1.5 keV) enables sputtering of SiO_2 unambiguously in a stoichiometric ratio, but this energy could be high enough to decompose intermediate oxidation states especially at the places with a large amount of nonperfect bonds (dangling and/or strained bonds) as it emerged indeed in our case. On the other hand, the thickness of the surface damaged layer with altered composition as a result of action of 1.5 keV Ar^+ ions is much smaller than the information depth of take off angle used [53]. This means that the XPS signal results from the steady state region of the layer and not from the surface distorted layer. The clarification of these effects is a nontrivial task especially in such kind of nonperfect oxide which is obviously laser oxidized SiO_2, and requires an additional precise investigation. ii) Various structural nonperfections in the layer including topological features and thickness nonuniformity may introduce an additional charge shift (regardless that the peak positions in the spectra are obtained after removal of charge shift) giving an inaccurate binding energy of the XPS lines. Based on these data, however, it is not possible to accept or to reject each of these two assumptions completely.

5.4 Conclusions

X-ray photoelectron spectra (XPS) for the pulsed Nd:YAG laser oxidation of Si with a laser beam energy density close to the corresponding one to surface melting but without crossing it. It is shown that this technique is a promising way for growing at nearly stoichiometric SiO_2 in the form of small spots with desirable thickness, (40 nm oxide obtained at 748 K was studied here) at low temperatures. The peak decomposition technique combined by depth profiling was employed to

identify the composition and chemical states throughout the films. It is established that the films are non-perfect and nonstoichiometric containing in general Si suboxides in different amounts throughout the depth. The oxide close to the surface exhibits a dominant SiO_2 state and smaller quantity of SiO. The interface between Si and laser – grown oxide is not abrupt, and the coexistence of Si_2O_3 and Si_2O suboxides in relatively wide interfacial region is found. It is concluded that post-oxidation annealing for improving microstructure of both oxide and near interface region is necessary.

CHAPTER 6

STRUCTURAL AND OPTICAL CHARACTERISTICS OF TANTALUM OXIDE GROWN BY PULSED Nd:YAG LASER OXIDATION

6.1 Introduction

High tunneling currents and reliability have been the results of the scaling limit of SiO$_2$-based insulators. To overcome these problems, high permittivity (high-κ) materials, such as single metal oxides and their silicates as well as ferroelectrics are being developed as alternative dielectrics in high density MOSFETs and Dynamic Random Access Memories, (DRAMs) [38]. One of the promising candidates is considered as Ta$_2$O$_5$ to replace SiO$_2$ as a memory dielectric in storage capacitors of Gigascale DRAMs, (sub-100 nm technology node) [35,38]. This material is mainly used as memory dielectric since it has excellent step coverage characteristics and high dielectric constant combined with relatively low leakage currents enabling high values of storage charges. Ta$_2$O$_5$-based DRAMs are also being produced nowadays by some manufacturers after many years of development [35]. Thermal oxidation of Ta film, rf sputtering, a variety of chemical vapor deposition techniques, ion beam deposition, atomic layer deposition, pulsed laser deposition are some of the methods to fabricate Ta$_2$O$_5$ film [1,34-36,54-67]. Since there are a variety of production techniques, competition among them from the investigations point of view is realized. On the other hand, each method has advantages and disadvantages in terms of mainly electrical properties that are essential for DRAM applications. It is not yet clear which method will be chosen as the best one with

respect to the storage capacitor applications because each fabrication method strongly affects the structural and electrical properties of grown Ta_2O_5.

The technique named as **P**ulsed **L**aser **O**xidation (PLO), however, is of a special interest in general for high-κ dielectrics among the various fabrication methods. The reasons why PLO is important for thin film growth process can be given in the following steps; i) local oxidation of small spots is possible, i.e. it has potential for nanoscale application and ii) PLO operates respectively at low substrate temperatures. Therefore, a number of problems which occur at high temperature processing of most high-κ dielectrics, particularly here for Ta_2O_5, such as undesirable reactions of the dielectrics with underlying Si resulting in a reduction of the benefits of high-κ material are minimized using this technique. If high-quality films with high dielectric constant are produced by PLO, an impact on the future high-κ dielectric technology will be realized. It is, therefore, vitally important to optimize the PLO parameters for obtaining the best methodology for the future applications. However, there is, at present, not enough experimental data for defining the properties of laser-grown Ta_2O_5 thin films from the view of DRAM storage capacitor application.

This chapter presents important experimental results for some structural and optical properties of Ta_2O_5 thin dielectric layers formed by pulsed Nd:YAG laser oxidation of Ta film on Si. Influence of both laser beam energy density and the substrate temperature on the effectiveness of the oxidation process in terms of structural perfections, amorphous status of the films and their refractive index values are discussed in details. Fourier Transform Infrared (FTIR) Spectroscopy and reflectance measurements at normal light incidence are used to characterize the structure, composition and optical properties of laser grown thin Ta_2O_5 films (20 – 50 nm) and their dependence on the oxide thickness, laser–beam–energy density and substrate temperature during oxidation. X-Ray Diffraction (XRD) method is used to detect the presence of crystal phase(s) in the grown layers. The results are discussed and compared with those of different groups which used other types of production methodologies for Ta_2O_5.

6.2 Experimental procedure

Tantalum films with a thickness from 10 to about 20 nm were deposited on Si by rf sputtering of tantalum target (99.99 % purity) in an Ar atmosphere. The working gas pressure, rf power density and the deposition rate were 3 Pa, 2.2 W/cm^2, 9.3 nm/min, respectively. The substrate was not intentionally heated during the tantalum deposition and presumably remained at temperatures close to room temperature. Subsequently, the samples were laser oxidized in vacuum chamber. The detailed procedure for laser oxidation of Ta film is given in section 3.3. The substrate temperature was between 250 and 400^{0}C. The main laser fluence varies in the range between 3.16 J cm^{-2} and 3.36 J cm^{-2} per pulse. Laser exposure times varied in the range of 30 – 60 min. More details on the laser oxidation system and laser parameters can be found in Chapter 3. The oxide thickness, d, and the refractive index, n, of the oxide layers obtained were initially determined by fixed wavelength ellipsometry, (λ = 632.8 nm); the films with $d \sim 20 – 50$ nm were studied. Additionally, both the refractive index and film thickness were determined with high accuracy in the spectral range $\lambda = 350 – 800$ nm, using reflectance measurements (Varian Cary 5E spectrophotometer with an accuracy of 0.5%) at normal light incidence [32]. The n and d of the layer were obtained by minimization of the objective function using the substrate trust region method based on the interior-reflective Newton method [33]. More details on the calculating procedure used can be found elsewhere [32 and chapter 4]. The thickness, dispersion energy and the single-oscillator energy were varied until a good fit between the measured and calculated values of R was found (accuracy better than 0.5%). The fit was accepted as successful when good enough accordance between ellipsometrically measured and fitted thickness was achieved. The preliminary experiments showed that the laser oxidation of a tantalum film with a thickness of about $d/2$ resulted in the formation of a tantalum-oxide film with a thickness about d. A Fourier Transform Infrared (FTIR) spectroscopy (BRUKER Equinox 55) was used to determine the chemical composition and structure of the films as a function of various oxidation parameters. The crystallinity of the films was examined by taking XRD patterns. The XRD analysis were carried out by using a Rigaku Miniflex

system equipped with CuK_α radiation of average wavelength 1.54059 Å. The XRD patterns were analyzed by a computer software and ICDD database which includes the diffraction patterns of well known structures. The peak matching process was carried out based on the observed peak positions at specific 2θ values and relative intensities of the peaks.

6.3 Results and discussion

6.3.1 FTIR spectra

FTIR spectra of Nd:YAG laser oxidized Ta films at various laser powers and substrate temperatures at a fixed working oxygen gas pressure (123 Pa) were taken. All FTIR samples used here were produced from laser oxidized Si wafers with 10 nm thick initial Ta films. The spectra were taken between 400 and 4000 cm^{-1}, but since the low wave number region (< 1100 cm^{-1}) is more important in determination of tantalum oxide, structure only the region of 400 to 1200 cm^{-1} is presented here. The results are used to search for the best oxidation regimes in terms of the homogeneity, density, structure and the composition of the oxide layers.

Figure 6.1 shows the FTIR spectra of the oxide layers for which the laser power was kept constant at around 3.21 J cm^{-2}, the laser oxidation time was ~ 30 min and the substrate temperature was varied between 250 and 400^{0}C. At the lowest substrate temperature, $T_s = 250^0$C, the effect of laser oxidation of Ta is very low showing that there is only a very small absorption peak around 650 cm^{-1} corresponding to Ta–O– Ta and Ta–O stretching vibration modes. As the substrate temperature is increased ($T_s \geq 300^0$C), the spectra show a main dominant dip centered around 650 cm^{-1} and a wide shoulder between 480 and 560 cm^{-1}, indicating that Ta–O–Ta and Ta–O stretching vibration modes of Ta_2O_5 exist in the oxide layer [64,68,70]. The sharp dip at 670 cm^{-1}, which is superimposed on the main signal is a result of the vibration modes of CO_2 resulting from the surrounding air in the FTIR spectroscopy. The absorption dip for the annealed sample is unexpectedly smaller than those of other samples that were annealed at lower temperatures. This is

believed to result from the variations in the laser power and focusing system. This behavior is not seen in the next sample set presented below.
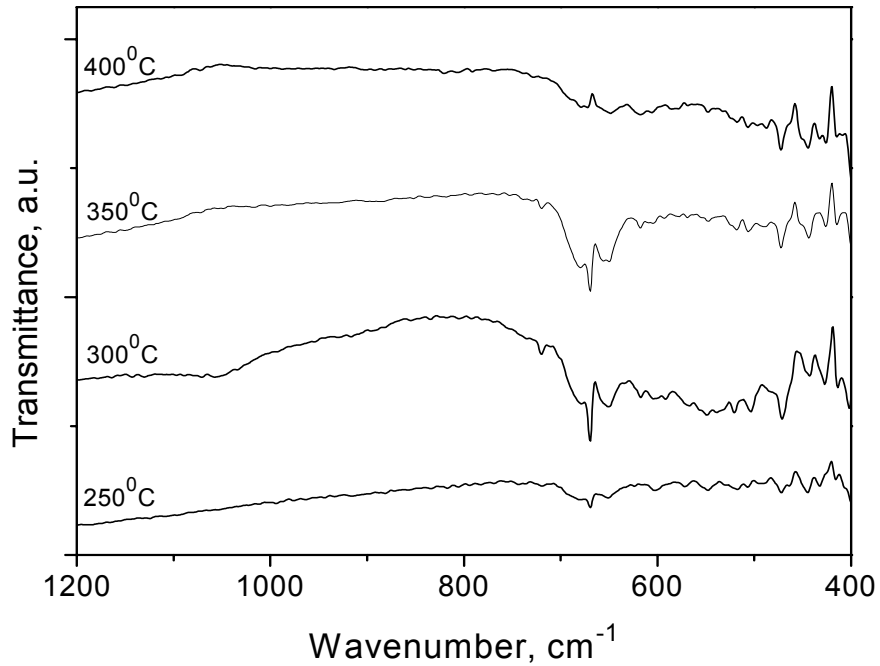
Figure 6.1 FTIR spectra of the oxide layers for various substrate temperatures, with constant and relatively the lowest applied laser power, 3.21 J/cm^2.

FTIR spectra of the sample set oxidized with a laser power of 3.31 J/cm^2 at various substrate temperatures, T_s, is shown in Figure 6.2. The sample with the lowest substrate temperature of 250^{0}C exhibits very small absorption dip centered around 650 cm^{-1}, showing that a tiny Ta_2O_5 film started to form at this temperature. When $T_s = 300^0$C, not only the depth of absorption dip at ~ 650 cm^{-1} is increased but also an absorption shoulder between 450 and 550 cm^{-1} appeared. These two signals are the results of Ta–O–Ta and Ta–O stretching vibration modes that are common to Ta_2O_5 [64,68,70]. However, a broad absorption band between 750 and 1050 cm^{-1}, corresponding to the presence of Ta suboxides appeared. This broad peak is reduced for $T_s = 350^0$C, while the intensity of ~ 650 cm^{-1} increased. We see also that the

position of shoulder like dip moved to higher wave numbers indicating that not only the amount of Ta–O–Ta and Ta–O stretching vibration modes are increased but also denser oxide films are obtained. As the substrate temperature is increased to 400^0C, the broadband peak between 750 and 1050 cm^{-1} disappeared showing that the amount of suboxides is very tiny at this temperature. On the other hand, the $\sim$ 650 cm^{-1} peak is sharper compared to those of other temperatures and the shoulder between 480 and 580 cm^{-1} is changed its position to even higher wave numbers indicating that the amount of Ta–O–Ta and Ta–O stretching vibration modes increased and denser Ta$_2$O$_5$ films were obtained.
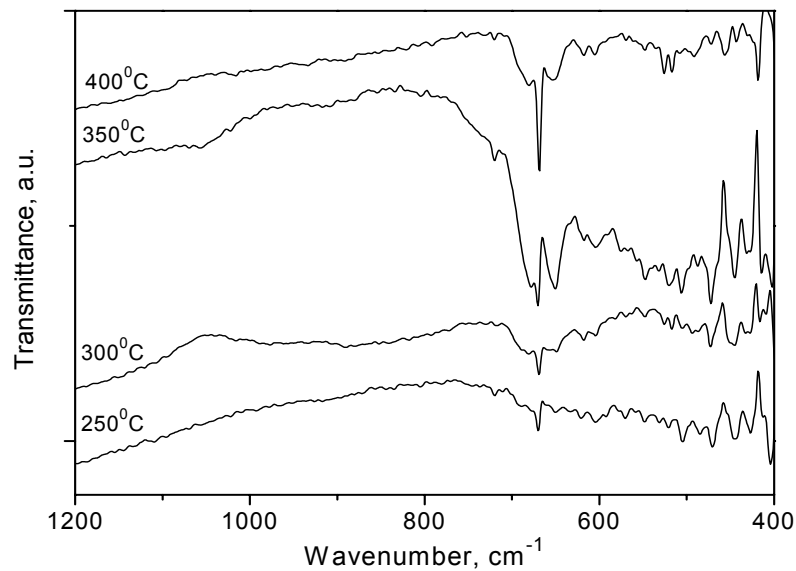

Figure 6.2 FTIR spectra of the oxide layers for various substrate temperatures, with constant and relatively the highest applied laser power, 3.31 J/cm^2.

The FTIR spectra of the oxide layers produced at the highest T_s (400^0C) with various laser powers, 3.21, 3.31 and 3.36 J/cm^2 is shown in Figure 6.3. As seen, the absorption peak $\sim$ 650 cm^{-1} gets sharper and deeper with increasing laser power, indicating that the Ta–O–Ta and Ta–O stretching vibration modes belonging to

Ta_2O_5 increase with the laser power increment. The position of the shoulder dip shifts its position to higher wave numbers from between 450 and 550 cm^{-1} for 3.21 J/cm^2 to between 470 and 550 cm^{-1} indicating that the obtained Ta_2O_5 layers are getting denser for higher used laser powers.
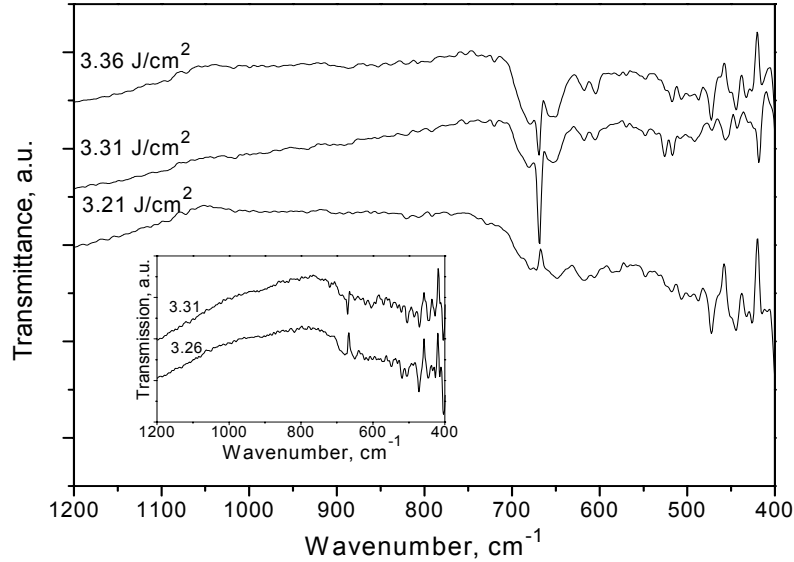
Figure 6.3 FTIR spectra of the oxide layers for the highest T_s and various P; 3.21, 3.31 and 3.36 J/cm^2 are shown. Inset shows the FTIR spectra for the lowest $T_s =$ 250^{0}C.

The inset of Figure 6.3 shows the FTIR spectra for lowest T_s (250^{0}C) and two preferably higher laser powers, 3.26 and 3.31 J/cm^2. The results show that there is only very tiny absorption dip at ~ 650 cm^{-1} corresponding to Ta–O–Ta and Ta–O modes of Ta_2O_5. This inset figure shows that laser oxidation of Ta with sufficient thickness is not possible even with the highest laser power. We can conclude from this result that the most important parameter for laser oxidation of Ta is the substrate temperature, T_s. Having chosen the most suitable T_s, the laser power should be adjusted to the possible highest necessary level for oxidation without melting the surface.

6.3.2 XRD results

X–ray diffraction (XRD) measurements were performed to determine the crystallinity of the laser oxidized Ta films. Figure 6.4 shows the XRD measurement results in Ta_2O_5 films oxidized at four different conditions. The substrates were also different for the samples where three of the substrates were the same (10 nm thick Ta layer on Si) and the fourth one was different (20 nm thick Ta layer on Si) in order to see the effect of Ta layer thickness on Si. The laser power was 3.31 J/cm^2 and the time duration was 30 min during the oxidation. The ellipsometrical measurements were performed after laser oxidation. The results showed that the oxide layer's thickness changes between 21 and 24 nm depending on the substrate temperature, with higher values corresponding to higher substrate temperatures, for the 10 nm thick Ta layer samples and around 41 nm from the initial 20 nm thick Ta layer. The refractive index values for these samples are between 1.93 and 2.22 showing that the oxide quality is as high as the thermally oxidized ones [34]. XRD measurements were performed on a series of films oxidized at different substrate temperature, T_s = 300, 350, 400^{0}C, while the other parameters, i.e. laser power, laser scanning time, oxygen pressure inside of the chamber during the oxidation were kept constant in order to obtain the substrate temperature effect on the crystallinity. The measurements showed that the films obtained at the condition of $T_s \leq 350^0$C are amorphous for all films, while the crystallinity starts when T_s = 400^{0}C produced from 10 nm thick Ta layers (see Figure 6.4 (a), (b), (c)). On the other hand, very tiny amount of crystallinity, i.e. crystalline grains, starts to be seen for the oxide layers produced from 20 nm thick Ta layers oxidized at T_s = 350^{0}C (see Figure 6.4 (d)). The most intensive peak at 2Θ = 33.26^0 corresponds to the Si peak resulting from the substrate. The highest intensity for the Ta oxidized structure were recorded at 2Θ = 23.24^0 with the Full Width at Half Maximum (FWHM) value of 0.635 and the second intensive one at 2Θ = 28.86^0 with FWHM value of 0.471 for the sample produced at T_s = 400^{0}C of 10 nm thick Ta substrate. As understood from the FWHM values, the XRD peaks are very broad (Figure 6.4) indicating that the level of crystallinity is very low. Therefore, the term of crystal grains or poly-crystallinity is more suitable for the crystal structure of our oxide layers. When the

peaks were compared to the ICDD database for Ta_2O_5, the crystal structure corresponds to the orthorhombic Ta_2O_5 with the card number of 71-0639 of ICDD database [69] and the dominant phase is orthorhombic β–Ta_2O_5 as obtained from other groups [59,70].
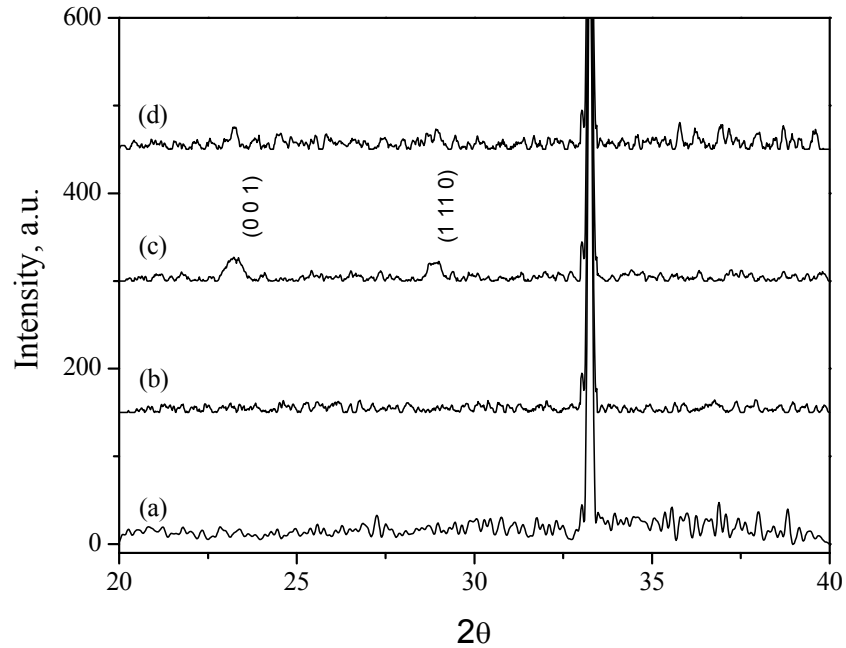
Figure 6.4 XRD results of laser oxidized Ta_2O_5 films for the following conditions;
        (a) $T_s = 300^0C$, d_{Ta}=10 nm, d_{oxide}=21 nm
        (b) $T_s = 350^0C$, d_{Ta}=10 nm, d_{oxide}=21 nm
        (c) $T_s = 400^0C$, d_{Ta}=10 nm, d_{oxide}=24 nm
        (d) $T_s = 350^0C$, d_{Ta}=20 nm, d_{oxide}=41 nm.

6.3.3 Reflectance spectra and refractive index

Influence of the substrate temperature on the reflectance spectra of 20 nm Ta_2O_5 films is shown in Figure 6.5. Oxygen pressure, P_{O2}, of 123 Pa and laser beam energy density, P, of 3.31 J/cm^2 were the laser oxidation parameters. The effect of small variation of P, ($P = 3.21$, 3.31 J/cm^2, respectively) around its optimum values

is studied for the films obtained at relatively higher substrate temperatures where the oxidation is expected to be more effective. There is exhibited also the reflectance spectrum of 10 nm Ta film on Si, (i.e. the spectrum of the initial sample before laser oxidation). The reflectance R decreases as T_s increases from 250 to 400^0C (Figure 6.5). This effect is more pronounced at smaller wavelengths, λ: the decrease in R is 15 – 18 % in the ultraviolet region ($\lambda = 350 – 400$ nm), and 12 – 16 % in the visible region. This reflectance drop is an indication of an increase in the optical thickness, which is defined as the product of the refractive index, n, of the layer and its physical thickness, d. The curves corresponding to 3.21 and 3.31 J/cm^2 for $T_s = 400^0$C are completely indistinguishable in all spectral range. Respectively, the reflectance curves at the same P values for $T_s = 350^0$C are almost the same and the difference is within the inevitable small thickness variation of laser oxidized films obtained at different conditions. That is why it can be concluded that the small changes in laser power have no effect on the film's reflectance for the film growth at higher T_s, (350 − 400^0C) and the oxidation processes produce layers with identical optical thickness. The highest drop of R is clearly visible in the whole spectral range as T_s increases from 250 to 300^0C with a decrease of 9 %. It is, therefore, inferred that the active oxidation starts somewhere between 250 and 300^0C substrate temperature. The reflectance spectrum of a Ta film on Si where the substrate was heated without laser oxidation is also a proof of this suggestion (Figure 6.5). That not any thermal oxidation occurs without laser action is obtained from the reflectance spectrum of metallic Ta where no changes are realized with T_s varying from 250 to 400^0C. Even though there are small optical thickness variations, the reflectance is not sensitive to them; i.e. the spectrum of metallic Ta film and the laser-oxidized layer at 250^0C are detected as the same (Figure 6.5). On the other hand, considerably different behavior than metallic Ta is exhibited when the oxidation takes place at T_s higher than 250^0C. Based on these results, that the active oxidation process starts somewhere when T_s greater than 250^0C can be concluded. Furthermore, an increase of T_s with a step of 50^0C resulted in a constant but smaller reduction of R, $\Delta R \sim 2 – 3$ % for $T_s \geq 300^0$C. The optical reflectance is ~ 28% in the visible region of the spectrum for the highest substrate temperature (400^0C) used here. Since R is a periodical function of the optical thickness with a

periodicity of $\lambda/2$, its changes with variation of nd, from zero to $\lambda/4$, depends on the ratio n/n_{sub} between refractive index n of the layer and of the substrate, n_{sub}, respectively; (R decreases when $n/n_{sub} < 1$ and opposite). If we suppose that the values of n are close to $2 - 2.2$, (the refractive index values typical of stoichiometric Ta_2O_5, [34,36,68]) the optical thickness, nd, will vary from $\lambda/8$ to $\lambda/18$ in the whole spectral range used and it will be generally smaller than $\lambda/4$. Considering that $n/n_{sub} < 1$, (for Si wafer, $n_{sub} = 5.60 - 3.66$ in the investigated spectral range), the decay of R could be attributed to the increase of optical thickness. It should be noted, however, that it is hard to draw a conclusion considering only the R spectral behavior because of the sophisticated relationship between R and n. The key role of the refractive index in these characteristics of the optical thickness is fairly plausible.
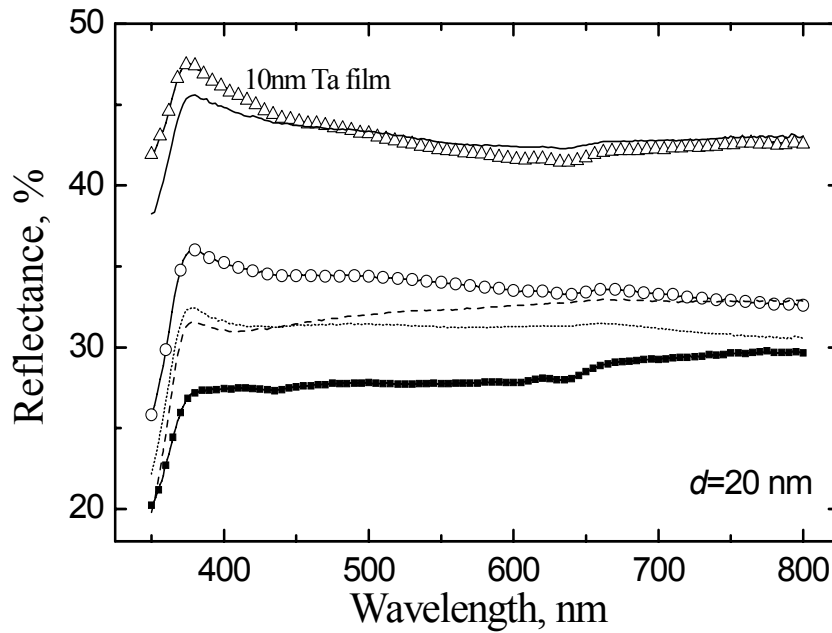
**Figure 6.5** Reflectance spectra of 20 nm laser oxidized Ta_2O_5 at various oxidation conditions, $P = 3.31$ J/cm^2: —— $T_s = 250^0$C; $\circ\circ\circ$ $T_s = 300^0$C; ----$T_s = 350^0$C; ■■■ $T_s = 400^0$C; $P = 3.21$ J/cm^2: ….. $T_s = 350^0$C; without laser power: $\triangle\triangle\triangle$ reflectance spectrum of 10 nm Ta film of heated substrate, $T_s = 250–400^0$C, (see the text).

Figure 6.6 presents the calculated values of n with respect to λ between 400 and 800 nm for three substrate temperatures. Curves for rf-sputtered (30 nm) Ta_2O_5 [71] and for different P value at $T_s = 400^0C$ are shown for comparison. The ellipsometrical values of n are in a very good accordance with the calculated ones at $\lambda \approx 633$ nm. The inset of the Figure 6.6 indicates the corresponding changes of n at 633 nm with T_s, ($P = 3.31$ J/cm^2). Generally, the dispersion curves exhibit a typical wavelength dependence of n for non- or slightly absorbing film, i.e. n decreases with increasing λ and tend to saturate at higher λ, ($\lambda \geq 600$ nm). Here, refractive index values, n, increased with the substrate temperature and this is attributed to the densification of the films. Since this increase is more sensitive when T_s is changed from 300 to 350^0C, it can be realized that the film undergoes a structural transformation upon oxidizing at T_s between 300 and 350^0C, while highest used T_s of 400^0C improved slightly refractive index. The improvement of refractive index value depends on the level of λ, i.e. the effect is stronger for the shorter wavelength region, ($\sim 400 - 600$ nm); the maximum increase of n, from 2.09 to 2.17 is detected at $\lambda = 400$ nm; the increase of T_s from 350 to 400^0C does not lead to change of n at all, for $\lambda > 650$ nm. The impact of T_s on refractive index suggests that at various substrate temperatures the growth processes have different controlling mechanisms resulting in the layers with different densifications. The dependence of n on T_s at $\lambda = 633$ nm (a photon energy of 1.96 eV), for $P = 3.31$ J/cm^2 presented as an inset in Figure 6.6. It is confirmed from this figure that the influence of T_s is especially important in the range 300–350^0C, where n arises with 0.12, achieving the value of 1.97, which is similar to the values reported for as-fabricated Ta_2O_5 films obtained by other methods [1,34,36,71]. Increasing T_s further to its highest value (400^0C) does not lead to any increase of refractive index at 633 nm. It is obvious that the dense enough as-grown oxides can be achieved at $T_s = 350 - 400^0C$. The effect of laser beam power at identical T_s, 400^0C, on refractive index is not detected at all (note that the curves for simplicity corresponding only to 3.21 and 3.31 J/cm^2 are shown in the figure even though the full laser power ranges 3.21 to 3.36 J/cm^2) (Figure 6.6). It is worth noting that the refractive indices of laser oxidized films, even for the highest T_s, do not reach those corresponding to rf sputtered films with similar thickness, indicating that the laser oxidation provides lower refractive index as

compared to the deposition process by rf sputtering of Ta target in Ar + O_2 mixture [1,71]. The possible reasons for the lower n values with laser oxidization technique could be the poor density, high porosity and oxygen deficiency of the layers. Stronger dispersion in the shorter wavelength region, $\approx$ 400–650 nm is, however, common for both types of Ta_2O_5; the sputtered and the laser oxidized layers. There could be two reasons for this result; either to the presence of suboxides which causes the adsorption edge to shift to larger wavelengths or to the large surface roughness. The suggestion of suboxides is a simpler explanation and it is completely consistent with rf sputtered samples [34] with the data of Auger and X-ray Photoelectron Spectroscopy (XPS) analyses where the presence of Ta suboxides was demonstrated through the depth of the layers. The detailed analyses for depth profiles by XPS measurements will be checked for the laser oxidized samples in near future, too.
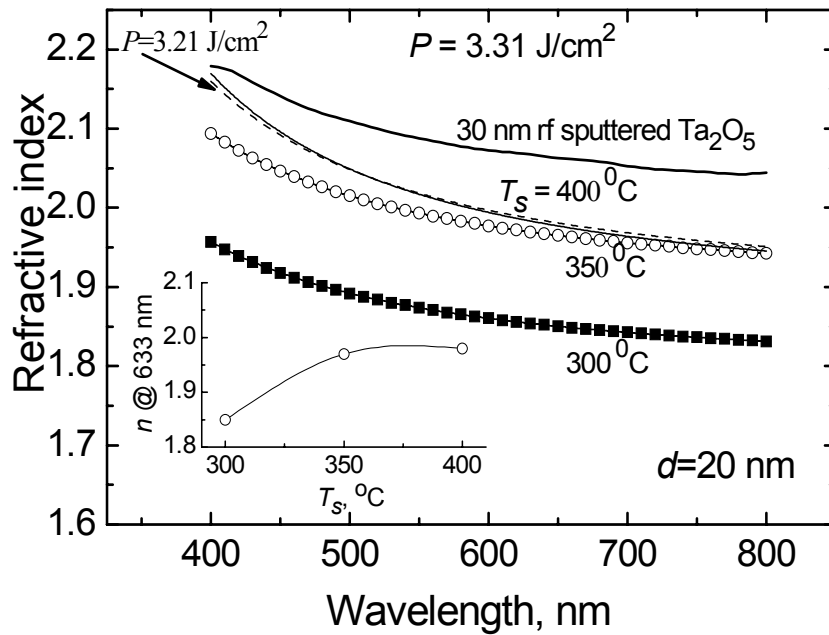

Figure 6.6 Refractive index as a function of λ for laser oxidized films obtained at different conditions; $n(\lambda)$ dependence of rf sputtered Ta_2O_5 (taken from [71]) is shown for comparison. The inset shows variation of n at 633 nm, with T_s, P = 3.31 J/cm^2.

The refractive index of the films was found to increase as the film thickness increased. The dispersion curves of n for three oxide thicknesses as measured ellipsometrically, ($P = 3.36$ J/cm^2 and $T_s = 400^0$C) are presented in Figure 6.7. The data of as–deposited rf sputtered 30 and 52 nm thick Ta_2O_5 films [71] are also given for comparison. The highest refractive index is obtained for the thickest laser-oxidized layer, (47 nm): the values of n are very close to those of 52 nm rf sputtered Ta_2O_5 in the range of $\lambda \geq 550$ nm, (the difference is only $0.01 - 0.03$) despite the laser-oxidized film is a little thinner. The values of n in the whole spectral range for both 37 nm laser-oxidized and 30 nm rf sputtered Ta_2O_5 are almost the same. Therefore, the results suggest that the laser oxidation of Ta films to thicknesses of above ~ 35 nm Ta_2O_5 provides layers with the same density, (in terms of refractive index) as sputtered Ta_2O_5. Consequently, it can be expected that the two types of oxides have similar chemical composition. Refractive index at 633 nm with respect to film thickness for laser–oxidized and rf sputtered Ta_2O_5 is given as an inset to Figure 6.7. Generally, the thickness dependence of n seems to be attributed to the better density of thicker films, (densified oxides with a better stoichiometry), resulting in a reduction of the interatomic spacing. Since the refractive index is proportional to the electronic polarizability which is inversely proportional to the interatomic spacing, the reduction of this spacing for thicker films directly results in an increase of their refractive index. The observed weaker dispersion of the thicker films as compared to the thinnest one suggests the improved stoichiometry of thick films too.
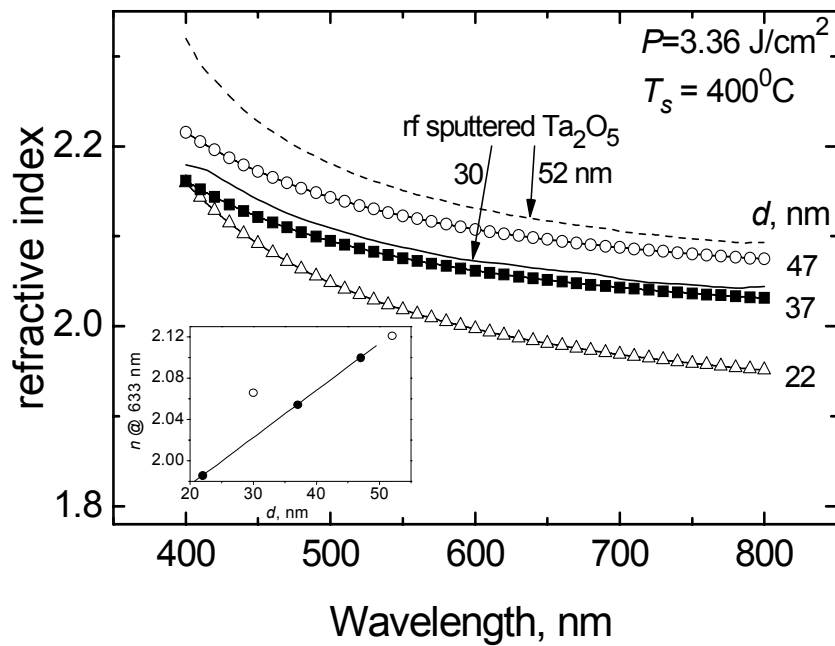
Figure 6.7 Dependence of refractive index on λ for the laser oxidized films with various physical thickness, $P = 3.36$ J/cm^2; $T_s = 400^0$C. The curves corresponding to two rf sputtered Ta$_2$O$_5$ samples (taken from [71]) are given for comparison. The inset shows the plot of n vs. d; • laser–oxidized; $\circ$ sputtered Ta$_2$O$_5$.

6.4 Conclusion

The Nd:YAG laser-assisted oxidation is used here as a technique to oxidize $10 - 20$ nm thick Ta layers at a laser beam energy density in the range $3.16 - 3.36$ J/cm^2 per pulse and the substrate temperature in the range of $250 - 400^0$C. The properties of laser grown oxide layers are examined by FTIR spectroscopy, XRD measurements and optical measurements for reflectance and refractive index values of the oxide layers.

In the FTIR spectroscopy measurements, the most important parameter is found to be the substrate temperature other than the laser power used. For the lowest studied

T_s (250^{0}C), there is only a small amount of tantalum oxidized layer, however, when the temperature is increased to 350^{0}C or higher values, the amount of suboxides decreases and consequently absorption dips related to Ta$_2$O$_5$ become more visible and intensive which indicates that the films obtained at $T_s \geq 350^0$C are mostly Ta$_2$O$_5$ structure with a small amount of suboxides.

XRD measurements revealed that the films obtained at the condition of $T_s < 350^0$C are amorphous for all films, but the crystallinity starts for the films produced from 10 nm thick Ta layers when $T_s = 400^0$C. However, crystalline grains, i.e. very tiny amount of crystallinity starts to be seen for the oxide layers produced from relatively thick 20 nm Ta layers oxidized at $T_s = 350^0$C. Very low crystallinity levels can be inferred since the detected XRD peaks are very broad having a high FWHM values. Therefore, the term of crystal grains or poly-crystallinity is more suitable for the crystal structure of our oxide layers and the dominant phase is orthorhombic β–Ta$_2$O$_5$.

Reflectance values with respect to wavelength from optical measurements show that the active oxidizing starts at between 250 and 300^{0}C. Reflectance values decreased with increasing T_s shows that the denser layers are grown when T_s is increased. As a consequence, the refractive index values increased when T_s is increased. Refractive index values, n, are inversely proportional to wavelength in accordance with the ellipsometric measured values. Having the dominant effect for T_s values between 300^{0}C and 350^{0}C, higher n values are obtained with increasing T_s.

CHAPTER 7

THICKNESS PROFILE AND ELECTRICAL PROPERTIES OF TANTALUM OXIDE FILMS GROWN BY Nd:YAG LASER OXIDATION

7.1 Introduction

Since the conventional SiO_2 based insulators reached their physical limits in terms of oxide thickness, alternative dielectric materials need to be searched for future DRAM application as storage capacitors. Vitally important points for a memory capacitor are to grow films with very high dielectric constant and very low leakage current levels. High–κ materials such as ZrO_2, HfO_2, Y_2O_3, TiO_2 and Ta_2O_5 increase the packing density without a further reduction of dielectric material's thickness since they have high dielectric constant values. Among these materials, Ta_2O_5 is one of the best candidate material since it has a high dielectric constant having value of greater than 20 (depending on the conditions during growth), high breakdown field, relatively low leakage currents resulting in a high storage charges and chemically stable structure [1,36,38,57,72,73].

There are a number of methods used to grow Ta_2O_5 layers. These are thermal oxidation, oxidation of sputtered layers of tantalum, a various ways of chemical vapor deposition technique, sputtering, evaporation, sol-gel methods, atomic layer deposition, ion-assisted deposition, laser oxidation of sputtered Ta layer [36,57].

Pulsed Laser Oxidation of rf-sputtered Ta layer can be used as an alternative technique for the production of Ta_2O_5. Being a local and low temperature process, laser oxidation is an interesting approach to the production of future devices (see

chapter 4). The chemical, electrical, optical and structural properties of obtained Ta_2O_5 layers need to be studied for these future applications of microelectronics. In this chapter, a study on the thickness distribution and dielectric and electrical parameters of pulsed Nd:YAG laser grown of rf-sputtered Ta layers are presented.

7.2 Experimental procedure

p-type Si substrates with a resistivity of 15-17 Ωcm were cleaned from the native oxide and loaded into the vacuum chamber in order to oxidize the rf-sputtered Ta films on Si substrate (see section 3.3 for details of the process). The substrate temperature varied between 250 and 400^0C, the laser beam energy density was between 3.21 and 3.36 J/cm^2 per pulse, the oxygen gas pressure was either 123 or 680 Pa and the rf-sputtered Ta thickness is 10, 15 or 20 nm for various samples. More details about the oxidation system and the oxidation process are given in Chapter 3 and 4.

After the oxidation process of Ta films was completed, thickness and refractive index values were measured by using an ellipsometer at 633 nm wavelength. Then, the MOS capacitors were constructed (see section 3.5) in order to obtain the electrical characteristics, i.e. Capacitance-Voltage (C-V), Conductance-Voltage (G-V) and Current-Voltage (I-V). For the capacitance and conductance measurements, high frequency regime (1k, 10k, 100k, 1MHz) was used. Series resistance correction (see section 3.6.1.1) was performed for 1 MHz and 100 kHz C-V and G-V data. Different types of oxide charges (see section 2.3.2) and hysteresis effect were extracted from the C-V and G-V data.

7.3 Results and Discussions

7.3.1 Thickness Distribution

The ellipsometric measurement results of the oxide thickness variation with respect to the distance from the center of the oxidized region for different Ta films are shown in Figure 7.1. The thicknesses of rf-sputtered Ta films were 10, 15 and 20 nm before starting oxidation. The oxidation parameters which are given in the

figure caption were used to oxide all Ta films in order to obtain approximately twice the thickness of initial Ta film. The refractive index values measured by the ellipsometer are very close values to that of bulk Ta_2O_5, namely 1.9, 2.1 and 2.1 for 10 nm, 15 nm and 20 nm initial thick Ta films respectively. The values of the oxide thicknesses, being in the expected range, were ~ 22.5 nm for 10 nm Ta film, ~32.5 nm for 15 nm Ta film, 41.5 nm for 20 nm Ta film. The highest value of the oxide thickness, d, is measured at the center of the laser beam (denoted by "0" in figure 7.1) and the thickness distribution is approximately uniform across the laser irradiated region. As can be seen from this figure, the thickness distribution of the oxide layers is more homogenous for higher initial Ta film thicknesses. It is also seen that a relatively flat region can be found over the distance of 2 mm at the center of the laser beam, across which the thickness variation is within ~8% for oxide produced from 10 nm Ta film and 2.2 mm flat region is obtained for the oxides having higher initial Ta thick films, i.e. 15 and 20 nm initial Ta films.

Figure 7.2 shows the oxide thickness, d, as function of the distance from the center of laser beam for various laser beam energy densities. Other parameters were kept constant during oxidation: the substrate temperature T_s=350^{0}C, oxygen gas pressure P_{O2}=123 Pa and time duration t=30 min for 10 nm initial thick Ta film. The refractive index values are measured to be 1.9, 1.9 and 2.2 respectively for 3.26, 3.31 and 3.36 J/cm^2 respectively. From these results, it is obvious that the refractive index of the oxide film obtained at the laser power of 3.36 J/cm^2 is in the range of bulk Ta_2O_5's refractive index value. The shapes of the oxide thickness show that they all have Gaussian-like variation and the oxide thickness has the maximum value for all oxide layers at the center of the laser beam. As seen from Figure 7.2, the oxide thickness values are very close to each other for the lower two laser beam energy densities (in other words laser powers), namely ~19.5 nm for 3.26 J/cm^2 and 21 nm for 3.31 J/cm^2, but it suddenly increases to 26 nm for 3.36 J/cm^2 having a relatively narrow Gaussian thickness profile with respect to the other two laser powers ones. The thickness variation is obtained around 1.4% for P=3.26 and 3.31 J/cm^2 while it increases little bit more to ~1.7% for P=3.36 J/cm^2 over the distance of 1 mm from the laser beam center. These results show that the expected oxide

thickness, which is approximately twice that of initial Ta film is obtained at relatively lower laser powers, i.e. 3.26 – 3.31 J/cm^2, while it increases to ~2.5 times that of initial Ta film for the laser power of 3.36 J/cm^2. This could be due to the fact that a SiO$_2$ layer is formed at the interface between Ta$_2$O$_5$ and Si substrate. It is reasonable to assume that this happens at higher laser energies.
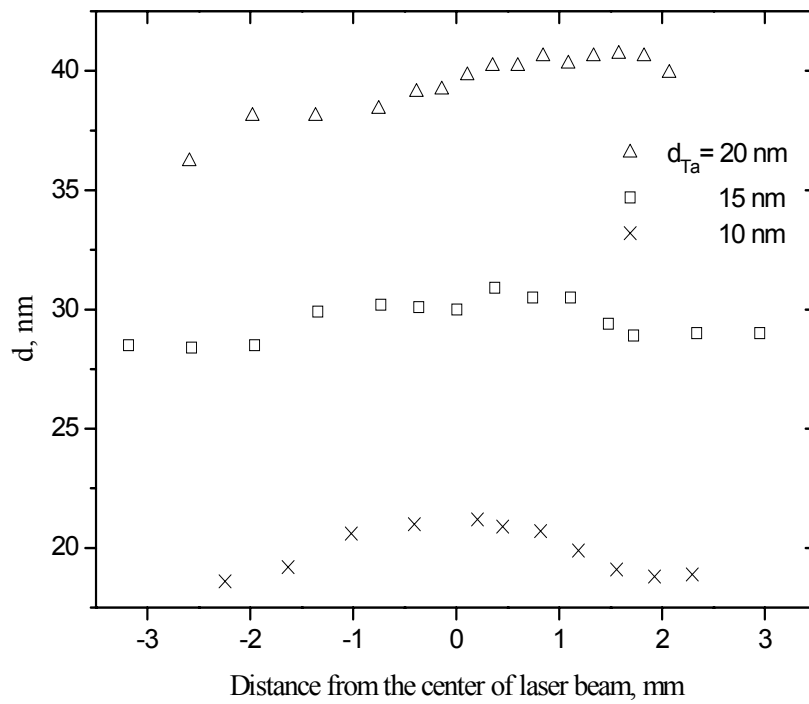

Figure 7.1 Oxide thickness versus distance from the center of laser beam. The constant parameters for all oxides are T_s=350^{0}C, P=3.31 J/cm^2, P_{O2}=123 Pa.
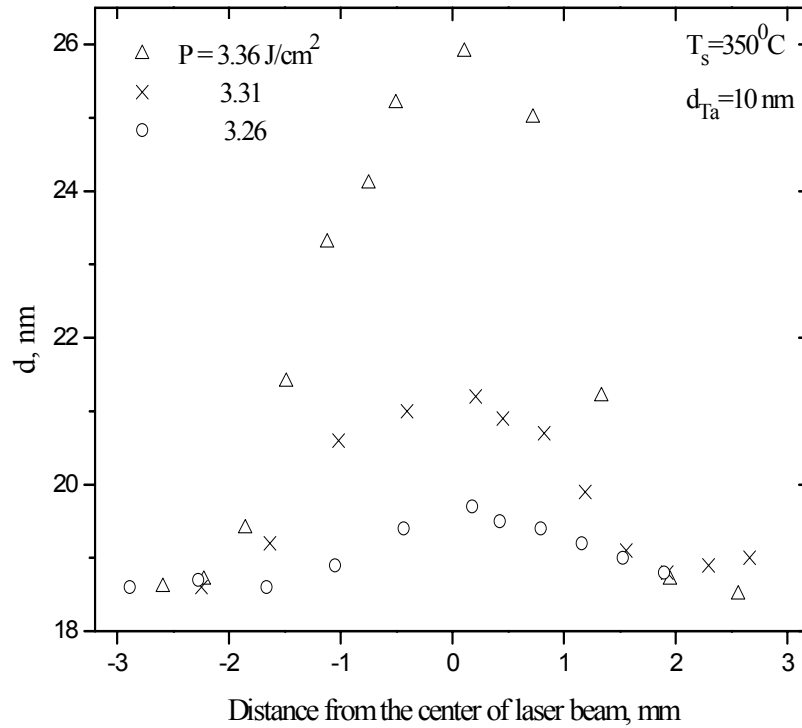
Figure 7.2 Oxide thickness versus distance from the center of laser beam for various used laser beam energy densities.

Figure 7.3 shows the oxide thickness as a function of distance from the laser beam center for variable T_s values; 250, 300, 350 and 400^0C. The other parameters are: oxygen pressure is P_{O2}=123 Pa, thickness of the Ta film is 15 nm. It is obvious that all the curves are in a Gaussian shape with a well-homogeneous region at the center, i.e. the thickness distribution over 1 mm at the center of the oxidized region changes between 0.5% and 0.7% which is very low. The maximum oxide thickness which is obtained at the center of the oxidized region is around 25.5 nm for 250^0C, 27.5 nm for 300^0C, 31 nm for 350^0C and 44 nm for 400^0C. According to these results, the expected oxide thickness for initial 15 nm thick Ta film is obtained for T_s=300-350^0C. However, it is too low having ~25.5 nm with an opposite shape of Gaussian form for thickness distribution corresponding to T_s=250^0C. This shape of thickness

distribution having the lowest thickness at the center and then sudden increase at the periphery is indicating that the layer is mostly metallic in the periphery, and a small region at the center is slightly oxidized. The refractive index values, which are the combination of all oxide layers formed on Si, measured by ellipsometer measurement data were 2.3, 2.1 and 2.0 respectively for 300^0C, 350^0C and 400^0C. Since the refractive index values are decreasing with increasing T_s and also the thickness for 400^0C increases suddenly in a large amount to about for 44 nm which is larger than the expected oxide thickness value (30 nm), it can be concluded that the Si substrate is also oxidized in addition to the oxidation of the Ta film.
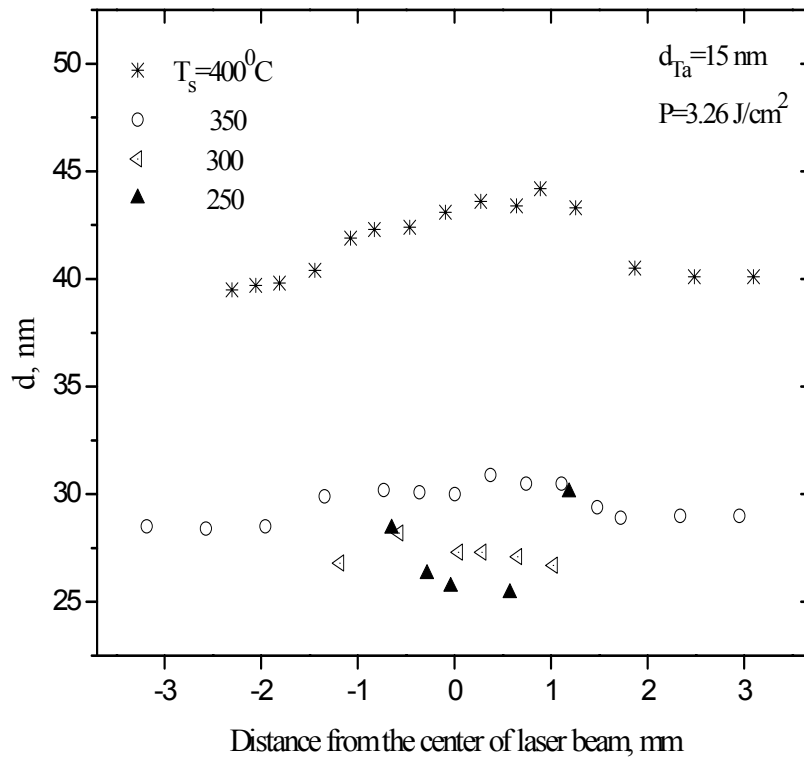

Figure 7.3 Oxide thickness versus distance from the center of laser beam for various T_s values.

7.3.2 Dielectric and electrical properties

7.3.2.1 Effective dielectric constant

In this section, the electrical properties, i.e. capacitance-voltage (C-V), conductance-voltage (G-V) and current-voltage (I-V) of 4 samples produced at T_s=250, 300, 350, 400^{0}C are presented. C – V curves were taken at high frequencies of 1 kHz, 10 kHz, 100 kHz and 1 MHz for MOS capacitors with 1.96 x 10^{-3} cm^{-2} Al gate area and series resistance correction (see section 3.6.1.1) were applied to 100 kHz and 1 MHz capacitance and conduction data. Using these experimental data, calculations have been carried out to obtain the effective dielectric constant of the oxide layer, ε_{eff}, flat band voltage, V_{FB}, fixed oxide charges, Q_f, slow (border) states, Q_s, and interface defect states, Q_{fast}. Figure 4 (a-d) shows C – V curves with accumulation, depletion and inversion regions and one G – V curve showing the conduction peak of MOS capacitors after the series resistance correction is applied.

The effective dielectric constant, ε_{eff}, of the oxide layers, most probably the combination of the native oxide on the Si substrate, SiO$_2$, and tantalum-oxide layer, were calculated from the capacitance at accumulation mode and the oxide thickness measured by ellipsometry. The ε_{eff} values corresponding to each High Frequency (HF) CV curve are given in Table 7.1 for all samples, and seen that almost all ε_{eff} values are higher than that of ideal SiO$_2$ as a proof that there exists an oxide layer with higher dielectric constant than that of SiO$_2$, ε_{SiO2} = 3.9. The ε_{eff} values of grown oxide films change between 15 and 19 at 1 MHz frequency limit except that of T_s = 250^{0}C oxide. The ε_{eff} values obtained from laser oxidation of Ta films are comparable to the values for oxides grown by other techniques [72,73]. For lower frequencies, the corresponding values of ε_{eff} increase, since accumulation capacitance value increases as frequency decreases.

$T_s = 250^0C$

(a)

1 kHz
10 kHz
100 kHz
1 MHz

100 kHz →

$T_s = 300^0C$

(b)

1 kHz
10 kHz
100 kHz
1 MHz
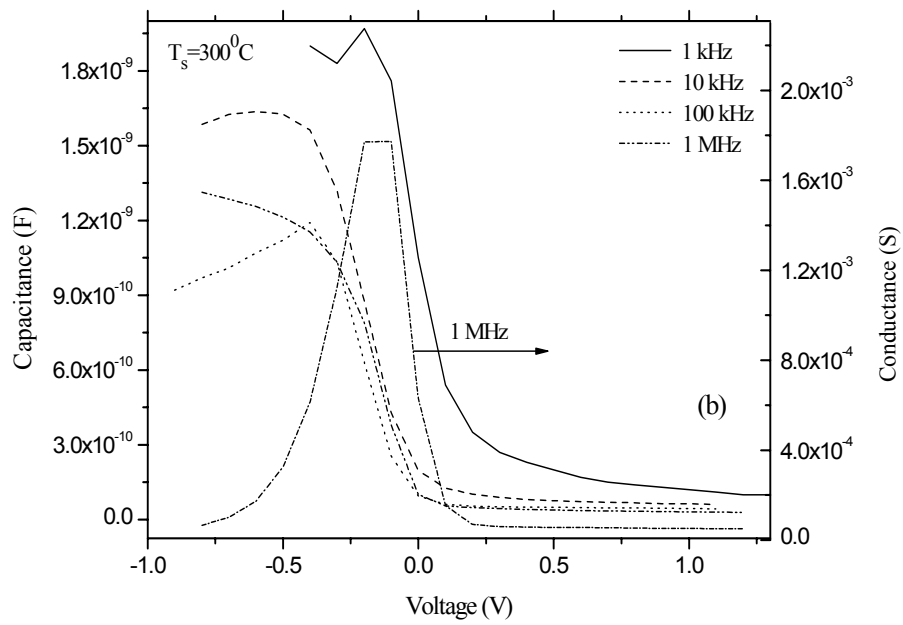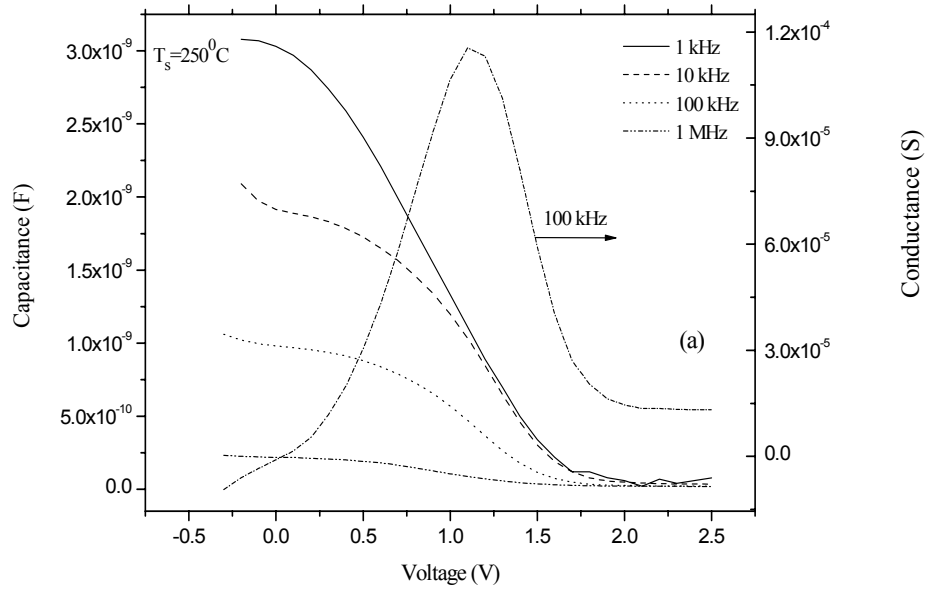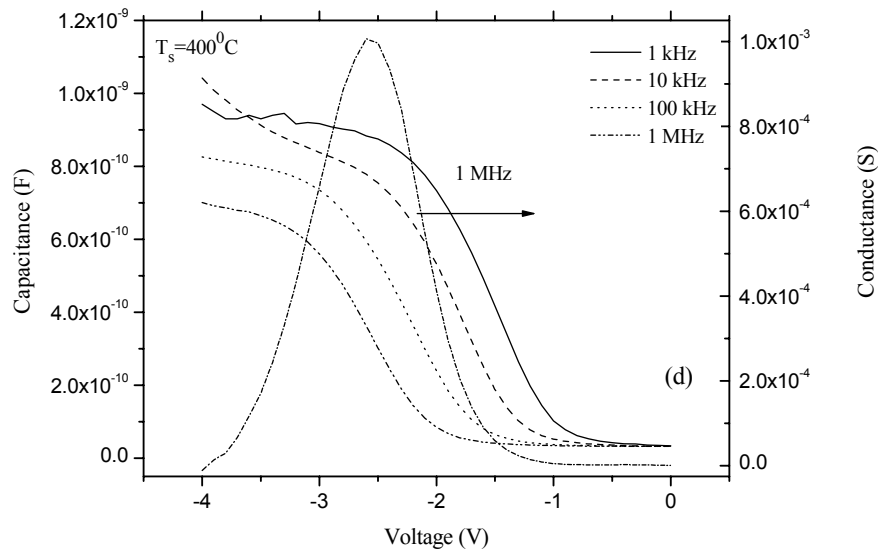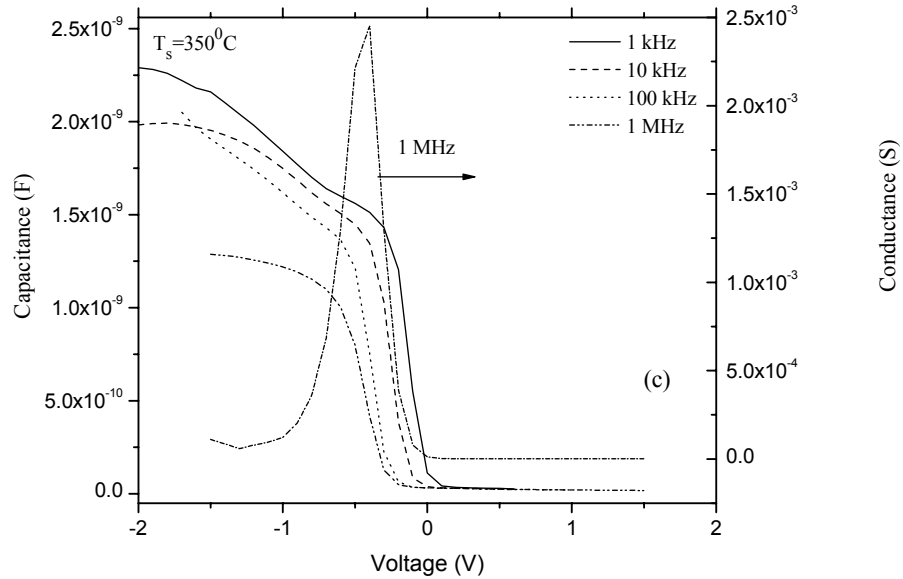
1 MHz →

Figure 7.4 Capacitance with respect to applied voltages for 1, 10, 100, 1000 kHz and conductance versus applied voltage for 100 kHz for T_s=250^{0}C and 1MHz for other conditions for;

    (a) T_s=250^{0}C
    (b) T_s=300^{0}C
    (c) T_s=350^{0}C
    (d) T_s=400^{0}C.

7.3.2.2 Charges in the grown oxide layer

The amount of fixed charge can be related to the value of V_{FB} by the following equation;

$$V_{FB} = \Phi_{MS} - \frac{Q_f}{C_{acc}} \tag{7.1}$$

where C_{acc} is the measured capacitance in accumulation. Using the flat band voltages, V_{FB}, obtained from the position at the conduction peak voltages and together with accumulation capacitance values, (the work function difference between Al gate and Si, Φ_{MS}, is -0.7 eV), the oxide charges, Q_f, are calculated and given in Table 7.1 for all samples at each frequency. When the flat band voltage is negative, then the expected presence of oxide charges is positive and vice versa. As seen from Table 7.1, Q_f is positive and ~3.6 x 10^{12} cm^{-2} for T_s=400^{0}C oxide, while it is negative and changes from ~(-1.2) to ~(-2.6) x 10^{12} cm^{-2} for T_s=250 – 300^{0}C oxides. The obtained Q_f values for laser grown oxides are even less than one order higher than those of common production methods of Ta_2O_5 films [72,73]. Fixed oxide charges often originate from the incomplete chemical bonding of the atoms near the dielectric/semiconductor interface [36]. One reason for these electrically active defects in Ta_2O_5 is the oxygen vacancies [72,73]. Therefore, some oxygen annealing treatments might reduce the Q_f values.

Table 7.1 Dielectric and electrical parameters obtained from capacitance and conductance data.

| T_s (°C)		400	350	300	250
	f (kHz)				
ε_{eff}	1000	19	15.1	16.8	3.24
	100	22.3	17.0	15.8	14.6
	10	23.8	23.9	21.7	28.0
	1	25.8	28.5	25.4	46.0
V_{FB} (V)	1000	-2.359	-0.255	-0.079	1.079
	100	-2.032	-0.218	-0.085	1.280
	10	-1.675	-0.059	-0.095	1.355
	1	-1.362	-0.014	0.072	1.338
Q_f (10^{12} cm^{-2})	1000	3.62	-1.76	-2.57	-1.23
	100	3.42	-2.11	-2.61	-6.14
	10	2.68	-4.05	-3.16	-12.3
	1	1.97	-5.12	-4.76	-20.0
Q_s (10^{11} cm^{-2})	1000	0.793	3.1	2.6	-1.8
Q_{fast} (10^{11} cm^{-2})	10 – 1000	19	9.1	0.69	0.54
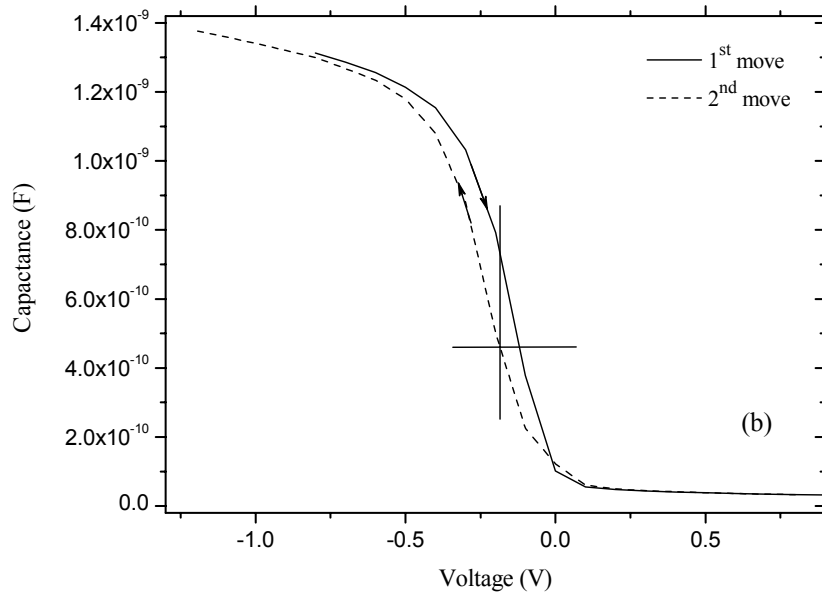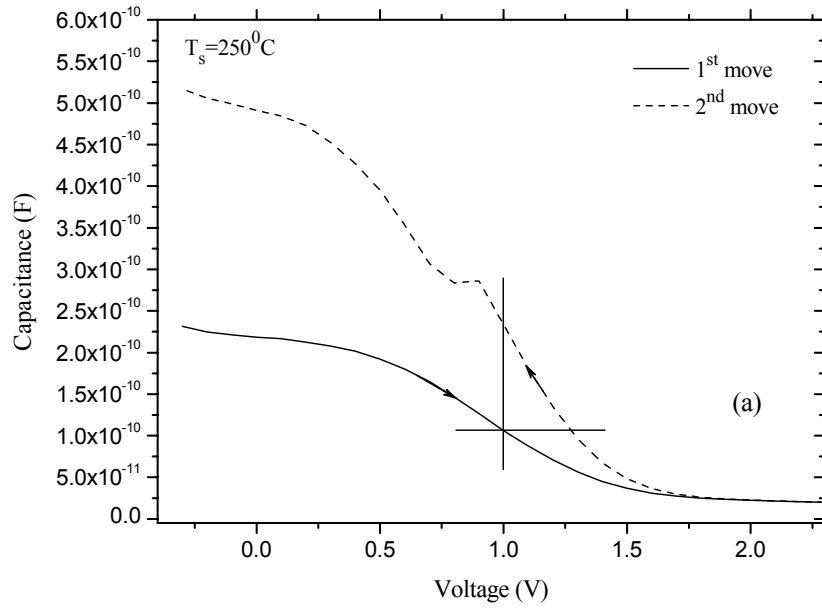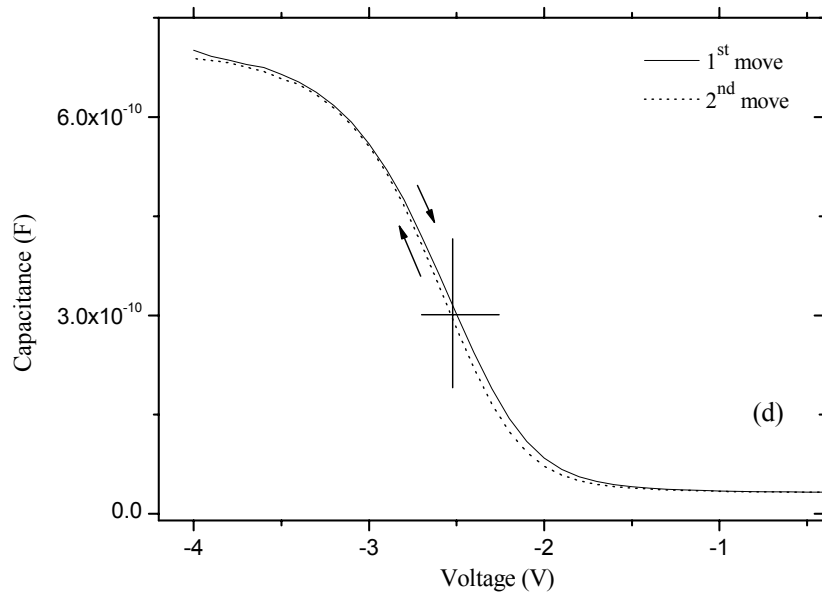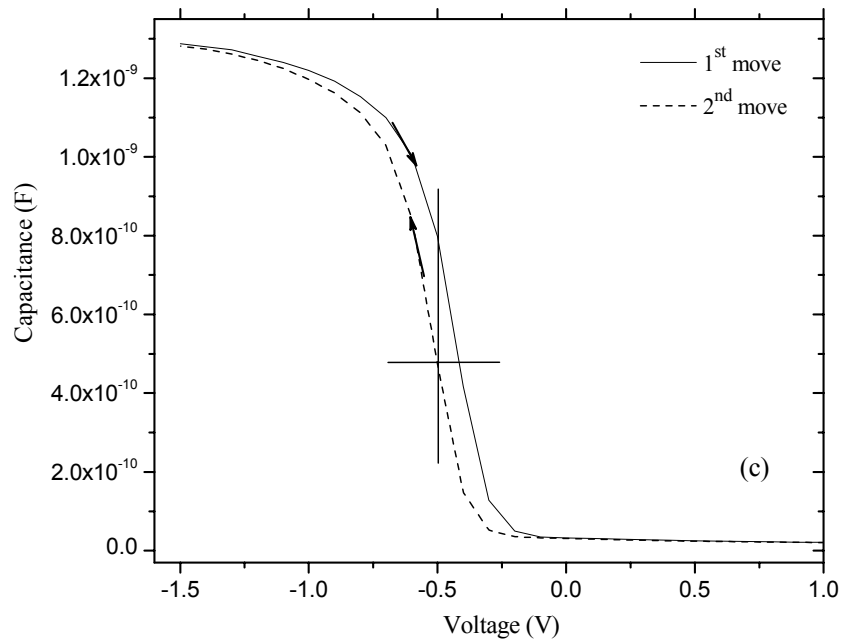
Figure 7.5 Capacitance with respect to applied voltage at 1 MHz frequency from accumulation to inversion (1st move) and from inversion to accumulation (2nd move).

7.3.2.3 Hysteresis effect and slow states

Laser grown oxides exhibit C – V hysteresis when the gate voltage is swept from accumulation to inversion and then from inversion to accumulation. This indicates the presence of slow states, Q_{slow}, which recharge during each bias cycle. The hysteresis effect at 1 MHz HF CV curve for all samples is shown in Figure 7.5 a-d. Hysteresis effect is detected at negative voltages for 300, 350 and 400^{0}C C-V curves, but it is at positive voltage side for 250^{0}C sample when the gate is swept from accumulation to inversion and then inversion to accumulation region. Slow states, Q_s, are obtained from the hysteresis effect at 1 MHz C-V curve and these charges are located very close to the interface with Si/oxide and recharge during the back bias cycle. The estimated slow states for all samples at 1 MHz frequency are calculated and given in Table 7.1. $\Delta V_{hysteresis}$ at 1 MHz C – V curve, between – (36 – 76) mV, give rise to ~10^{11} cm^{-2} slow states for T_s = 300 – 400^{0}C while it has opposite sign and has respectively higher value, $\Delta V_{FB}^{hyst} = 0.261V$ for T_s=250^{0}C resulting in –1.8 x 10^{11} cm^{-2} of slow states, Q_{slow}. The higher values of Q_{slow} are comparable to those obtained by other groups [72,73].

The frequency dispersion between 10 kHz and 1 MHz C – V curves near flat band conditions is used to estimate the value of the interfacial defect charges, Q_{fast}. Figure 7.6 a-d shows this effect for all samples near flat band voltage values and corresponding calculated values in the range between 7 x 10^{10} and 2 x 10^{12} cm^{-2} are shown in Table 7.1.
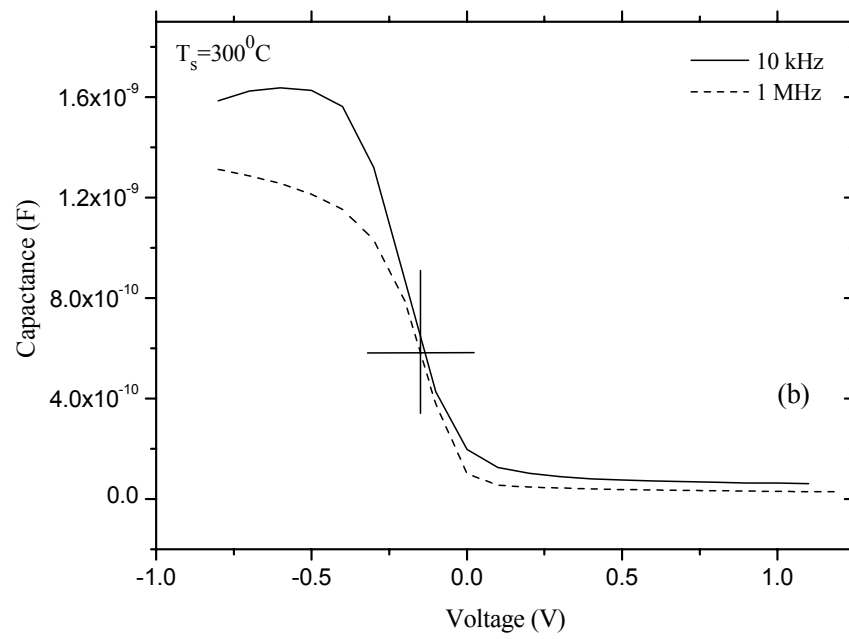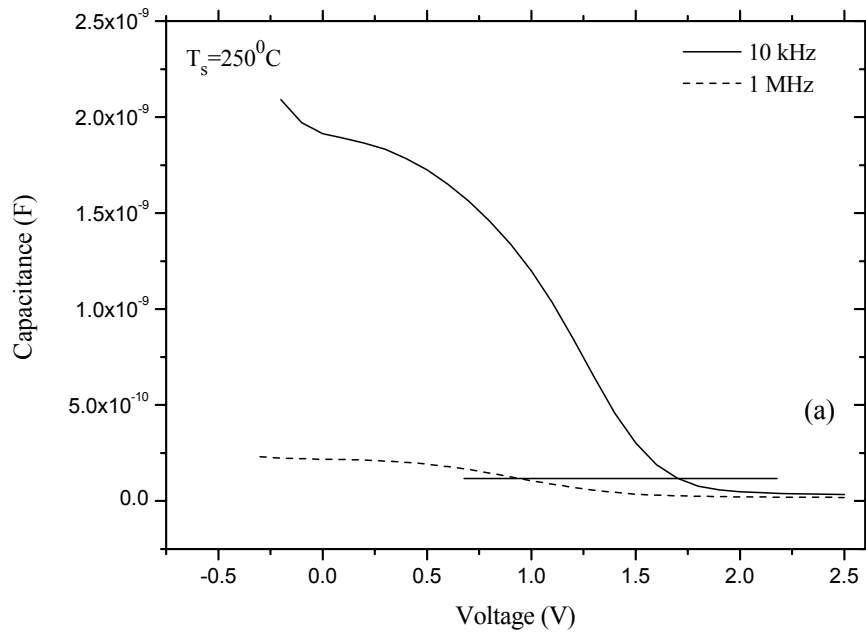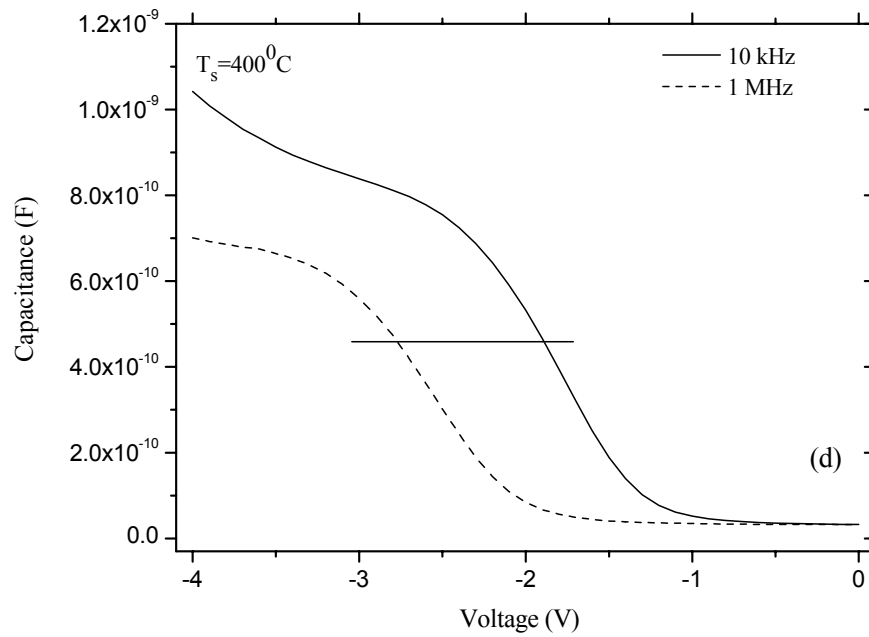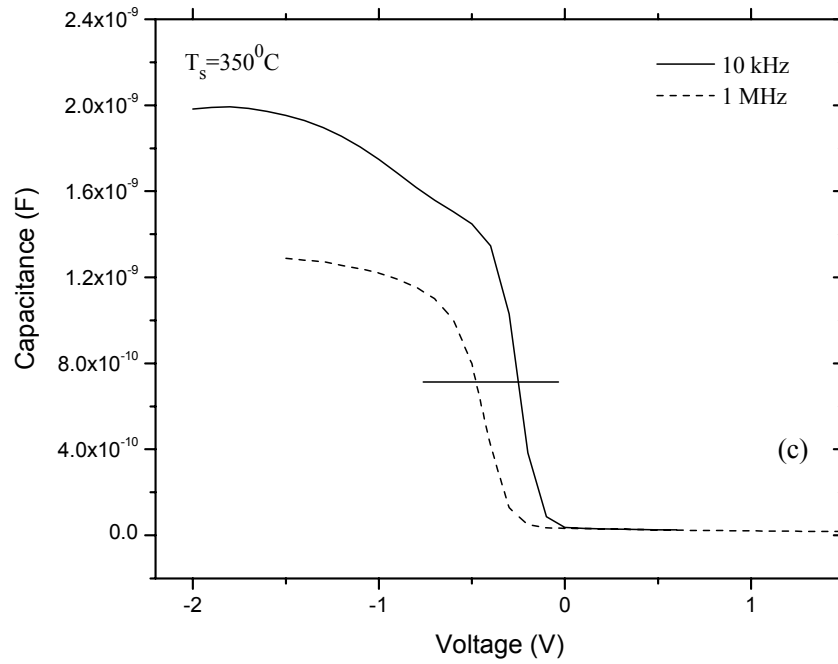
Figure 7.6 Capacitance with respect to applied voltage at 1 MHz and 10 kHz frequencies from accumulation to inversion mode.

7.3.2.4 I – V characteristics of the capacitors

The leakage current density through the capacitor as a function of applied voltage is shown for all samples in Figure 7.7. The effective oxide thickness values measured by the ellipsometry are 26 nm, 23 nm, 21 nm and 48 nm for T_s=250^{0}C, 300^{0}C, 350^{0}C and 400^{0}C oxides respectively. It is seen from this figure that the leakage current density decreases gradually as the substrate temperature increases. The variation is too small in the forward bias conditions (negative applied voltage values for which electrons are injected from Al gate) from 250^{0}C to 300^{0}C and to 350^{0}C while there is a sharp decrease for 400^{0}C indicating an oxide layer with better insulation. The leakage current starts from very low values ~10^{-9} A/cm^2 for very small applied voltages and it goes to 10^{-5} A/cm^2 for ~ -2 V for 400^{0}C oxide. In order to figure out the possible leakage current mechanisms, temperature dependent leakage current with respect to applied voltage characteristics needs to be studied.
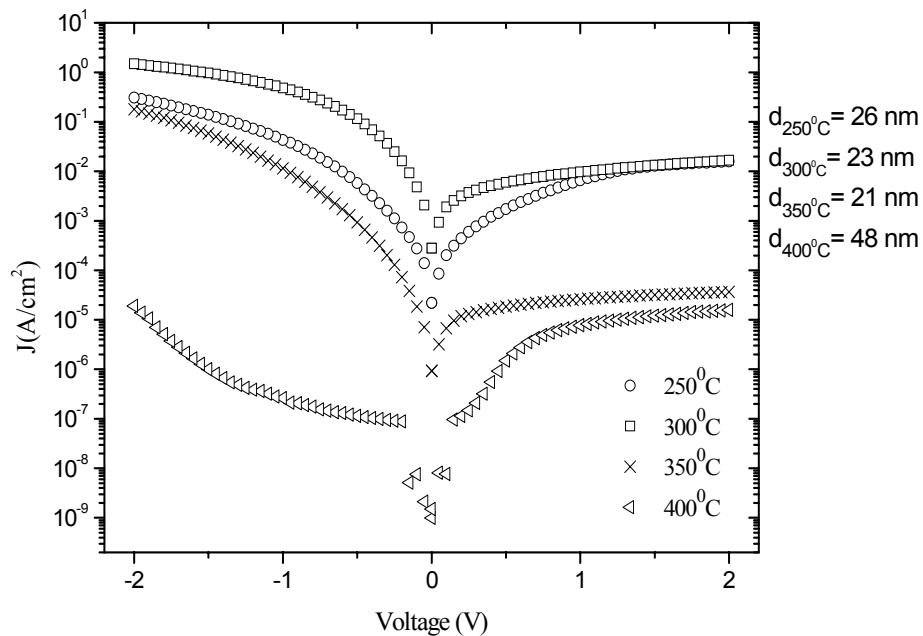
Figure 7.7 Leakage current versus applied voltage.

7.4 Conclusions

Thin rf-sputtered Ta films on Si substrate, 10, 15 and 20 nm thick Ta, were used to grow tantalum oxide films on Si by means of pulsed Nd:YAG laser working at 1064 nm wavelength regime. The refractive index values (~1.9 – 2.2) show that the laser grown layers have very good n values close to that of bulk Ta_2O_5. The oxide thickness distributions obtained from ellipsometer measurement results show a uniform Gaussian-like shape with the highest thickness at the center of the laser beam. The expected oxide thickness, which is twice that of initial Ta films, were obtained for T_s=300 – 350^{0}C and P=3.26 – 3.31 J/cm^2 per pulse.

Dielectric and electrical parameters were extracted from the capacitance and conductance of MOS capacitors with 1.96 x 10^{-3} cm^2 Al gate devices. From these measurements, the fixed oxide charges, Q_f, slow states from hysteresis effect at 1 MHz C–V curve, Q_s, fast interface states between 10 kHz and 1 MHz C–V curves, Q_{fast}, were obtained. The obtained values of Q_f and Q_s were compared with the values of obtained by other groups for Ta_2O_5 films grown by different oxidation methods. Leakage current densities of four different grown oxides were also compared with each other and shown that the current density level decreases while T_s increases.

The results show that the oxidation of Ta films by Nd:YAG laser is a promising growth method of Ta_2O_5 films. However, the film properties need to be improved in order to replace the SiO_2 layers currently used in the memory elements. Future work will cover the temperature dependent leakage current studies in order to better understanding of this material as well as XPS depth profiling studies to determine the structural composition of the grown oxides with respect to the depth from the surface of the oxide through the interface with Si.

CHAPTER 8

CONCLUSION

The main material of microelectronics for more than a few decades is based on the Si technology because of its excellent mechanical, chemical and electrical properties. This is mainly because of the native oxide of Si, namely SiO_2, having perfect interface with Si. However the constant shrinking of the device geometries of today's technology of microelectronics forces the thickness of SiO_2 to its physical limits. Therefore, the fabrication of ultra-thin and electrically reliable SiO_2 layers on Si substrate or fabrication of alternative dielectrics with high dielectric constant, (high-κ materials) are the main search parameters of the microelectronics nowadays. In both cases, however, there is always great interest in novel processing techniques that may improve the existing methods of production.

There are various methods to oxidize the semiconductor surfaces (see chapter 1 for details). Among all these methods, laser oxidation has attracted special attention due to its ability to induce localized oxidation with good spatial resolution, to achieve a good control over the thickness of very thin layer of 1-2 nm at low processing temperatures and the most suitable one reaching into some areas that other processes cannot be done, i.e. one of the most important techniques for thin film growth. On the other hand, one of the great advantages of laser annealing is that the laser radiation is heavily absorbed in a thin surface layer, a few hundred to several thousand angstroms in the surface.

Our main aim was to oxidize thin Ta film in order to grow tantalum oxide film by using Nd:YAG laser. Before realization of this, we had to optimize our laser

annealing system with well known and well studied dielectric which is SiO_2. The material chosen for laser oxidation process at the first stage is Si because it is the most studied material and all characteristics related to the Si and SiO_2 interface, and oxide layer were explored. Even though various forms of silicon oxide exist, the native oxide, namely silicon dioxide (SiO_2) is the most important one. Since having very high resistivity (higher than 10^{16} Ohm-cm), very important electrical parameters, i.e. dielectric breakdown strength > 10 MV/cm, surface states < $10^{11}/cm^2$ and chemically very stable, it is an excellent insulator.

In chapter 2, the theory of the laser radiation interaction with matter and MOS capacitor structures was given. In the laser interaction with matter part, the theory with respect to the laser wavelength and the matter phase situations were discussed. The most important definitions, and ideal and real situations related to MOS structures were given together with the suitable energy band diagrams.

In chapter 3, it was started with the parts of the constructed laser oxidation system and continued with procedures for the sample preparation methods and MOS capacitor construction details. Then, it continued with the short information related to the measurement systems and the types that we used. These can be given as the MOS capacitance and current measurements, spectrophotometric measurements, ellipsometry, X-ray photoelectron spectroscopy (XPS), Fourier Transform Infrared Spectroscopy (FTIR) and X-ray diffraction (XRD).

In chapter 4, thin SiO_2 films have been successfully obtained by 1064 nm Nd:YAG laser oxidation of p-Si in the presence of O_2. The thickness uniformity, dielectric and electrical properties, and optical characteristics of the layers were studied. The dielectric measurements in MOS configuration indicated that the laser-assisted oxide generally has parameters close to those of thermally grown SiO_2, such as interfacial defect charges, slow states density, leakage current and the capacitors showed true MOS behavior. An inverse relationship of the reflectance with the wavelength was exhibited. It was shown that the higher substrate temperature stimulates better oxidation revealing the denser films. An inverse relationship of the refractive indices with wavelength was observed. The optical properties showed

that the Nd:YAG laser oxidation of Si provides films whose optical thickness and refractive index can be controlled by the process conditions. Based on the results of this chapter, it can be concluded that to grow denser films the oxidation should take place at higher substrate temperatures and above 3.30 J/cm^2 laser power.

In chapter 5, the results of the X-ray photoelectron spectra (XPS) for the pulsed Nd:YAG laser oxidation of Si with a laser beam energy density close to the corresponding one to surface melting but without crossing it were given in details. It was shown that this technique is a promising way for growing at nearly stoichiometric SiO$_2$ at low temperatures. It was established that the films are non-perfect and nonstoichiometric containing in general Si suboxides in different amounts throughout the depth. It was concluded that post-oxidation annealing for improving microstructure of both oxide and near interface region is necessary.

In chapter 6, the properties of laser grown oxide layers by FTIR spectroscopy, XRD measurements and optical measurements for reflectance and refractive index values of the oxide layers were given. In the FTIR spectroscopy measurements, the most important parameter was found to be the substrate temperature other than the laser power used. XRD measurements revealed that the films obtained at the condition of $T_s < 350^0$C are amorphous for all films, but the crystallinity starts for the films produced from 10 nm thick Ta layers when $T_s = 400^0$C. However, the crystalline grains were seen to be at $T_s = 350^0$C for relatively thick 20 nm Ta layers. The dominant phase is orthorhombic β–Ta$_2$O$_5$. On the other side, reflectance values with respect to wavelength from optical measurements showed that the active oxidizing starts between 250 and 300^{0}C. Reflectance values decreases with increasing T_s showed that the denser layers were grown when T_s was increased. It was realized that the dominant effect for T_s values was between 300^{0}C and 350^{0}C for higher n values.

In chapter 7, the thickness profile and electrical properties of tantalum oxide films grown by pulsed Nd:YAG laser oxidized films were studied. The oxides were obtained from the thin rf-sputtered Ta films on Si substrate, 10, 15 and 20 nm thick Ta on Si. The refractive index values (~1.9 – 2.2) of the oxide films showed that the

laser grown layers had very good *n* values close to that of bulk Ta_2O_5. The oxide thickness distributions obtained from ellipsometer measurement results showed a uniform Gaussian-like shape with the highest thickness at the center of the laser beam. The expected oxide thickness, which is twice that of initial Ta films, were obtained for T_s=300-350^{0}C and P=3.26-3.31 J/cm^2 per pulse.

Dielectric and electrical parameters were extracted from the capacitance and conductance of MOS capacitors. From these measurements, the fixed oxide charges, Q_f, slow states from hysteresis effect at 1 MHz C–V curve, Q_s, fast interface states between 10 kHz and 1 MHz C–V curves, Q_{fast}, were obtained. Leakage current densities of four different grown oxides were also compared with each other and shown that the current density level decreases while T_s increases.

The results show that the oxidation of Ta films by Nd:YAG laser is a promising growth method of Ta_2O_5 films. However, the film properties need to be improved in order to replace the SiO_2 layers currently used in the memory elements.

REFERENCES

1   E. Atanassova, Microelectronics Reliability **39**, 1185 (1999)

2   J. D. Plummer, M. Deal and P. B. Griffin, Silicon VLSI Technology, New Jersey: Printice Hall (2000)

3   X.Blasco, M. Nafria, X. Aymerich, Surf. Sci. **532-535**, 732 (2003)

4   I. W. Boyd, Laser Processing of Thin Films and Microstructures, Berlin Heidelberg : Springer-Verlag, Chap. 2 (1987)

5   I. W. Boyd, Appl. Phys. Lett. **42**, 728 (1983)

6   I. W. Boyd and J. I. B. Wilson, Physica B **117& 118**, 1030 (1983)

7   A. Cros and F. Salvan, Appl. Phys. A **28,** 241 (1982)

8   T. E. Orlowski and H. Richter, Appl. Phys. Lett. 45, 241 (1984)

9   R. T. Young, J. Narayan, W. H. Christie, G. A. Van der Leeden, J. I. Levatter, L. J. Cheng, Solid State Technology **26**, 183 (1983)

10   D. H. Lowndes, Phys. Rev. Lett. **48**, 267 (1982)

11   N. Paulter, P. S. Peercy, Phys. Rev. Lett. **48**, 33 (1982)

12   B. C. Larson, C. W. White, T. S. Noggle, D. Mills, Phys. Rev. Lett. **48**, 337 (1982)

13 A. Gat, J. P. Gibbson, T. J. Magee, J. Peng, V. Deiling, P. Williams, C. A. Evans, Appl. Phys. Lett. **32**, 276 (1978)

14 L. Lavisse, D. Gravey, C. Langlade and B. Vannes, Appl. Sur. Sci. **186**, 150 (2002)

15 V. Cracuin, N. Bassim, R. K. Singh, D. Craciun, J. Hermann and C. Boulmer-Leborgne, Appl. Sur. Sci. **186**, 288 (2002)

16 P. Baeri and E. Rimini, Mater. Chem. Phys. **46**, 169 (1996)

17 H. Shinriki, T. Kisu, S. I. Kimura, Y. Nishioka, Y. Kawamoto, K. Mukai, IEEE Trans. Electron Devices **37**, 1937 (1990)

18 W. R. Hitchen, W. C. Krusell, D. M. Dobkin, J. Electrochem. Society **140**, 2615 (1993)

19 D. E. Gray, American Institute of Physics Handbook, 2nd Edition, New York: AIP (1972)

20 W. D. Driscol, W. Vaughan, Handbook of Optics, New York: Mc.Graw-Hill (1978)

21 C. Kittel, Introduction to Solid State Physics, London: Wiley (1972)

22 R. F. Marks, R. A. Pollack, Ph. Avouris, Laser Diagnostics and Photochemical Processing for semiconductor Devices, Eds. R.M. Osgood, S. R. J. Brueck, H. R. Schlossberg, North-Holland, Amsterdam p.257 (1983)

23 J. Y. Zhang, I. W. Boyd, Appl. Surf. Sci. **186**, 64-68 (2002)

24 C. Coste, Ozonation Manual for Water Treatment, Ed. W. J. Masschelein, Chichester (UK): Wiley, p.204 (1982)

25 J. Wen, M. H. Thiemens, Chem. Phys. Lett. **172**, 416 (1990)

26   I. W. Boyd, Mat. Res. Symp. Proc. **129**, "Ultrathin Silicon Dioxide Films: Photo-Induced Growth" Materials Research Society (1989)

27   J. R. McNesby, H. Okabe, Advances in Photochemistry, Vol.3, p.157, Eds. W.A. Noyes, G. Hammond, J.N. Pitts, New York: Wiley (1966)

28   S. E. Blum, K. H. Brown and R. Srinivasan, Appl. Phys. Lett. **43**, 102 (1983)

29   E. H. Nicollian, J. R. Brews, MOS (Metal Oxide Semiconductor) Physics and Technology, New York: John Wiley (1982)

30   H. C. Casey, Devices for Integrated Circuits: Silicon and III – V Compound Semiconductors, New York: John Wiley (1999)

31   D. Bauerle, Laser Processing and Chemistry, 3rd Edition, Berlin:Springer, Part II (2000)

32   Tz. Babeva, S. Kitova, B. Mednikarov, I. Konstantinov, Appl. Opt. **41,** 3840 (2002)

33   T. F. Coleman, Y. Li, SIAM J. Optimization **6,** 418 (1996)

34   E. Atanassova and T. Dimitrova, Handbook of Surfaces and Interfaces of Materials, vol 4, Edt. H S Nalwa, San Diego, California, USA: Academic Press, pp. 439-479 (2001)

35   A. I. Kingon, J. P. Maria and S. K. Streiffer, Nature **406**, 1032 (2000)

36   G. D. Wilk, R. M. Wallace and J. M. Anthony, J. Appl. Phys. **89**, 5243 (2001) (and references therein)

37   S. Wemple, M. DiDomenico, Phys. Rev. B **3** 1338 (1971)

38   Intern. Techn. Roadmap for Semiconduct. (ITRS) 2004 edition, http://public.itrs.net, last accessed date April 2005

39   P. M. Campbell, E. S. Snow, Mater. Sci. Eng. B **51,** 173 (1998)

40   S. Zankovych, T. Hoffmann, J. Seekamp, J. V. Bruch, C. M. Sotomayor, Nanotechnology **12**, 91 (2001)

41   A. Perez del Pino, P. Serra, J. L. Morenza, Appl. Surf. Sci. **197-198**, 887 (2002)

42   Q. Dong, J. Hu, J. Lian, Z. Guo, J. Chen, B. Chen, Scripta Materialia **48**, 1373 (2003)

43   J. S. Johannessen, W. E. Spicer, Y. E. Strausser, J. Appl. Phys **47**, 3028 (1976)

44   M. H. Hecht, F. J. Grunthaner, P. Pianetta, L. I. Johansson, I. Lindau, J. Vac. Sci. and Technol. A **2**, 584 (1984)

45   A. S. Vengurlekar, A. N. Chandorkar, K. V. Ramanathan, Thin Solid Films **114**, 285 (1984)

46   E. Atanassova, A. Paskaleva, Appl. Surf. Sci. **103**, 359 (1996)

47   F. J. Grunthaner, B. F. Lewis, N. Zamini, J. Maserdjian, A. Madhukar, IEEE Trans. Nucl. Sci. **27**, 1640 (1980)

48   F. T. Himpsel, F. R. Mc. Feely, A. Taleb-Ibrahimi, J. A. Yarmoff, G. Hollinger, Phys. Rev. B **38**, 6084 (1988)

49   E. Atanassova, A. Paskaleva, Appl. Surf. Sci. **120**, 306 (1997)

50   C. M. Garner, I. Lindau, C. Y. Su, P. Pianetta, W. E. Spicer, Phys. Rev. B **19**, 3944 (1979)

51   T. Adachi, C. R. Helmus, J. Electrochem. Soc. **127**, 1617 (1980)

52   T. L. Barr, Appl. Surf. Sci. **15**, 1 (1983)

53   J. M. Sauz, S. Hofmann, Surf. Interf. Anal. **5**, 210 (1983)

54   S. Kamiyama, P.Lesaicherre, H. Suzuki, A. Sakai, I. Nishiyama, A. Iskitani, J. Electr. Soc. **40**, 1617 (1993)

55   S. R. Jeon, S.W. Han, J. W. Park, J. Appl. Phys. **77**, 5978 (1995)

56   J. V. Chrahn, P. E. Hellberg, E. Olson, J. Appl. Phys. **84**, 1632 (1998)

57   C. Chaneliere, J. L. Autran, R. A. B. Devine, B. Balland, Mater. Sci. Eng. **R22**, 269 (1998)

58   K. Kukli, J. Aarik, A. Aidla, O. Kohan, T. Uustare, V. Sammelselg, Thin Solid Films **260**, 135 (1995)

59   Z. Mingfei, F. Zhengwen, Y. Haijun, Z. Zhuangjian, Q. Qizong, Appl. Surf. Sci. **108 (3)**, 399 (1997)

60   Y. Nishimura, A. Shinkawa, H. Ujita, M. Tsuji, M. Nakamura, Appl. Surf. Sci. **136**, 22 (1998)

61   J. Y. Zhang, I. W. Boyd, Appl. Surf. Sci. **168**, 234 (2000)

62   S. Boughaba, G. I. Sproule, J. P. McCaffrey, M. Islam, M. J. Graham, Thin Solid Films **358**, 104 (2000)

63   J. Y. Kim, M. C. Nielsen, E. J. Rymaszewski, T. M.Lu, J. Appl. Phys. **87**, 1448 (2000)

64   I. W. Boyd, J. Y. Zhang, Microel. Reliab. **40**, 649 (2000)

65   J. Y. Zhang, V. Dusastre, I. W. Boyd, Mater. Sci. in Semicond. Processing **4**, 313 (2001)

66   E. Atanassova, N. Novkovski, A. Paskaleva, M. Pesovska-Gjorgjevich, Solid. St. Electr. **46**, 1887 (2002)

67   M. Passacantando, F. Jolly, L. Lozzi, V. Salerni, P. Picozzi, S. Santucci, C. Corsi, D. Zintu, J. Non. Cryst. Solids **322**, 225 (2003)

68   J. J. Yu, J. Y. Zhang, I. W. Boyd, Appl. Surf. Sci. **186**, 57 (2002)

69   X-Ray Diffraction File, ICDD.

70   J. Y. Zhang, Q. Fang, I. W. Boyd, Appl. Surf. Sci. **138–139**, 320 (1999).

71   Tz. Babeva, E. Atanassova, J. Kaprinarova, Phys. St. Sol. A, in press.

72   E. Atanassova, A. Paskaleva, Microelec. Reliab. **42**, 157 (2002)

73   E. Atanassova, D. Spassov, Microelec. Reliab. **42**, 1171 (2002)
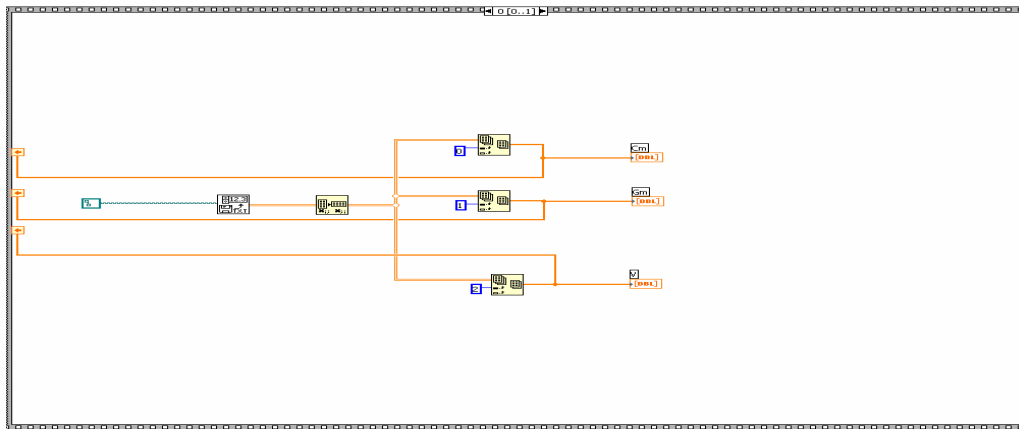
**Figure A1** The first loop of the series resistance correction program
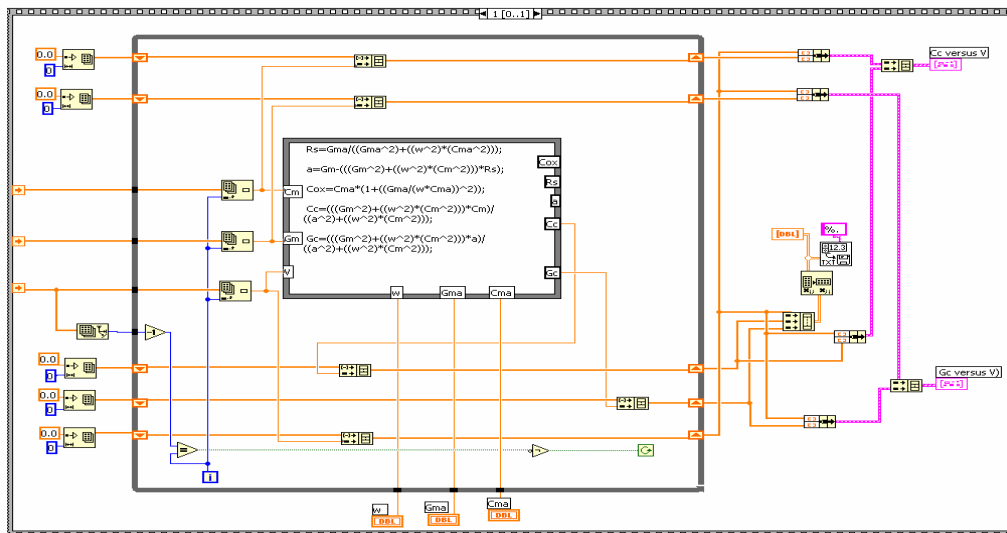
Figure A2 The second loop of the series resistance correction program

VITA

The author, Gülnur AYGÜN ÖZYÜZER, was born in Ankara on May 07, 1970. She received her B.S. degree in Physics Engineering Department from Ankara University in 1991 and M.S. degree in Physics Department from the Ohio State University (OSU) in 1997. Title of her master thesis is "Injection Locking of Single Stripe Diode Lasers". She has been working as a research/teaching assistant in the Department of Physics, METU.

List of Publications of Gülnur AYGÜN ÖZYÜZER:

1. "Thickness profile and electrical properties of tantalum oxide films grown by pulsed Nd:YAG laser oxidation" **G. Aygun**, E. Atanassova, R. Turan, in preparation.
2. "Structural and optical characteristics of tantalum oxide grown by pulsed Nd:YAG laser oxidation" E. Atanassova, **G. Aygun**, R. Turan, submitted to Materials Chemistry and Physics.
3. "XPS study of pulsed Nd:YAG laser oxidized Si" **G. Aygun**, E. Atanassova, K. Kostov, R. Turan, submitted.
4. "Spatial distribution of light – emitting centers in Si – implanted SiO_2" U. Serincan, **G. Aygun**, R. Turan, Journal of Luminescence, in press.
5. "Properties of reactive O_2 ion beam sputtered TiO_2 on Si wafers" S. Ulucan, **G. Aygun**, L. Ozyuzer, M. Egilmez, R. Turan, Journal of Optoelectronics and Advanced Materials **7**, 297 (2005).
6. "Reflectance spectra and refractive index of Nd:YAG laser oxidized Si surface" **G. Aygun**, E. Atanassova, R. Turan, Tz. Babeva, Materials Chemistry and Physics **89**, 316 (2005).

7. "Oxidation of Si Surface by a Pulsed Nd-YAG Laser" **G. Aygun**, E. Atanassova, A. Alacakir, L. Ozyuzer, R. Turan, Journal of Physics D: Applied Physics **37**, 1569 (2004).

8. "Darbeli lazer aşındırma yöntemiyle nanoboyutta üretilmiş SiO_2 parçacıkların karakterizasyonu", Mine Bahçeci , Lütfi Özyüzer, **Gülnur Aygün**, Raşit Turan, 10. Denizli Malzeme Sempozyumu ve Sergisi 142-146 (14-15-16 Nisan 2004).

9. "The Structure and Properties of Liquid Metals from Molecular Dynamics", G. Dereli, **G. Aygün Özyüzer** and Tahir Çağın, preprint (2000).

International conferences / meetings attended:

1. "The Structure and The Properties of Liquid Metals from Molecular Dynamics", **G. Aygün Özyüzer**, G. Dereli, and Tahir Çağın, has been presented at the 2000 March Meeting of the American Physical Society (March 20-26, 2000) in Minneapolis, MN, USA, (Oral presentation).

2. "Properties of reactive O_2 ion beam sputtered TiO_2 on Si wafers" S. Ulucan, **G. Aygun**, L. Ozyuzer, M. Egilmez, R. Turan, 13th International School on Condensed Matter Physics: Varna, Bulgaria August 29-September 4, 2004.

National conferences/meetings attended:

1. XI Yoğun Madde Fiziği Ankara Toplantısı, Ankara – Turkey, 3 Aralık 2004, (Oral presentation: Nd:YAG Puls Lazeri Aracılığıyla büyütülen Si oksitlerinin Yapısal, Kimyasal, Elektriksel ve Optiksel Özellikleri.)

2. 22. Turkish Physical Society Conference, Bodrum – Turkey, 14–17 September, 2004, (Oral presentation: Electrical and Optical Properties of Nd:YAG Laser Grown Si Oxides.)